UNIVERSITÀ DEGLI STUDI DELLA CALABRIA

Dipartimento di FISICA

Scuola di Dottorato

Scienze, Comunicazione e Tecnologie "Archimede"

Indirizzo

"Fisica e Tecnologie Quantistiche"

Con il contributo di

Secretaría de Educación Superior, Ciencia, Tecnología e Innovación (SENESCYT-ECUADOR)
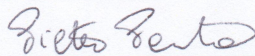
CICLO

XXVIII

Plasmon Phenomena in Graphene-related and Graphene-beyond Materials: a Time-Dependent Density Functional Theory Approach.

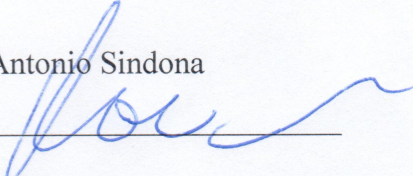**Settore Scientifico Disciplinare** FIS/03 - FISICA DELLA MATERIA

Direttore: Prof. Pietro Pantano
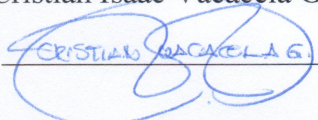
Firma _____

Supervisore: Dott. Antonio Sindona

Firma _____

Dottorando: Dott. Cristian Isaac Vacacela Gómez

Firma _____

Plasmon phenomena in graphene–related and beyond–graphene materials: a time–dependent density functional theory approach.

Cristian Isaac Vacacela Gomez

February 9, 2017

Contents

Abstract

The plasmonic properties of graphene-related and beyond-graphene materials are investigated with a proper time-dependent density functional theory in the random phase approximation approach. Both the intrinsic (undoped) and several extrinsic (carrier doped or gated) conditions are explored by simulating injection of a probe particle (i.e., an electron or a photon) of energy below 20 eV and in-plane momentum smaller than 1.0 $\mathring{A}^{-1}$. The energy-loss function of the systems is analyzed, with particular reference to its induced charge-density fluctuations, i.e., plasmon resonances and corresponding dispersions, occurring in the investigated energy-momentum region.

Silicene, germanene, as well as graphene nanoribbons organized in periodic 2D planar arrays are characterized by two intrinsic interband plasmons at energies larger than 1.5 eV. These plasmon modes reasemble to the well-known π and $\sigma - \pi$ modes of graphene. Interesting enough, silicene and germanene show a hybridized π-like plasmon, which is assisted by competing one-electron processes involving sp^2 and sp^3 states, and depends on the slightest changes in specific geometric parameters, such as nearest-neighbor atomic distance and buckling constant.

At energies below 1 eV, two extrinsic intraband modes are predicted to occur in silicene and germanene, which are generated by distinct types of Dirac electrons (associated with different Fermi velocities at the so-called Dirac points). The most intense of them is a two-dimensional plasmon, having an energy-momentum dispersion that resembles that of a two-dimensional electron gas. The other is an acoustic plasmon that occurs for specific momentum directions and competes with the two-dimensional plasmon at mid-infrared energies. The strong anisotropic character of this mode cannot be explained in terms of the widely used Dirac-cone approximation. Furthermore, these extrinsic oscillations are highly sensitive to the concentration of injected or ejected charge carriers. In addtion to these modes, germanene exhibits a new intraband plasmon, which can be originated with a doping > 0.3 eV.

On the other hand, extrinsic semimetallic (zigzag) nanoribbons display an intraband plasmon following the energy-momentum dispersion of a two-dimensional electron gas. Extrinsic semiconducting (armchair) nanoribbons are instead characterized by two distinct intraband and interband plasmons, whose fascinating interplay is extremely responsive to either injection of charge carriers or increase in electronic temperature. These oscillations share some common trends with recent nanoinfrared imaging of confined edge and surface plasmon modes detected in graphene nanoribbons of 100–500 nm width.

List of Publications

[1] **C Vacacela Gomez**, M Pisarra, M Gravina, P Riccardi, A Sindona. Physical Review B **95**(8), 085419 (2017).

[2] D. Coello-Fiallos, T. Tene, J. L. Guayllas, D. Haro, A. Haro, **C Vacacela Gomez**. To appear in Materials Today: Proceedings (2017).

[3] **Cristian Vacacela Gomez**, Michele Pisarra, Mario Gravina, Antonello Sindona. Beilstein Journal of Nanotechnology **8**(1), 172-182 (2017).

[4] **C Vacacela Gomez**, M Pisarra, M Gravina, J M Pitarke, A Sindona. Physical Review Letters **117**(11), 116801 (2016).

[5] Luis Villamagua, Manuela Carini, Arvids Stashans, **Cristian Vacacela Gomez**. Ricerche di Matematica **65**(2), 579-584 (2016).

[6] **C Vacacela Gomez**, M Pisarra, M Gravina, S Bellucci, A Sindona. Research and Technologies for Society and Industry Leveraging a better tomorrow (RTSI), 2016 IEEE 2nd International Forum on, 1-4 (2016).

[7] **C Vacacela Gomez**, E Robalino, D Haro, T Tene, P Escudero, A Haro, J Orbe. Materials Today: Proceedings **3**(3), 796-802 (2016).

[8] L Pierantoni, D Mencarelli, A Sindona, M Gravina, M Pisarra, **C Vacacela Gomez**, S Bellucci. Microwave Symposium (IMS), 2015 IEEE MTT-S International, 1-3 (2015).

[9] Antonello Sindona, Michele Pisarra, Mario Gravina, **Cristian Vacacela Gomez**, Pierfrancesco Riccardi, Giovanni Falcone, Francesco Plastina. Beilstein Journal of Nanotechnology **6**(1), 755-766 (2015).

[10] D Coello Fiallos, **C Vacacela Gomez**, G Tubon Usca, D Cid Perez, P Tavolaro, G Martino, LS Caputi, A Tavolaro. AIP Conference Proceedings **1646**(1), 79-86 (2015).

[11] G Tubon Usca, **C Vacacela Gomez**, D Coello Fiallos, P Tavolaro, G Martino, LS Caputi, A Tavolaro. AIP Conference Proceedings **1646**(1), 79-86 (2015).

Funding and Technical Resources

Acknowledgements

First I want thank God, second my supervisor Antonello Sindona for all his contributions of time, ideas, and funding to make my Ph.D., it has been an honor to be his Ph.D. student.

The members of Condensed Matter group have contributed immensely to my personal and professional time at University of Calabria. I am especially grateful for Michele Pisarra and Mario Gravina, as well Jacopo Settino a good friend.

Lastly, I would like to thank my family for all their love and encouragement. For my mother and grandfhaters who raised me with a love of science and supported me in all my pursuits. For my son Emiliano, without him, I could have delivered the thesis months ago, but none of this would make sense. And most of all for my loving, supportive, encouraging, and patient wife Talia, whose faithful support during the final stages of this Ph.D. is so appreciated. Thank you.

Cristian Vacacela Gomez
University of Calabria
February 2017

Chapter 1

Introduction

Control and manipulation of light at sub-wavelength scales has been one of the most important goals for fundamental research and applied science in the recent years. In this context, the field of plasmonics, that is a branch of optics and photonics, grows rapidly due to the novel optical properties originated at the nanometer scale when the light interacts, e.g., with thin metal films or metal nanoparticles. These optical signals exist beyond the imposed diffraction limit [1] [2], and they have been proved to be tunable [3, 4, 5]. Both of these amazing features (existence and tunability) may be directed to the design of next-generation of nanoplasmonics and nanophotonics devices [6, 7], with the enhanced capability to operate from visible (VIS) to terahertz (THz) frequencies for a broad range of applications, such as biological sensing [8], biomedical diagnostics [9], labels for biomedical research [10], nanoantennas for light-emitting diodes [11], cancer treatment [12], solar energy conversion [13], optical signal processing [14], and quantum information technology [15, 16].

---

[1]The major problem with using light (electromagnetic waves) in optical signal-processing devices and integrated circuits is the low levels of integration and miniaturization available, which are far poorer than those achievable in modern electronics. This problem is a consequence of the diffraction limit of light in dielectric media, which does not allow the localization of electromagnetic waves into nanoscale regions much smaller than the wavelength of light in the material [1].

1.1   Surface Plasmons

As a preliminary introduction to the concept of surface plasmon, imagine that a light-wave falls on a metal surface [17, 18]. The electrons of the metal sample move freely and, driven by the external light electric field associated to the light pulse, they are periodically displaced with respect to the lattice ions. This displacement creates charges of opposite at opposite surfaces. Because these charges attract each other, there also exists a restoring force. The result is a periodic free-electron gas oscillator, whose quantum is called surface plasmon (SP) and whose frequency is determined by the restoring force and effective mass of the electron. The plasmon frequency depends on the atomic composition, size and shape of the nanostructured material [17]. Thus, striking and distinct plasmonic properties can be identified, which need to be characterized from the fundamental point of view with a proper physical description, e.g., by using a full *ab initio* approach [19, 20].

Generally, SPs are defined as collective and coherent oscillation of the valence electron–density in conductive materials [21, 22]. These oscillations possess a number of appealing properties for nanophotonic technologies, the most remarkable of which are, perhaps, (1) their small spatial extension compared with the light wavelength, which has been exploited to achieve improved imaging resolution [23]; (2) their strong interaction with light, which is evidenced by a centenary tradition of generating colors through plasmon-supporting metal nanoparticle suspensions [24]; and (3) the huge optical enhancements produced by this strong interaction, which upon external illumination result in near-field intensities $> 10^5$ times larger than the incident light intensity, as inferred from surface-enhanced Raman scattering (SERS) measurements [25].

In this thesis, we scrutinize the electronic and plasmonic properties of atomically thin materials organized in two-dimensional (2D) honeycomb–like geometries, say, graphene-related materials, e.g., graphene nanoribbons (GNRs), structured in periodic planar arrays, as well as beyond-graphene materials e.g., monolayer silicene (MSi) and monolayer germanene (MGe). These novel nanomaterials have emerged as powerful plasmonic materials in the latest years, that combine the appealing properties described above with the ability of being electrically tunable, which is the main motivation behind our study. As for technological applications, graphene-related and beyond materials can be used: (i) to integrate optics in nanoelectronic devices using the light to transmit data [15]; (ii) for ultrasensitive detection down to the single-molecule level [26], (iii) in nanoscale photometry [27] and nonlinear optics [28].

1.2   Plasmonics

A first approach to plasma oscillation was developed by Gustav Mie in 1908 [29], with his classic paper on light scattering by dielectric absorbing spherical particles. Nowadays with the progress nanofabrication techniques by structuring nanomaterials, a renewed interest in surface plasmons was given after the discovery of the unique physical and chemical properties [30] of monolayer graphene (MG) and its ability to confine the optical energy [31].

Specifically, at THz frequencies, the graphene surface plasmons (GSPs) [32] compared to the conventional SPs detected in metal nanoparticles e.g., gold and silver [33], show: (1) *enhanced tunability* of the optical responses changing the doping level i.e., the charge-carrier (electron or holes) concentrations related to the Fermi energy (E_F), generally, in the order from 10^{12} cm^{-2} to 10^{14} cm^{-2}, (2) *stronger confinement*, because GSPs wavelength are $\sim$ 1–3 orders of magnitude smaller than the visible-light wavelengths, and (3) *low losses* due to its long optical relaxation times reaching values of $\tau \approx 10^{-13}$ s, compared to $\tau \sim 10^{-14}$ s in gold, and allowing a viable solution to the long–standing problem of dissipation in plasmonics.

At high–energies (> 50 eV), experimental reports working on MG with a free–standing conformation [34, 35], have demonstrated that MG is characterized by two plasmon structures at $\sim$ 4.7 eV and $\sim$ 14.6 eV, which have been labelled π and $\sigma + \pi$, because they are assisted by single-particle (SP) processes that involve transitions from band states with dominant π and σ character. Similar modes have been detected in graphite at 7 eV and 26 eV, respectively. However, these plasmons cannot be controlled, at least with current technology.

Recently, enhanced graphene plasmonic properties have been reported when MG is cut in micro– or nanoribbons [31, 36], and these one-dimensional nanostructures are organized in 2D arrays, which offers an extra tunability of the GSP outlined above and, furthermore, it gives rise to a new confined graphene edge plasmon (GEP), as consequence of the geometrically controllable band–gaps of these graphene-related systems.

Both the GSP and GEP modes have been detected with nano-infrared imaging techniques [36] in GNR arrays of 100-500 nm in width, and theoretically confirmed even in narrowest–periodic arrays on GNRs of $\sim$1 and $\sim$2 nm in width [37]. Additionally, at high–energies these narrow GNR arrays also exhibits similar plasmon structures like MG, i.e., the π plasmon at $\sim$ 3 eV and the $\sigma + \pi$ plasmon at $\sim$ 13 eV, showing a controlable behavior at visible (VIS) frequencies [37].

The incompatibility of graphene–related materials such as MG, bilayer graphene (BLG), fewlayer graphene (> 7 layers) and GNR arrays, with the current silicon–based electronics has motivated the research on other group-IV elements with associated honeycomb–like lattice, e.g., Silicon and Germanium. Their single–layer conformations i.e., MSi and MGe, share much of the unique properties of MG, with the following advantages: [38]: (i) compatibility with the current semiconductor technology, (ii) controlable band–gaps in presence of a perpendicular electric field or by chemical functionalization, (iii) experimental realization of quantum spin Hall effect due to their stronger spin–orbit gap coupling, and (iv) epitaxial synthesis on several metallic or band–gap substrates with different electronic properties.

On the theoretical side, semi–classical and tight binding (TB) approaches are preferential frameworks to describe the electronic properties in these honeycomb–like systems [39, 40, 41, 42], because they turn out to be sufficiently accurate for far infrared applications. However, the main essence of the ground-state and excited-state properties of the nanosystems are not properly or fully considered, which makes these models unsuitable for applications in the mid-infrared to ultraviolet band. For instance in graphene, the Dirac cone approximation contemplates an isotropic top valence (π) and

bottom conduction (π^*) band dispersion at some special points in the reciprocal space, the so-called K and K' points, which is reliable for an ideal graphene sheet at probing frequencies below 10 THz ($\sim$ 0.04 eV). Otherwise, density functional theory (DFT) calculations have reveled an anisotropic energy band structure [43, 44], which explains why an extra plasmon mode appears at low–frequency in doped MG. The latter has been called acoustic plasmon (AP) [44], in analogy with the phonon modes of diatomic lattices.

Thus, a proper description of the plasmon structure and plasmon propagation in graphene–related and beyond–graphene materials, is still laking. Here, we provide a full *ab initio* framework to scrutinize the plasmonic properties of MG, MSi, MGe and GNR arrays, considering several intrinsic (undoped) and extrinsic (doped/gated) conditions. A plan of the thesis is briefly outlined in the next subsection.

1.2.1 Overview of the thesis

Chapter 2 presents a discussion of the structural and electronic properties of 2D honeycomb–like systems, based on experimental evidences and previous theoretical reports found in the literature. For instance, free-standing MG is characterized by a sp^2 hybridization and a linear band dispersion around the Fermi energy. MSi and MGe, in free-standing form, are characterized by low-buckled structural conformation, due to their mixed $sp^3 - sp^2$ hybridization. Nonetheless, they preserve the linear dispersing feature of the top valence and low conduction bands at the Fermi energy. On the other hand, GNRs exhibit a semiconducting or semimetallic behavior, depending on their geometry, which can be exploited to modulate their electronic and plasmonic properties.

Chapter 3 describes the theoretical framework used throughout all the thesis. It is based on time-dependent density functional theory (TDDFT) at the level of the random-phase approximation (RPA) in the linear-response (LR) regime. A short review of DFT is provided as well, which is not the main topic of this thesis, but it is used as a working tool to obtain the ground-state electronic properties and the Kohn-Sham (KS) single-particle energies and orbitals. In the same chapter the usual TDDFT scheme for 3D periodic systems is given, and a correction to the methodology suitable for 2D periodic systems is developed, which basically consists in a mixed space representation that will allow to cut-off unwanted interactions between the system replicas, inherent DFT computations with the plane-wave basis set.

Chapter 4 focusses on the plasmon structure of and plasmon dispersion in MG, MSi and MGe by energy–loss calculations. First, the TDDFT approach of chapter 3 is validated by the comparison of our energy loss calculations performed on MG with some experimental data available in the literature. Second, the energy loss calculations are carried out on free-standing MSi and MGe at higher– and lower–energies, considering both intrinsic (undoped) and extrinsic (doped/gated) conditions.

Chapter 5 shows how the GSP and GEP modes are originated in 2D periodic–arrays of semi-conducting and semi-metallic GNRs, and are affected by the width, chirality and unit-cell length of each ribbon, as well as the in-plane vacuum distance between

two contiguous ribbons. The *ab initio* simulations are compared with semi–classical and tight binding approaches available in the literature, focusing on the low energy and vanishingly small momentum features of the systems' response.

Chapter 6 summarizes to the main conclusions and perspectives of the thesis.

Chapter 2

2D materials

One-atom thick materials in two dimensions, are one of the most active areas of nano-materials research [45, 46]. They offer attractive electronic properties, either as single or few layers, or as part of a layered heterostructure. In this context, graphene is the most widely studied 2D material and many of its unique properties are due to its low energy electronic band structure around the Dirac point, where the occupied π and unoccupied π^* states cross, leading to quasiparticles that mimic the characteristics of massless Dirac Fermions. This results in charge-carriers that propagate with a Fermi velocity, which is about 1/300th of the speed of light, leading to high room temperature mobilities [47]. Graphene has already demonstrated these properties serving variously as a calibration for universal constants, as a transparent contact in solar cells [48] and in high frequency electronics [49] with high cut-off frequencies.

Although there is sustained research effort in the study of graphene, recent attention has turned to alternative 2D materials [50]. Of particular interest are the other group IV elemental materials, i.e., silicene and germanene, because of their compatibility with the current semiconductor technology [51]. Silicene and germanene also possess a honeycomb-like lattice, and show a linear band dispersion around the Fermi energy at the K point and the appearance of massless Dirac Fermions like graphene [52]. In this chapter, we present a short description of the electronic and structural properties of graphene, silicene and germanene as well as graphene nanoribbons organized in 2D planar arrays. We also review the state-of-the-art of low dimensional systems, with reference to the seminal papers that accelerated nanotechnology research and development [46].

2.1 Graphene

Since it has been peeled off from graphite [Fig. 2.1(a)] in 2004, with the "Scotch tape method" developed by Novoselov and Geim [53], graphene have attracted huge attention due to its unique electronic, optical, thermal and mechanical properties [54, 55] and posible technological applications from nanocompites to conductive coatings [56].
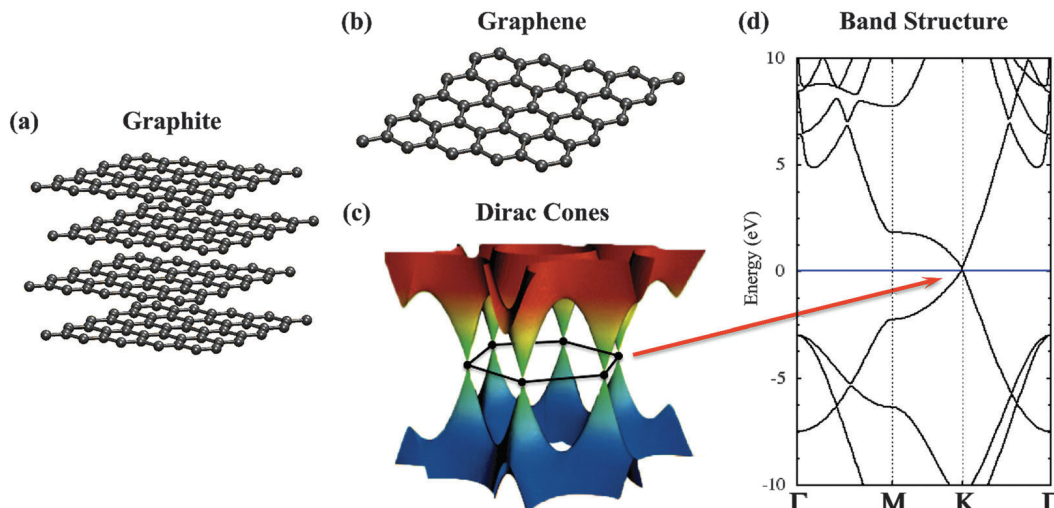

Figure 2.1: Taken from Ref. [57]. (a) graphite, (b) graphene, (c) Dirac cones in graphene [], (d) graphene band structure along high-symmetry path: ΓΜΓΚ. Fermi level set up to 0 eV.

Graphene is an atomically thin sp^2 (planar) layered material made out of carbon (C) atoms arranged on a honeycomb-like structure made out of hexagons, and can be thought of as composed of benzene rings stripped out from their hydrogen atoms [Fig. 2.1(b)] [30, 58]. Each C atom forms three σ bonds with the adjacent C atoms via sp^2 hybridization, leaving a perpendicular half occupied p_z orbital. The coupling of p_z orbital between adjacent atoms forms the π bond. The planar structure of graphene arises from the short C-C bond length (~ 1.42 Å) and consequently the strong π bonding [58, 59].

Due to the peculiar electronic structure [Fig. 2.1(c),(d)], graphene is a zero band gap material with a semimetallic behavior with vanishing density of states at the Fermi level [see Fig. 2.4]. The Fermi level is crossed by the π (highest valence) and π^* (lowest conduction) bands near the six corners (inequivalent K and K' points) of the 2D hexagonal Brillouin zone [Fig. 2.1(c)]. Furthermore, the π and π^* bands display a linear (or conical) dispersion close to the K and K' points. This this feature leads to zero massless charge-carriers, and thus to very high electric currents. Quasi electrons and holes moving as free massless particles can be described by the Dirac equation, therefore, they are called Dirac fermions and the six corners of the Brillouin zone are called the Dirac points [60, 61].

From the crystallographic point of view the real-space structure of graphene [Fig. 2.2] can be seen as a triangular lattice with a basis of two atoms per unit-cell. The primitive
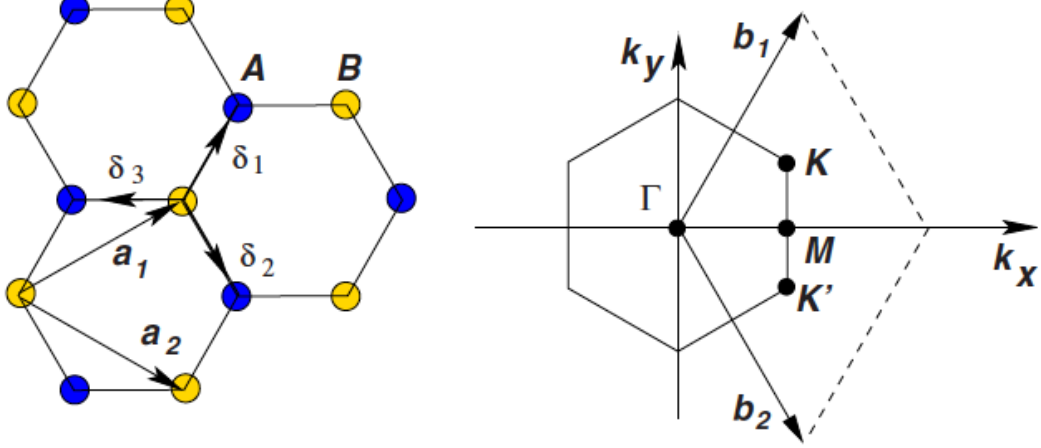
Figure 2.2: Taken from Ref. [30]. (Left) honeycomb-like lattice and (right) Brillouin zone of graphene; $\mathbf{a_1}$ and $\mathbf{a_2}$ are the lattice unit vectors, δ_i, $i = 1, 2, 3$ are the nearest-neighbor vectors. $\mathbf{b_1}$ and $\mathbf{b_2}$ correspond to the reciprocal lattice vectors. The Dirac cones are located at the K and K' points.

vectors of the real space lattice can be written as

$$\mathbf{a_1} = \frac{a}{2}(3, \sqrt{3}), \quad \mathbf{a_2} = \frac{a}{2}(3, -\sqrt{3}) \tag{2.1}$$

where $a \sim 1.42$ Å is the C-C bond length in graphene. A possible choice of primitive vectors for the reciprocal space is the following

$$\mathbf{b_1} = \frac{2\pi}{3a}(1, \sqrt{3}), \quad \mathbf{b_2} = \frac{2\pi}{3a}(1, -\sqrt{3}). \tag{2.2}$$

Hence, a possible shape of the first Brillouin zone is the parallelogram generated by $\mathbf{b_1}$ and $\mathbf{b_2}$ [Fig 1.2(right)], which includes the inequivalent Dirac points

$$\mathbf{K} = (\frac{2\pi}{3a}, \frac{2\pi}{3\sqrt{3a}}); \quad \mathbf{K'} = (\frac{2\pi}{3a}, -\frac{2\pi}{3\sqrt{3a}}). \tag{2.3}$$

The three nearest-neighbor vectors in real space are given by

$$\boldsymbol{\delta_1} = \frac{a}{2}(1, \sqrt{3}), \quad \boldsymbol{\delta_2} = \frac{a}{2}(1, -\sqrt{3}), \quad \boldsymbol{\delta_3} = -a(1, 0) \tag{2.4}$$

and the six second-nearest neighbors are located at

$$\boldsymbol{\delta'_1} = \pm\boldsymbol{a_1}, \quad \boldsymbol{\delta'_2} = \pm\boldsymbol{a_2}, \quad \boldsymbol{\delta'_3} = \pm(\boldsymbol{a_2} - \boldsymbol{a_1}). \tag{2.5}$$

In tight-binding approaches [41], the Hamiltonian for the valence electrons in graphene is obtained by considering that electrons can only hop between neighboring atoms. If we limit the possible hoppings to nearest and next-nearest neighbors, we get the following tight-binding Hamiltonian

$$H = -t \sum_{\langle i,j \rangle, \sigma} (a_{\sigma,i}^\dagger b_{\sigma,j} + \text{H.c}) - t' \sum_{\langle i,j \rangle, \sigma} (a_{\sigma,i}^\dagger a_{\sigma,j} + b_{\sigma,i}^\dagger b_{\sigma,j} + \text{H.c}) \tag{2.6}$$

where $a_{\sigma,i}(a^{\dagger}_{\sigma,i})$ annihilates (creates) an electron with spin $\sigma = \frac{1}{2}, -\frac{1}{2}$ on site $\mathbf{R}_i$ on sublattice A (and similar with sublattice B), $t \sim 3$ eV is the nearest-neighbor hopping parameter and t' is the next nearest-neighbor hopping in the same sublattice. The energy bands derived by solving the secular equation associated to the tight-binding Hamiltonian of Eq. 2.6 [62] are

$$E_{\pm}(\mathbf{k}) = \pm t \sqrt{3 + f(\mathbf{k})} - t' f(\mathbf{k}) \tag{2.7}$$

with

$$f(\mathbf{k}) = 2 \, \cos(\sqrt{3} k_y a) + 4 \, \cos(\frac{\sqrt{3}}{2} k_y a) \cos(\frac{3}{2} k_x a). \tag{2.8}$$

The plus and minus signs in Eqs. 2.7 and **??** identify the π^* and π band levels, respectively.
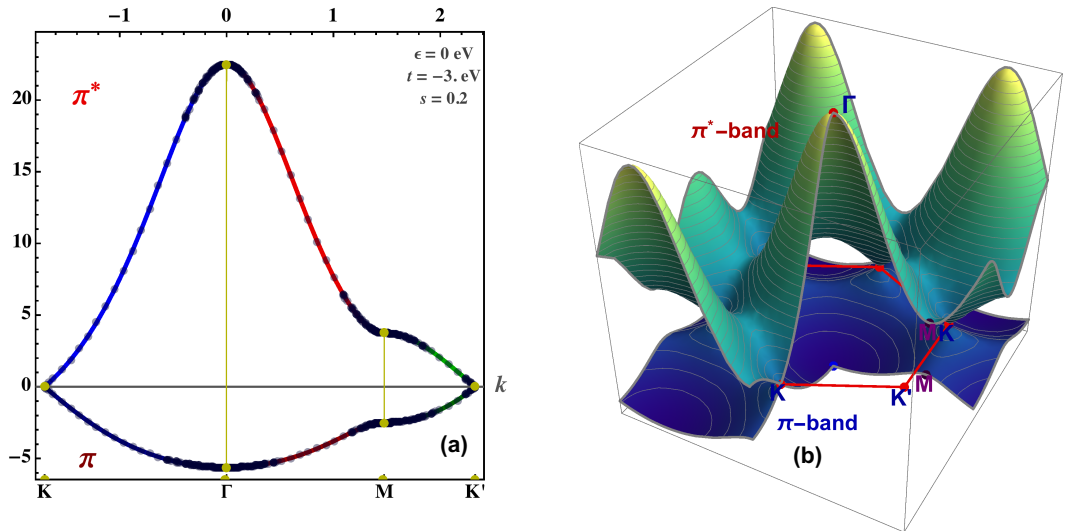
Figure 2.3: Energy spectrum (in unit of t) for finite values of $t = 3.0$ eV and $t' = 0.2t$ eV; (a) graphene band structure along high-symmetry path KΓMK', (b) a complementary view of (a) to evidence the linear band dispersion at the six Dirac points.

In Fig. 2.3, we show the full π and π^* band structure of graphene along the high-symmetry path KΓMK' of the first Brilluoin zone. With $t' = 0$ (nearest-neighbor approximation), the electron-hole band spectrum is symmetric around the Dirac-point energy (set to zero), while for finite values of t', the symmetry is broken, say, the π and π^* bands become asymmetric. The symmetric dispersion for t'=0 is obtained by expanding Eq. 2.8 close to $\mathbf{K}$ (or $\mathbf{K}'$), with the coordinates of Eq.(1.3). i.e., by considering a wave vector of the form as $\mathbf{k} = \mathbf{K} + \mathbf{q}$ (or $\mathbf{k} = \mathbf{K}' + \mathbf{q}$), with $q \ll K$ (or $q \ll K'$). By doing so, we obtain,

$$E_{\pm}(\mathbf{q}) \approx \pm v_F |\mathbf{q}| + O[(q/K)^2] \tag{2.9}$$

where $\mathbf{q}$ is the momentum measured relatively to the K points and $v_F \sim 10^6$ m/s, is the Fermi velocity. The density of π and π^* band levels, derived from Eqs. 2.7 and 2.8,
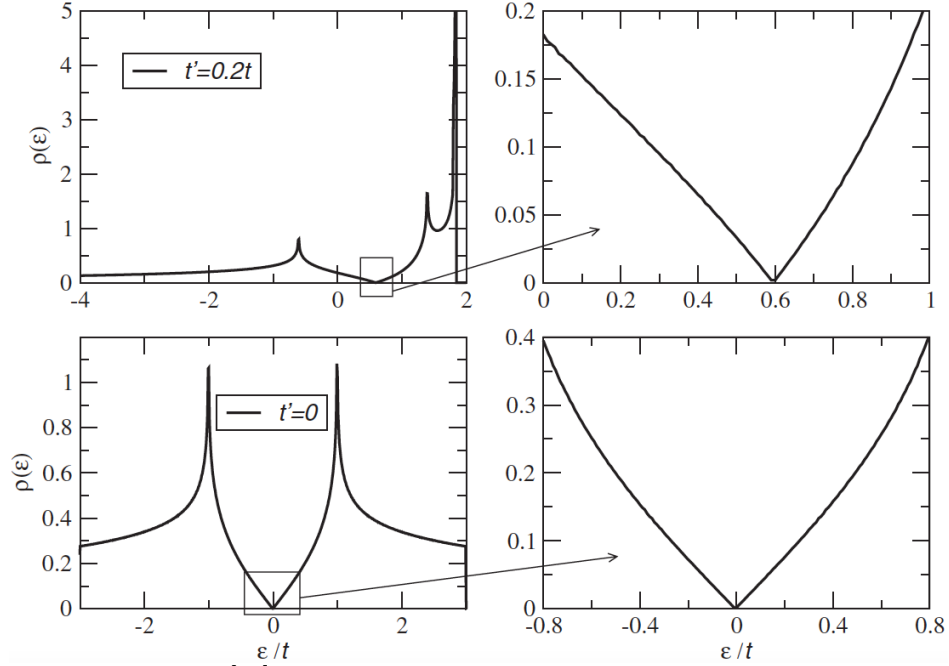
Figure 2.4: Taken from Ref [30]. Density of states per unit-cell as a function of energy in units of t computed from Eq.2.6, $t' = 0.2t$ (top) and $t' = 0$ (bottom) with the respective zoom of the density of states close to the neutrality point of one electron per site.

is reported in Fig. 2.4, which shows a semimetallic behavior for graphene in both the $t' = 0$ and $t' \neq 0$ cases, say, graphene is a zero band gap material. Close to the Dirac point, the dispersion is approximated by Eq. 2.9 and the density of states per unit-cell is given by

$$\rho(E) = \frac{2A_c}{\pi} \frac{|E|}{v_F^2} \tag{2.10}$$

where $A_c = 3\sqrt{3}a^2/2$ is the unit-cell area.

From the technological point of view, the Dirac cones, have been explored towards spintronic applications, because graphene exhibits a low spin–orbit (SO) gap, of the order of 10^{-3} eV, which makes it an ideal candidate for such utilization [63]. Subsequently, the engineering of graphene bands has rapidly lead to the development of semiconducting prototypes [64], an important step towards design of electronic and optoelectronic nanodevices. However, these nanodevices require larger band gaps, say, semiconductors or dielectric materials with direct or indirect band gaps ranging from ultraviolet to infrared through the visible range [65, 66], for which reason, other candidates among the group-IV elements, e.g., silicon (Si) and germanium (Ge) in honeycomb lattice, have been explored as we will see in the following.

2.2 Silicene and Germanene

Two-dimensional (2D) single layers of Si and Ge, i.e., silicene and germanene have been investigated by Takeda and Shiraishi [67] by first-principles calculations. Unlike graphene, where the A and B sublattices are in the same plane [Fig. 2.2], the two sublattices in silicene and germanene are relatively shifted in the direction perpendicular to the atomic plane, forming buckled structures [68, 69]. Previous studies have reported that silicene and germanene are characterized by a low or high bucking parameter [69, 70], as we see in Fig 2.5 where the calculated binding energies of silicene
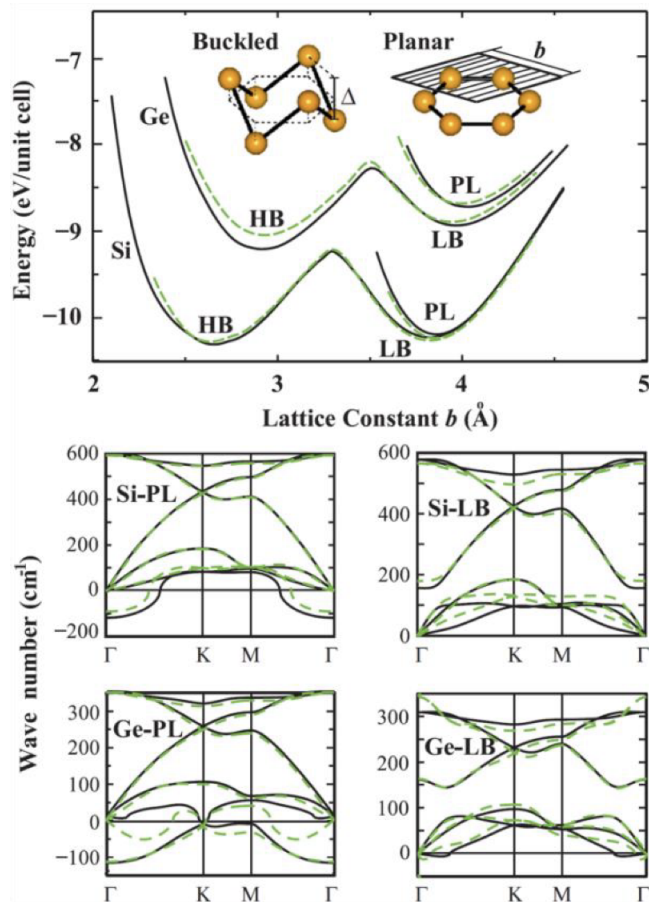
Figure 2.5: Taken from Ref [71]. (Top panel) binding energy versus lattice constant of planar and buckled silicene and germanene. Black and dashed green curves of energy are calculated by LDA using PAW potential and ultrasoft pseudopotentials, respectively. (Down panel) phonon dispersion curves obtained by force-constant and linear response theory are presented by black and dashed green curves, respectively.

and germanene as a function of the lattice constant are presented together with phonon dispersion curves [71].

Planar (PL), low-buckled (LB), and high-buckled (HB) honeycomb-like structures are all local minima on the binding energy curves. The PL configuration possess higher energy than the LB and HB counterparts (top panel) and the imaginary phonon

frequencies in a large portion of the Brillouin zone (down panel). On the other hand, it is demonstrated that optimized HB structures on the 2×2 supercell show an instability with a tendency towards clustering [71, 72].

Hence PL and HB structures do not correspond to real local minima, say, they are not stable [71, 73]. In contrast, the LB structures for silicene and germanene exhibit positive values for the phonon dispersion curve in the entire Brillouin zone (BZ) and thus are dynamically stable. The calculated Si-Si and Ge-Ge bond lengths for the LB structures are $2.2 - 2.4$ Å and $2.4 - 2.5$ Å, respectively [73, 38]. Compared to C, Si and Ge atoms have larger atomic radii. Consequently, π bonds in silicene and germanene, formed by coupling of adjacent p_z orbitals, are much weaker than those in graphene due to the longer interatomic distance. Despite the weakened π bonds, the stability of silicene and germanene is maintained by puckering induced dehybridization [38]. As a result, the perpendicular p_z orbital combines with s orbital [38, 74, 75].
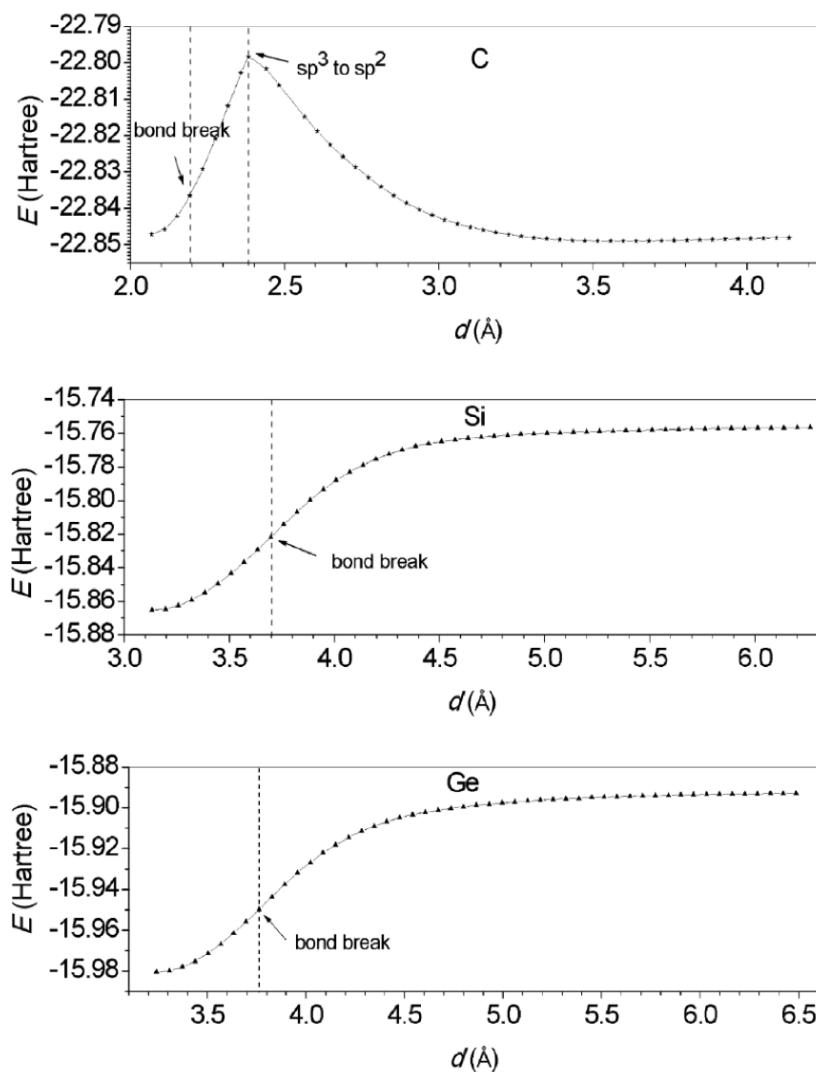

Figure 2.6: Taken from Ref [76]. The E (in Hartree) vs d (in Å) curves for lonsdaleite lattice from 3D to 2D structure evolution of carbon, silicon, and germanium. The dashed lines indicate the critical point for bond breaking.

The latter was explored by Wang [76], in elementary 2D phases by carbon, silicon, and germaniun. Three dimensional (3D) lonsdaleite crystals of C, Si and Ge were adopted as initial configurations. The 3D to 2D transformation was simulated by stretching the layer spacing d between two neighboring hexagonal basal planes gradually together with full relaxations of the in-layer atomic position and the lattice parameter. The evolution of bonding state can be effectively inspected from the variation of total energy E, as depicted in Fig. 2.6. For the carbon phase, there is an apparent turning point from endothermic to exothermic in the E vs d curve at $d \sim 2.38$ Å, which is obviously due to the change of orbital hybridization from sp^3 to sp^2 [38]. However, for the silicon and germanium phases, the total energy E keeps increasing with the increasing of d, suggesting no such sp^3 to sp^2 transition [38, 76]. In other words, silicene and germanene keep a sp^3-like state i.e., a mixed $sp^3 - sp^2$ orbital hybridization [38, 77].
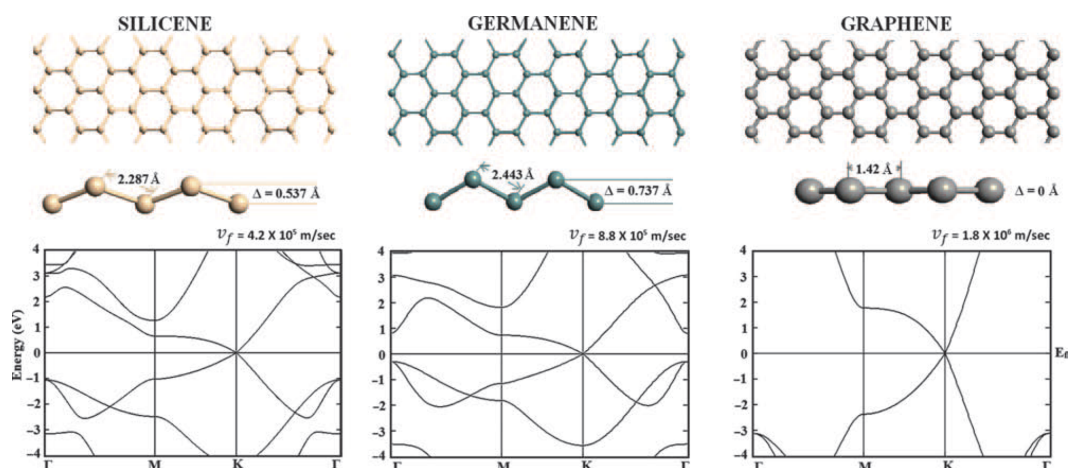
Figure 2.7: Taken from Ref [77]. Geometric conformation and band structure of silicene, germanene and graphene.

In spite of the low buckled geometry and mixed $sp^3 - sp^2$ hybridization, the band structures of silicene and germanene resemble that of graphene at lower energies, that is, the π and π^* bands cross linearly at the Fermi level, forming the Dirac cone at the Dirac points as shown in Fig. 2.7 [77]. Then, silicene and germanene also are zero band gap materials with unique electronic properties like graphene. Additionally, silicene and germanene have been recognized to have two principal advantages with respect to graphene: (i) a large spin-orbit induced band gap of 1-30 meV, with respect to the 10^{-3} meV value predicted for graphene [78, 79], which has been confirmed by an experimental realization of the quantum spin Hall effect; and (ii) a tunable band gap in the presence of a perpendicular electric field [80, 81], with band gap values of several meV that increase linearly with increasing the field strength. These advantages makes them immediate candidates for nanoelectronics.

2.3 Graphene nanoribbons

We now move to interesting features found in graphene by a simple variation of its dimensionality [82]. If graphene is confined to one-dimension (1D) into nanoribbons narrower than 10 nm in width, it changes from a semimetal into a semiconductor material with appreciable band gap on eV scale [83, 84]. The successful synthesis of graphene nanoribbons with precision of 5 and 10 mn has been recently reported on germanium substrates via chemical vapour deposition [85]. The semiconducting behavior of graphene nanoribbons allows for substantial modulation of their conductance and enabling their application in semiconductor logic [86], high-frequency communication devices [87], optoelectronics [88], photonics [89] and sensor technology [90] in which a band gap is needed to achieve high performance.
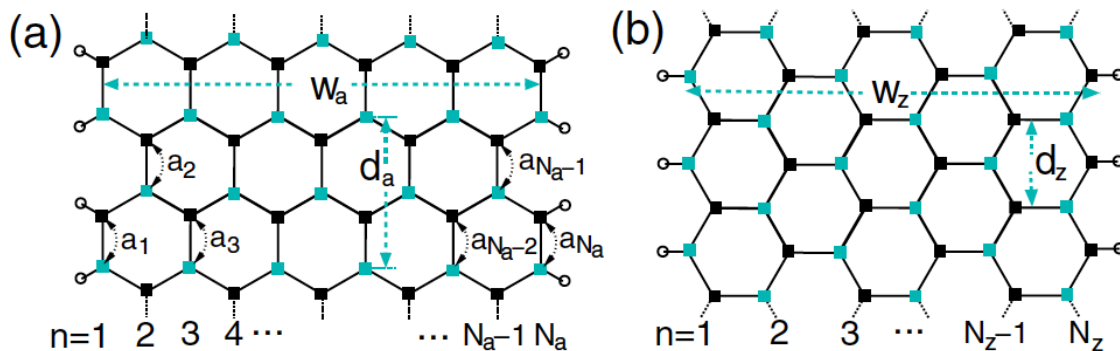
Figure 2.8: Taken from Ref [84]. (a) Representation of an armchair graphene nanoribbon. (b) Representation of a zigzag graphene nanoribbon. The empty circles denote hydrogen atoms passivating the edge carbon atoms. The black and gray rectangles represent atomic sites belonging to different sublattice in the graphene structure. The unit-cell distances are denoted by d_a and d_z and ribbon widths by w_a and w_z for armchair and zigzag graphene nanoribbons, respectively.

Geometrically, at the nanometer scale two shaped edge conformations are mainly studied in graphene nanoribbons called armchair and zigzag [Fig. 2.8], which are respectively characterized by dimer lines (N_a) and zigzag chains (N_z) across the graphene nanoribbon width [84]. Nearest neighbor tight-binding approaches [91, 92, 84] with appropriate boundary conditions based on π-states, and semiclassical models [93, 94, 84], based on a two-dimensional free massless particle Dirac equation with an effective Fermi velocity ($v_F \sim 10^6$ m/s), have predicted that graphene nanoribbons with armchair shaped edges can be either metallic or semiconducting depending on their widths, and that graphene nanoribbons with zigzag shaped edges are metallic with peculiar edge states on both sides of the ribbon regardless of its width.

These methodologies are known to describe very well the low energy properties of graphene, however a proper description of edge effects (armchair and zigzag) in nanometer sized ribbons can be achieved only considered by first-principle calculations [84, 95]. Unlike graphene, the bonding characteristics between atoms change abruptly at the edges [84]. Furthermore, zigzag graphene nanoribbons present a narrow-band edge states at the Fermi level (as will discussed bellow) implying possible magnetization at

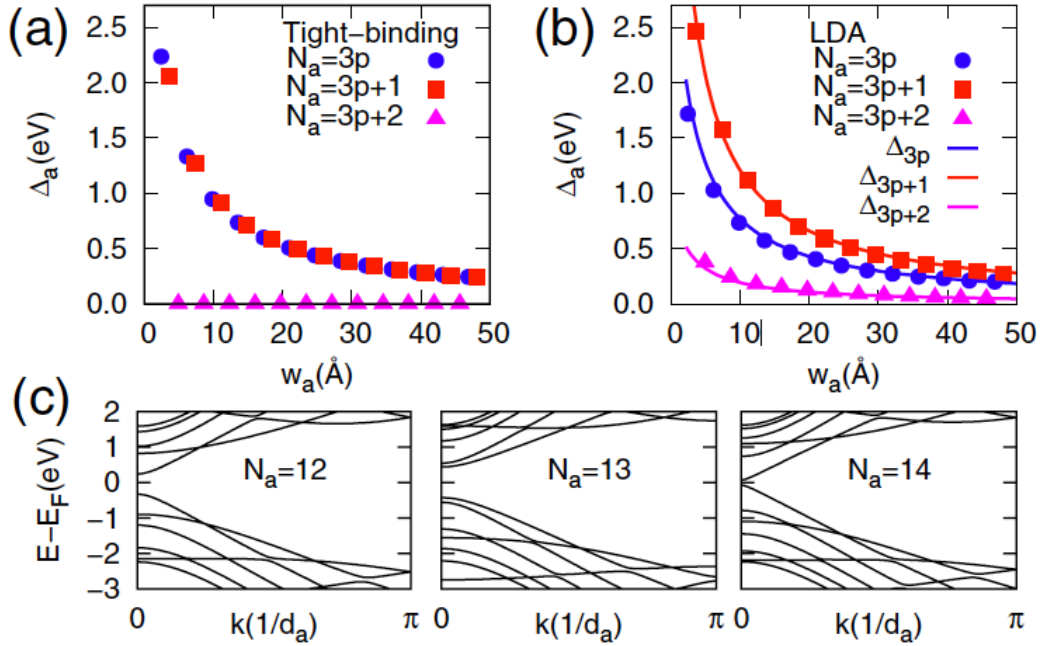Figure 2.9: Taken from Ref [84]. The variation of band gaps of armchair graphene nanoribbons as a function of width (W_a) from (a) Tight binding calculations (with hopping parameter $t = 2.7$ eV) and (b) first-principles calculations. (c) LDA band structures of armchair graphene nanoribbons with dimer lines $N_a = 12, 13, 14$, respectively. Fermi level set to zero.

the edges [84], then the spin degree of freedom is also an important point to consider.

In Fig. 2.9 we see that armchair graphene nanoribbons are semiconductors with band gaps which decrease as a function of increasing ribbon widths (W) [84]. However three distinct families are detected in function of the band gap and width variation denoted as N = 3p, N = 3p + 1 and N = 3p + 2, where p is a positive integer [84]. As it was expected, the results from nearest neighbor tight-binding model are quite different from those by first-principles calculations. The tight-binding results using as hopping parameter $t = 2.7$ eV between π-electrons [Fig. 2.9(a)] show that armchair graphene nanoribbons are metallic for the N = 3p + 2 family. Otherwise, graphene nanoribbons are semiconducting for the N = 3p and N = 3p + 1 families.

By first-principles calculations, we can observe that graphene nanoribbons with a metallic behavior do not appear with widths smaller that 5 nm [84], and the band gap values of the three different families are now well separated as evidenced in Fig. 2.9(b). For instance, if the $N_a = 3p$ family is considered with p= 3, we can observe a tight-binding band gap value of ~ 2 eV and an *ab initio* band gap of ~ 2.5 eV. Furthermore, the first-principles band structures of armchair graphene nanoribbons with $N_a = 12, 13, 14$ exhibit direct band gaps at Γ point ($kd_a = 0$) in all cases. The semiconducting behavior of armchair graphene nanoribbons is due to the quantum confinement [84] which can be described as:

$$\Delta_{BG} = \frac{1}{W_a} \tag{2.11}$$

where the band gap (Δ_{BG}) is inversely proportional to the ribbon width (W_a).

The band structure of graphene nanoribbons with zigzag shaped edges calculated by tight-binding approach [96] [Fig. 2.10(a)-(c)] shows that the highest valence bands and the lowest conduction bands always degenerate at $k = 0$ (Γ point) when the spin degree of freedom is not considered. The quasi-flat band dispersion originates a high-DOS peak structure (see Chater 5) at the Fermi level that plays an important roll in the understanding of the plasmonic properties of virtual gapless graphene nanaribbons [97, 98].
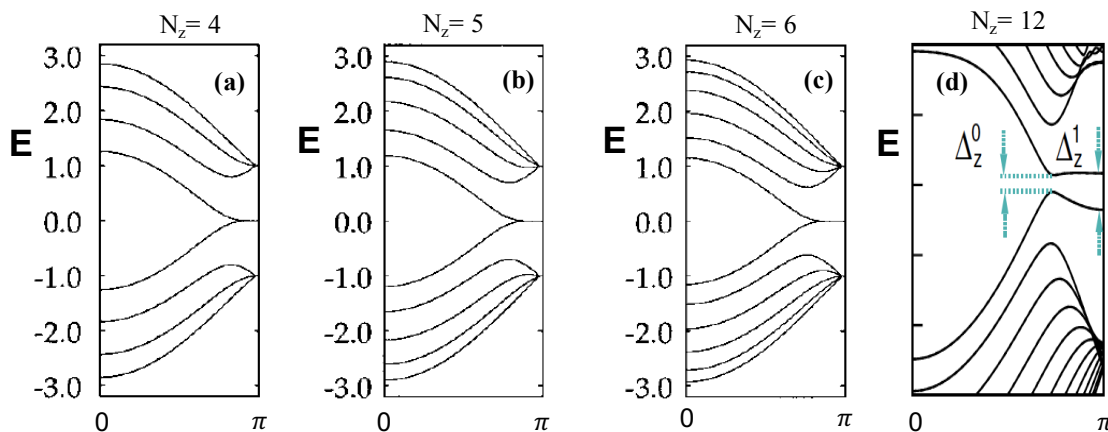
Figure 2.10: Taken from Refs. [96, 84]. Band structures of zigzag graphene nanoribbons with $N_a = 4,5,6$ and 12. (a)-(c) Tight-binding model and (d) L(S)DA approach. Fermi level set to zero.

When the spin degrees of freedom are included within first-principle calculations [Fig. 2.10(d)], i.e., by using the local spin density approximation (LSDA) [99], the zigzag graphene nanoribbons are predicted to have a magnetic insulating ground state with ferromagnetic ordering at each zigzag edge and antiparallel spin orientation between the two edges [96, 84]. Basically, the band gaps in zigzag graphene nanoribbons originate from the staggered sublattice potentials resulting from the magnetic ordering, which introduce band gaps for electrons on a honeycomb hexagonal lattice [100, 84]. This is realized because the opposite spin states on opposite edges occupy different sublattices (black rectangles on the left side and gray ones on the right see Fig. 2.8). Thus we can observe that graphene nanoribbons with homogeneous armchair or zigzag shaped edges all have band gaps which decrease as the ribbon widths increase.

Chapter 3

Theory

Density functional theory (DFT) is the most popular and useful computational approach to study the equilibrium electronic properties of many-electron systems as well as a wide variety of nanomaterials, whose calculations were unthinkable just a few decades ago [101]. DFT popularity stems from its speed, lower computational cost, and computational efficiency as well a good balance between reasonable and useful accuracy of several physical properties (e.g., bond lengths, vibrational frequencies, elastic constants are calculated with errors of less than a few percent). DFT approaches are sufficiently accurate for many applications in solid state physics, chemistry, materials science and many other fields [102]. Particularly, DFT based on the Kohn-Sham formalism is the most widely used many-body method for electronic structure calculations of atoms, molecules, solids, and solid surfaces [101, 102, 103].

Instead, plasmons in solid state materials are typically triggered by electron-beam radiation or photocurrents below a few eV, and charged ions with incident kinetic energy of the order of $0.1 - 1$ keV [104, 105]. In the present context, we consider introducing an electron or a photon, with incident momentum $\mathbf{q}$ and frequency ω, which weakly perturbs the Kohn-Sham electrons of the system under consideration. With this in mind, the intrinsic and extrinsic plasmonic properties of 2D materials can be explored in the framework of *ab initio* time-dependent density functional theory (TDDFT) at the level of the random-phase approximation (RPA).

In this Chapter, we then briefly revise the key points of DFT methodology, which will be used to obtain the Khon-Sham single-particle orbitals and energies necessary to compute the dielectric properties of our systems within TDDFT+RPA framework. This framework has been proved to be sustainable to investigate the energy loss function and plasmon dispersion in graphene-related and beyond-graphene materials [106, 19, 107, 20].

3.1 Theoretical Foundation

A system composed of N electrons interacting with one another via the Coulomb interaction, and moving inside an external potential V_{ext}, (e.g., the periodic ion core potential in crystals) can be described by the following Hamiltonian[1]:

$$\hat{H} = -\frac{\hbar^2}{2m_e}\sum_i^N \nabla_i^2 + \sum_i^N V_{ext}(\mathbf{r}_i) + \frac{1}{2}\sum_{i\neq j}^N \frac{e^2}{4\pi\varepsilon_0|\mathbf{r}_i - \mathbf{r}_j|}, \tag{3.1}$$

by using atomic units, Eq. (3.1) can be rewritten as:

$$\hat{H} = -\frac{1}{2}\sum_i^N \nabla_i^2 + \sum_i^N V_{ext}(\mathbf{r}_i) + \frac{1}{2}\sum_{i\neq j}^N \frac{1}{|\mathbf{r}_i - \mathbf{r}_j|}. \tag{3.2}$$

It is well known that Eq. (3.2) is not solvable exactly. A viable way to Eq. (3.2) is given by DFT, which states that all the relevant and observable properties of the ground state of a many-electron system depend only on the ground state electron density.

The latter was first developed by Thomas [109] and Fermi [110], who working independently, proposed a statistical model in 1927 to approximate the equilibrium distribution of electrons in a many-electron atom. This model represented the total electron kinetic energy as function of the electron density $n(r)$:

$$T_{TF}[n] = \frac{3^{5/3}\pi^{4/3}}{10}\int d^3 r\, n^{5/3}(\mathbf{r}). \tag{3.3}$$

Eq. 3.3 can be combined with the classical expressions for the nuclear-electron and electron-electron interactions (both expressed in terms of $n(\mathrm{r})$) to obtain the todal energy density functional

$$ETF[n] = T_{TF}[n] + \int d^3 r\, V_{EXT}(\mathbf{r})n(\mathbf{r}) + \frac{1}{2}\int d^3 r_1 d^3 r_2 \frac{n(\mathbf{r}_1)n(\mathbf{r}_2)}{|\mathbf{r}_1 - \mathbf{r}_2|}, \tag{3.4}$$

in Eq. 3.4 the second term is the electron interaction with the external potential and the third term represents the classical Coulomb interaction between two charge densities, that is the Hartree energy. Later on, Dirac [111] added a term to this functional to take into account the exchange interaction between electrons, due to the Pauli exclusion principle. The result was the Thomas-Fermi-Dirac total energy functional::

$$E_{TFD}[n] = E_{TF}[n] - \frac{3^{4/3}}{4\pi^{1/3}}\int d^3 r\, n(\mathbf{r})^{4/3} \tag{3.5}$$

in which the last term is an approximation of the exchange energy. The problem with the Thomas-Fermi model is that it relies on approximations that are indeed too crude to get good results also in the case of simple atoms, however their idea of expressing the total energy as a functional of the electron density turned out to be very useful, as we will explain in the following.

---

[1]Regarding the degrees of freedom of the"positively charged" background responsible of V_{ext}, we are assuming that they can be viewed as frozen, as in the Born-Oppenheimer approximation[108]; their contribution to the Hamiltonian Eq. (3.1) and to the total energy functional Eq. (3.7) is indeed an additive, though configuration dependent, constant as long as only the electrons' degrees of freedom are concerned.

3.1.1 The Hohenberg-Kohn theorems

DFT is based on the two Hohenberg-Kohn theorems [112], which allow the construction of an exact theory of many-body system applicable to all system of interacting electrons whose Hamiltonian has the form Eq. (3.2).

Theorem 1: *If the Ground States of two many electron system, each containing N electrons, one with external potential $V_1(\mathbf{r})$, and the other with external potential $V_2(\mathbf{r})$, have the same electron density $n_0(\mathbf{r})$, then the two external potential differ only by an additive constant C, that is must be:*

$$V_1(\mathbf{r}) = V_2(\mathbf{r}) + C. \tag{3.6}$$

The first Hohenberg-Kohn theorem states that the external potential $V_{ext}(\mathbf{r}_i)$, and then the full many-body Hamiltonian Eq.(3.1), is determined uniquely by the ground state electron density $n_0(\mathbf{r}_i)$. As a consequence, since the Hamiltonian is fully determined, except for a constant shift in energy, so are the many-body wavefunctions (ground state and excited states as well). So, at least in principle, all the properties of the system are determined by the ground state electron density $n_0(\mathbf{r})$.

One of the most important consequences is that all the quantities can be expressed as functional of the electron density. This allow to define the total energy functional $E[n]$ as:

$$E[n] = T[n] + E_{int}[n] + \int d^3r V_{EXT}(\mathbf{r})n(\mathbf{r}), \tag{3.7}$$

in which we wrote explicitly as functionals the kinetic energy part of the total energy, $K[n]$, and the electron-electron interaction part $E_{int}[n]$.

Theorem 2: *For each external potential V_{ext} the total energy functional $E[n]$, defined by (3.7), reach its global minimum for the ground state density n_0 and the value $E[n_0]$ is the ground state energy of the system.*

The form of the total energy functional allows also the definition of the universal Hohenberg and Kohn functional $F_{HK}[n]$ as:

$$F_{HK}[n] = T[n] + E_{int}[n]. \tag{3.8}$$

With universal it is meant that the (3.8) is the same for all the many electrons system, regardless the external potential acting on them. At this point it is interesting to note that the two HK theorems and all DFT theory can be applied to all many body problems (not only to many electron problems) provided that the universal functional F_{HK} is changed accordingly.

3.2 The Kohn-Sham formalism

Although, the Hohenberg-Kohn theory is exact in principle, it can not be exploited in practice because the exact Hohenberg-Kohn functional Eq. (3.8) is not known. As already observed in the case of the Thomas-Fermi model, the problem lies both in the kinetic energy term $K[n]$ and in the electron-electron interaction term E_{int}.

Regarding the latter, one needs to model the many-body nature of the electron-electron interaction and state it as a functional of the electron density. The kinetic energy term, on the other hand, can be calculated explicitly as a sum of one body terms (see the first term in $\hat{H}$ in Eq. (3.1)), but it can not be easily expressed as a functional of the electron density. A way of overcoming these two problems is given by the Kohn-Sham formalism [113]. It consist in replacing the interacting N-electron system with a non-interacting N-electron system, in which the non-interacting electrons move in a effective external potential (V_{eff}) that depends on the electron density.

To make this substitution two assumptions consistent with the Hohenberg-Kohn theorems are necessary:

1. The ground state density of the interacting N-electron system in the external potential V_{EXT} must be representable by a ground state density of an auxiliary non-interacting system.

2. The auxiliary non-interacting Hamiltonian H_{aux} has the usual kinetic energy operator and an effective potential V_{eff}.

These assumptions allow to express the H_{aux}, which may also depend on the spin degrees of freedom σ, as :

$$H_{aux} = -\frac{1}{2}\nabla^2 + V_{eff}^{\sigma}(\mathbf{r}). \tag{3.9}$$

With the first assumption the electron density is given as the sum of the one-electron densities given by the square moduli of the N one-electron wave functions[2]:

$$n(\mathbf{r}) = \sum_{\sigma}\sum_{i}^{N'} |\psi_i^{\sigma}(\mathbf{r})|^2. \tag{3.10}$$

So we can still write the total energy functional as:

$$E_{KS}[n] = T_s[n] + E_{Hartree}[n] + E_{xc}[n] + \int d^3 r V_{EXT}(\mathbf{r})n(\mathbf{r}). \tag{3.11}$$

In Eq. (3.11) is used the non-interacting kinetic energy functional[3]:

$$T_s[n] = \sum_{\sigma}\sum_{i}^{N'} |\nabla\psi_i^{\sigma}(\mathbf{r})|^2, \tag{3.12}$$

---

[2]At this point we include explicitly the spin degree of freedom in the wave-function, in this way we must pay attention to the upper extreme of the summation on i that becomes N'.

[3]It is worth noticing that the kinetic energy functional $T[n]$ in Eq. (3.8) is in general different from the non interacting kinetic energy functional $T_s[n]$ defined in Eq. (3.12); their difference can be viewed as arising from many-body interaction that are excluded in the independent electron picture so they are somehow included in the exchange and correlation part $E_{xc}[n]$.
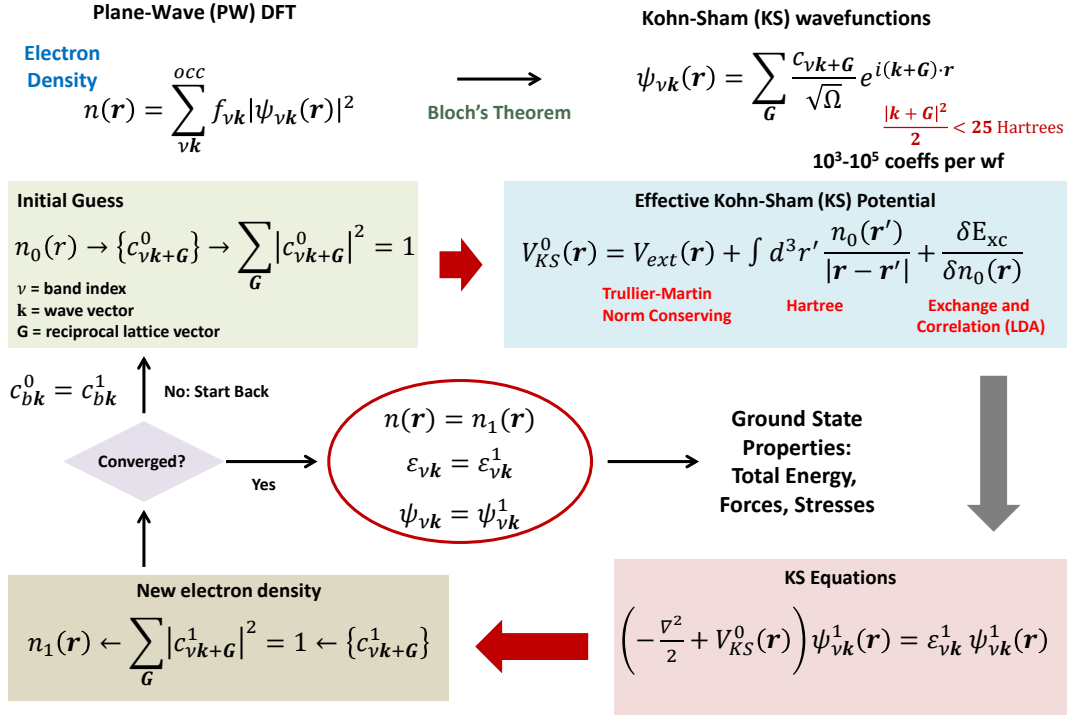
Figure 3.1: Flow chart illustrating the Kohn Sham self consistent procedure.

which is indeed a functional of n due to the density dependence is implicit in the one electron wavefunctions, $\psi_i^\sigma = \psi_i^\sigma[n]$, and it also depends explicitly on the classical electron-electron interaction energy ($E_{Hartree}$):

$$E_{Hartree}[n] = \int d^3r_1 d^3r_2 \frac{n(\mathbf{r}_1)n(\mathbf{r}_1)}{|\mathbf{r}_1 - \mathbf{r}_2|}, \tag{3.13}$$

all the other many-body electron-electron interaction are included in the so called Exchange and Correlation term $E_{xc}[n]$.

This new formulation of the problem allows to set up an iterative research of the ground state density $n_0(\mathbf{r})$ in a self-consistent cycle, depicted in the flow chart of Fig. 3.1. This procedure is illustrated in more details in the following sections, together with the approximations hidden within.

3.2.1 The self-consistent Kohn-Sham cycle

The self consistent (SC) Kohn-Sham cycle is quite similar to the Hartree-Fock cycle for calculating the ground state of many electron atoms [114]. The preliminary step of the SC cycle is an initial guess for the total electron density $n(\mathbf{r})$. The initial electron density can then be used to calculate the total energy functional for the first step. At this point the next step would be operating a variation in the electron density that reduces the total energy. However, as already pointed out, this operation is not possible because it is not possible to have a simple expression of the kinetic part as a density functional. The problem is then transferred on the wave-function exploiting Eq. (3.12)

and Eq. (3.10). In fact the minimum of the total energy can be obtained by equating to zero the variation of the total energy with respect to the wave-function instead[4]:

$$\frac{\delta E_{KS}}{\delta \psi_i^{\sigma*}(\mathbf{r})} = \frac{\delta T_s}{\delta \psi_i^{\sigma*}(\mathbf{r})} + \left[\frac{\delta E_{ext}}{\delta n(\mathbf{r})} + \frac{\delta E_{hartree}}{\delta n(\mathbf{r})} + \frac{\delta E_{xc}}{\delta n(\mathbf{r})} \right] \frac{\delta n(\mathbf{r})}{\delta \psi_i^{\sigma*}(\mathbf{r})} = 0, \tag{3.14}$$

subject to the orthonormalization condition

$$\langle \psi_i^\sigma | \psi_j^{\sigma'} \rangle = \int d^3 r \psi_i^{\sigma*}(\mathbf{r}) \psi_j^\sigma(\mathbf{r}) = \delta_{i,j} \delta_{\sigma,\sigma'}. \tag{3.15}$$

Equations (3.14) and (3.15) can be put together, adding the Lagrange multipliers ε_i^σ and noting that

$$\frac{\delta T_s}{\delta \psi_i^{\sigma*}(\mathbf{r})} = -\frac{1}{2} \nabla^2 \psi_i^\sigma(\mathbf{r}) \quad \text{and} \quad \frac{\delta n(\mathbf{r})}{\delta \psi_i^{\sigma*}(\mathbf{r})} = \psi_i^\sigma(\mathbf{r}), \tag{3.16}$$

to form a Schroedinger-like equation:

$$\left(H_{KS}^\sigma - \varepsilon_i^\sigma \right) \psi_i^\sigma(\mathbf{r}) = 0, \tag{3.17}$$

where the Kohn-Sham Hamiltonian is given by

$$H_{KS}^\sigma = -\frac{1}{2} \nabla^2 + V_{KS}^\sigma \tag{3.18}$$

and the Kohn-Sham potential V_{KS} is nothing but the effective potential defined in (3.9):

$$V_{KS}^\sigma = \frac{\delta E_{ext}}{\delta n(\mathbf{r})} + \frac{\delta E_{hartree}}{\delta n(\mathbf{r})} + \frac{\delta E_{xc}}{\delta n(\mathbf{r})} = V_{ext}(\mathbf{r}) + V_{Hartree}(\mathbf{r}) + V_{xc}^\sigma(\mathbf{r}). \tag{3.19}$$

Coming back to the SC cycle, the initial guess for the electron density is plugged into Eq. (3.19) to obtain the KS potential. Then the KS Hamiltonian is calculated and the KS equation are solved to obtain the eigenvalues ε and the eigen-functions ψ. The eigen-functions are then used to calculate a new electron density $n(\mathbf{r})$ using Eq. (3.10), using which one recalculates the KS potential and so on. The cycle is called self-consistent because the electron density obtained in the ith cycle is necessary to obtain the potential in the $(i+1)^{th}$. The cycle stops when a convergency criterion is satisfied. There are a lot of possible choices in setting up a convergency criterion. A possible choice is that the difference in two output quantity (for instance the total energy, the orbital energies or the density itself[5]) calculated with the electron densities of two (or more) subsequent steps is less than a given (small) value. The last electron density is the main output of the SCF-cycle and is used to obtain all the other interesting quantities.

---

[4]Eq. (3.14) is obtained by varying with respect to the complex conjugate of the wave-function ψ^* as is done in all variational problem to obtain the secular equation for the wave-function ψ Eq. (3.17); varying with respect of the wave-function directly would have lead to secular equation that are the complex conjugate of Eq. (3.17) that give the same result because the Kohn-Sham Hamiltonian Eq. (3.18) is an hermitian operator.

[5]Provided a certain definition of difference in the last two cases

3.3 DFT approximations

As stated to solve practical problems with DFT method outlined above some approximations are necessary. This section is devoted to the description of some of the approximation that will be encountered in the following chapters. It is necessary to stress that the topics covered are not exhaustive; for a more detailed discussion see Refs. [115, 116]

3.3.1 Exchange and Correlation "Flavor"

The first approximation we will encounter is the most important from a fundamental point of view, because is the only one that is necessary and is not used to ease the procedure. It concerns directly the Hohenberg and Kohn functional. As we stated in Eq. (3.2) the direct application of the Hohenberg-Kohn theorems in solving the many-electron problem is impossible due to the difficulty in expressing the kinetic energy term as a density functional and in modeling the complicated many-body electron-electron interaction. The Kohn-Sham formalismo allows to "simplify" the kinetic energy part, but still nothing has been done for the electron-electron interaction part. We already said that the exact Hohenberg-Kohn functional is not known; in the formulation we used all the unknown part in the Hohenberg-Kohn functional is in the term we called exchange-correlation term, E_{xc}, in the total energy functional Eq.(3.11), or the exchange-correlation potential, V_{xc}, in defining the Kohn-Sham effective potential Eq. (3.19). This term can be rewritten as:

$$E_{xc}[n] = \int d^3 r n(\mathbf{r}) \varepsilon_{xc}([n], \mathbf{r}) \tag{3.20}$$

where the ε_{xc} is an energy per particle and is in general a complicated "function" of the position $\mathbf{r}$ and of the values of the density and of the density derivatives $\{n(\mathbf{r}'); \nabla n(\mathbf{r}')\}$ calculated in principle for all the possible $\mathbf{r}'$.

Indeed there are several possible choices for V_{xc}, or equivalently for ε_{xc}; we are not going to explore all of them. In fact it does not exist the best exchange-correlation functional, because every different physical situation has its proper approximation and so its "best" exchange-correlation functional. However the functionals can be grouped into classes according to some of their main features.

One of these classes is the class of *Local* functionals. A functional is local if ε_{xc} is a function of the position $\mathbf{r}$ and of the electron density (and eventually its derivatives) calculated in the same position $\mathbf{r}$. Local functionals are, for example, the functionals that use the Local Density Approximation (LDA) [117, 99, 118] and its generalization to include the dependence of ε_{xc} on the derivatives of the density, called Generalized Gradient Approximation (GGA) [119]; in the case of LDA and GGA the exchange-correlation energy is given by:

$$E_{xc}^{LDA} = \int d^3 r n(\mathbf{r}) \varepsilon_{xc}^{LDA}(n(\mathbf{r}), \mathbf{r}), \tag{3.21}$$

$$E_{xc}^{GGA} = \int d^3 r n(\mathbf{r}) \varepsilon_{xc}^{GGA}(n(\mathbf{r}), |\nabla n|, \dots, \mathbf{r}). \tag{3.22}$$

In the case of non-local functional [120] it is not possible to write a simple expression like Eq. (3.21) or Eq. (3.22) because the calculation of $\varepsilon_{xc}([n], \mathbf{r})$ includes the evaluation of the density n, and eventually its derivatives ∇n, in $\mathbf{r}$ and in other points $\{\mathbf{r}_i\}$.

Another class of density functional is obtained if the exchange-correlation term depends explicitly on the one-electron orbitals, obtainig a so called Orbital-Dependent functional. Among these, we mention the LDA+U method [121], in which an artificial potential term (U) acting only on localized orbitals (like d and f orbitals in transition elements) is added to a standard LDA functional. Finally, in the so called Hybrid functionals [122], where a non-local density term is combined to the exact Hartree-Fock exchange term.

3.3.2 Periodic and finite-size calculations

DFT can be used to study both finite size entity and large bulk materials. Finite size entities are, for instance, atoms and molecules and in general all systems that are composed by a (fixed) finite number of atoms and then have a finite number of electrons. In this case the cluster of atom is considered isolated in the space and the DFT algorithm of Fig. 3.1 can be applied directly.

On the contrary, bulk property of macroscopic materials can be studied, by means of DFT methods, with periodic calculations. A periodic calculation is set up by constructing a fundamental finite size cluster of atoms, the unit cell. In this way the number of electron in the unit cell is finite. The unit cell is periodically replicated using some displacement lattice vectors $\{\mathbf{R_i}\}$ to construct the bulk solid, that has infinite dimension and then is made by an infinite number of atoms therefore having an infinite number of electron. The periodic description allow to apply the Bloch theorem [123] and express the wavefunctions as Bloch states:

$$\psi_{i,\mathbf{k}} = e^{i\mathbf{k}\cdot\mathbf{r}} u_i(\mathbf{r}) \tag{3.23}$$

where the function $u_i(\mathbf{r})$ has the same periodicity of the lattice[6] and where we introduced the band index i. Moreover the periodic properties of the wavefunctions are reflected in the density that is periodic and that is calculated summing over the occupied bands that are half the number of the electrons in the unit cell. Indeed the complexity of infinite number of electrons is recovered because the calculation of the density is made integrating over $\mathbf{k}$. The $\mathbf{k}$ integral however can be replaced by a summation over a finite number of k-points in the first Brillouin zone (BZ). This is indeed an approximation and is usually done by the method of Monkhorst and Pack [124], that consist in sampling the BZ with points that are not connected with one another by symmetry operations, or, equivalently, by sampling the irreducible part of the first BZ, that is the part of the BZ that can be used to construct the full BZ using symmetry operations.

---

[6]The periodicity of u_i allow to write $u_i(\mathbf{r}) = \sum_{\mathbf{G}} c_{i,\mathbf{G}} e^{i\mathbf{G}\cdot\mathbf{r}}$, where $\{\mathbf{G} : \mathbf{G} \cdot \mathbf{R} = 2\pi l, l \in \mathbb{N}\}$ is the reciprocal lattice. This makes the plane-waves basis set the natural, but not the only, choice in periodic calculation.

It should be stressed that the distinction between finite size and periodic calculation is not neat. In fact there exist intermediate situation, for system with periodicity only in one or two dimensions, that can be modeled by periodic super-cells or using finite-size-like calculation in the non-periodic direction. We also remark that the periodic calculation can be applied to finite size systems, like atoms and molecules, by means of the periodic super-cells, this is done mainly to use the Bloch representation. On the contrary a big finite size calculation can be used to obtain information on bulk properties, when one wnats to avoid a periodic calculation.

3.3.3   All electron and Pseudo-Potentials

A way to ease the computational burden and reduce the convergency times of DFT codes is to define suitable pseudo-potentials eliminating inert electrons, which do not participate directly to the process understudy [see [115], Chapter 11]. The main underlying idea is that, for most purposes, the core electrons can be viewed as tightly bound to the ionic cores and relatively inert. This observation leads to substituting core electrons with an approximately averaged screening in uence on the ionic potential that is parametrized by pseudo-potentials. Among the advantages of this procedure we mention the reduced electron number and basis set size, especially in periodic calculations where the sharply peaked core orbitals require large numbers of plane waves to be reproduced. Construction of a pseudo-potential consists in finding a potential whose eigenfunctions perfectly match the original all electron wavefunctions at electron-nuclear distances r larger than a given cut-off distance r_{cut}. This usually consists in removing the divergent part of the potential for $r \to 0$, as shown schematically in Fig. 3.2. The main disadvantages are that, on the one hand, no information can be obtained from core electrons, and, on the other hand, the pseudization procedure gives valence wavefunctions with wrong behavior at $r < r_{cut}$; a classical example is the pseudized 2_s wavefunction of a many-electron atom that has no nodes, while it should have one node.

Choosing of the correct pseudo-potential in a DFT calculation is one of the most difficult and important parts and, even in this case, it is not possible to define a perfect pseudo-potential for all situations concerning a given atom. Usually, the pseudo-potentials are tested with available experiments on some measurable quantities. It is worth noticing that there are a numerous standard techniques for pseudo-potential generation. Here, we mention only the two big categories of norm-conserving [125] and ultra-soft [126] pseudopotentials. Norm-conserving pseudo-potentials enforce the condition to the norm of their eigenfunctions that must equal the norm of the original all-electron eigenfunctions for integrations above r_{cut}. Ultra-soft pseudo-potentials release this condition to further decrease the size of the basis set. In some situations the desired output quantities are directly related to core electrons, so the use of pseudo-potential is not possible and all-electron calculations are necessary.
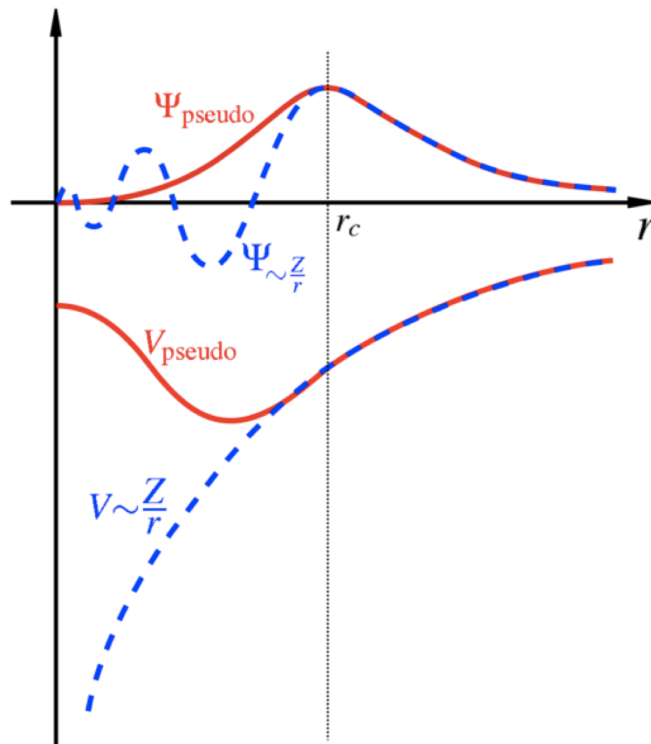
Figure 3.2: Schematic comparison between the Coulomb potential and a possible choice of pseudo-potential; in the picture is also shown the difference between the all-electron and the pseudo-eigenfunctions.

3.3.4 Basis set

In 3.2.1 we saw that the Kohn Sham self-consistent cycle result in solving a time-independent Schroedinger-like problem Eq. (3.17), that consist in finding eigenfunction and eigenvalues of the Kohn-Sham Hamiltonian Eq. (3.18).

A way of easing the procedure is expanding the generic one electron wave-function in components of a suitable basis set $\{\phi_j\}$:

$$\Psi(\mathbf{r}) = \sum_{j}^{N_{basis}} C\phi_j(\mathbf{r}). \tag{3.24}$$

Where C is in general a complex number. How much the reconstruction of the generic wave-function ψ_i^σ is correct depends on the completeness of the basis set. Obviously a complete basis set is made by an infinite number of basis function that can not be used in practice, so the number of basis function N_{basis} is a compromise between the computational cost and the "fidelity" of the representation Eq. (3.24).

The introduction of a basis allow to transform the problem Eq. (3.17) in a matrix diagonalization problem at each of the self consistent step. The ingredients in this case are the matrix elements $\langle\phi_i|H_{KS}^\sigma|\phi_j\rangle$ of the operators entering Eq. (3.18) and the overlap integrals $\langle\phi_i|\phi_j\rangle$ between the basis function[7]. The result is a set of N_{basis}

---

[7]Indeed it is not necessary to use a set of orthogonal basis function as basis set, so the overlap

eigenvalues $\{\varepsilon_i\}$ and eigenvectors $\{|\psi_i\rangle\}$ such that:

$$|\psi_i^\sigma(\mathbf{r})\rangle = \sum_j c_j^\sigma |\phi_j(\mathbf{r})\rangle. \tag{3.25}$$

The eigenvectors $|\psi_i\rangle$ are the searched one-electron wave-functions needed to calculate the electron density $n(\mathbf{r})$ in Eq. (3.10).

As in the case of the Exchange and Correlation Flavor, it is not possible to define the best basis set, rather each different problem has its best basis set and it should be stressed that a wrong choice of the basis set can result in a non-converging SCF cycle. Among the many possible choices of basis set we mention two different types: plane waves, and localized orbitals (see [115], chapter 14,15).

Plane waves basis set are used in periodic calculations[8]. The plane waves are defined by the reciprocal lattice vectors $\{\mathbf{G}_j\}$ to expand the periodic part $u_j(\mathbf{r})$ of the Bloch function in Eq. (3.23). They are defined as:

$$\phi_{\mathbf{G}_j}(\mathbf{r}) = \frac{1}{\sqrt{V}} e^{i\mathbf{G}_j \cdot \mathbf{r}}. \tag{3.26}$$

The plane waves are normalized using the volume V of the solid, that is calculated multiplying the volume of the direct space unit cell by the number of k-points used in the BZ sampling. The number of plane waves included in the basis set is usually defined by a cut-off energy E_{cut}, so that only the plane waves that fulfill $\hbar^2(\mathbf{k}+\mathbf{G}_j)^2 < 2mE_{cut}$ (where $\mathbf{k}$ is the momentum of the Bloch function Eq. (3.23) and m is the electron mass) are included in the calculation. It should be noted that plane waves are not the best choice for all electron calculation, because a good representation of the very localized core orbital can be achieved with a very large number of plane waves that result in inefficiency in the calculation speed.

Another possible choice for the basis set is the localized orbital basis set. They are the natural choice in finite size calculations, even though they can be used in periodic calculation to expand $u_j(\mathbf{r})$. There are different possible choice for the actual shape of localized function, among the others we cite:

1. Slater type orbitals (STO) [127]: are analytical functions, whose shape mimic the eigen-functions of the Hydrogen atom. Being spherically symmetric, STOs are usually expressed as products of spherical Harmonics and radial functions, that decay like e^{-r}. STOs enter ab-initio calculations of simple diatomic molecules [128] and can be used both for all electron and pseudo-potential DFT codes.

2. Gaussian type orbitals (GTOs) [129]: Another possible choice for analytic functions is given by gaussian orbitals. Also in these case the function can be written as a spherical harmonic multiplied by a gaussian radial function centered on the atomic core. The gaussian shape of the radial function has the advantage of easing the integrations, speeding up the evaluation of matrix elements. They can be used both for all electron and for pseudopotential calculation.

---

integrals between different basis function can be nonzero.

[8]As previously stated, plane waves can be used for finite-size-like objects, like atoms and molecules, by means of the periodic super-cell method.

3. Numerical atomic orbitals (NAOs) [130]: It is also possible to expand the radial part of the basis function using numerical orbital. The numerical orbital, unlike gaussian and Slater orbital, have the advantage that they can be defined on a finite size support. They are centered on the atomic cores and have the advantage that their overlap is exactly zero for functions centered sufficiently far apart. They are usually defined approximating some analytic function or from a pseudopotential calculation for the isolated atom.

Finally, it is worth noticing that some techniques use mixed basis functions, like the Projector Augmented PlaneWaves method (PAW), with localized functions for the regions near the atomic cores and plane waves for the interstitial regions. An application is provided by the localized d and f orbitals in the LDA+U method.

3.4 TDDFT+RPA

It is well-known that DFT codes work with a 3D periodic geometry (which is not the case obviously of any graphene-related or beyond material), in our case the periodic structure is made of replicated planes in the out-of-plane direction. The mutual interaction between the replicas is known to play a significant role in many-electron features like excitation energies, the frequency-dependent electronic response, photo-absorption spectra, as well as exciton bands dispersion [131, 132].

In order to get rid of these artificial effects, here we introduce a mixed (direct-reciprocal) approach to treat graphene, silicene, germanene and graphene nanoribbons arrays as 2D materials. This approach [106, 19, 107, 20] is based on two-steps: (i) the electronic ground state of the systems under consideration, is first determined with full inclusion of the band structure and the interlayer interaction, thus, a Dyson-like equation is solved self-consistently in order to calculate the so-called density-response function of the many-electron system, and (ii) a 2D correction is subsequently applied, to eliminate the artificial interaction between the out-of-plane periodic replicas, i.e., an unwanted physical phenomenon.

3.4.1 Density-response function in 3D systems

As stated before the key outputs (see Fig. 3.1) of DFT calculations are the Kohn-Sham eigenvalues $\varepsilon_{\nu\mathbf{k}}$ and eigenvectors $|\nu\mathbf{k}\rangle$, which are the main ingredients to compute the density-response function of a 3D periodic and *non-interacting* many-electron system in reciprocal space. The latter is defined as follows [133, 134]

$$\chi^0_{\mathbf{GG'}}(\mathbf{q}, \omega) = \frac{2}{\Omega} \sum_{\mathbf{k}, \nu, \nu'} \frac{(f_{\nu\mathbf{k}} - f_{\nu'\mathbf{k}+\mathbf{q}}) \rho^{\mathbf{kq}}_{\nu\nu'}(\mathbf{G}) \, \rho^{\mathbf{kq}}_{\nu\nu'}(\mathbf{G'})^*}{\omega + \varepsilon_{\nu\mathbf{k}} - \varepsilon_{\nu'\mathbf{k}+\mathbf{q}} + \mathrm{i}\,\eta}, \tag{3.27}$$

where the matrix elements $\rho^{\mathbf{kq}}_{\nu\nu'}(\mathbf{G})$ has the form:

$$\rho^{\mathbf{kq}}_{\nu\nu'}(\mathbf{G}) = \langle \nu\mathbf{k}|e^{-\mathrm{i}(\mathbf{q}+\mathbf{G})\cdot\mathbf{r}}|\nu'\mathbf{k}+\mathbf{q}\rangle \tag{3.28}$$

and the Fermi-Dirac distribution $f_{\nu\mathbf{k}}$ is

$$f_{\nu\mathbf{k}} = \frac{1}{1 + e^C} \tag{3.29}$$

with $C = \varepsilon_{\nu\mathbf{k}} - u/kT$. T is the temperature and u the chemical potential (doping level).

In Eq. (3.27), the sums over band indices and wavevectors run within the first Brillouin zone over both occupied and unoccupied levels, whose population is established by the Eq.(3.29), and the factor of 2 accounting for the spin degeneracy and η is a positive infinitesimal broadening[9].

The exact *interacting* density-response function can be obtained in the framework of TDDFT, as follows [135]

$$\chi_{\mathbf{G}\mathbf{G}'} = \chi^0_{\mathbf{G}\mathbf{G}'} + \sum_{\mathbf{G}_1\mathbf{G}_2} \chi^0_{\mathbf{G}\mathbf{G}_1} v_{\mathbf{G}_1\mathbf{G}_2} \chi_{\mathbf{G}_2\mathbf{G}'}, \tag{3.30}$$

where $v_{\mathbf{G}_1\mathbf{G}_2}$ represent the Fourier coefficients of an effective electron-electron interaction.

In the framework of linear-response theory, the inelastic scattering cross section corresponding to a process in which (after the scattering of external electrons or photons) an electronic excitation of wavevector $\mathbf{q}+\mathbf{G}$ and energy ω is created at the 3D periodic system is proportional to the imaginary part of one diagonal element of the so-called inverse dielectric matrix:

$$(\epsilon^{-1})_{\mathbf{G}\mathbf{G}'} = \delta_{\mathbf{G}\mathbf{G}'} + \sum_{\mathbf{G}_1} v^0_{\mathbf{G}\mathbf{G}_1} \chi_{\mathbf{G}_1\mathbf{G}'}, \tag{3.31}$$

where $v^0_{\mathbf{G}\mathbf{G}_1}$ represent the Fourier coefficients of the bare Coulomb interaction denoted as:

$$v^0_{\mathbf{G}\mathbf{G}_1} = \frac{4\pi\delta_{\mathbf{G}\mathbf{G}_1}}{|\mathbf{q} + \mathbf{G}|^2} \tag{3.32}$$

In the RPA, the effective electron-electron interaction is taken to coincide with its bare Coulomb counterpart, i.e., $v_{\mathbf{G}_1\mathbf{G}_2} = v^0_{\mathbf{G}_1\mathbf{G}_2}$ and, therefore:

$$\epsilon_{\mathbf{G}\mathbf{G}'} = \delta_{\mathbf{G}\mathbf{G}'} - \sum_{\mathbf{G}_1} v^0_{\mathbf{G}\mathbf{G}_1} \chi^0_{\mathbf{G}_1\mathbf{G}'}. \tag{3.33}$$

The so-called crystal local-field effects are included by taking the full matrix $\epsilon_{\mathbf{G}\mathbf{G}'}$ in the process of obtaining the diagonal part of the inverse dielectric matrix $(\epsilon^{-1})_{\mathbf{G}\mathbf{G}'}$. We

---

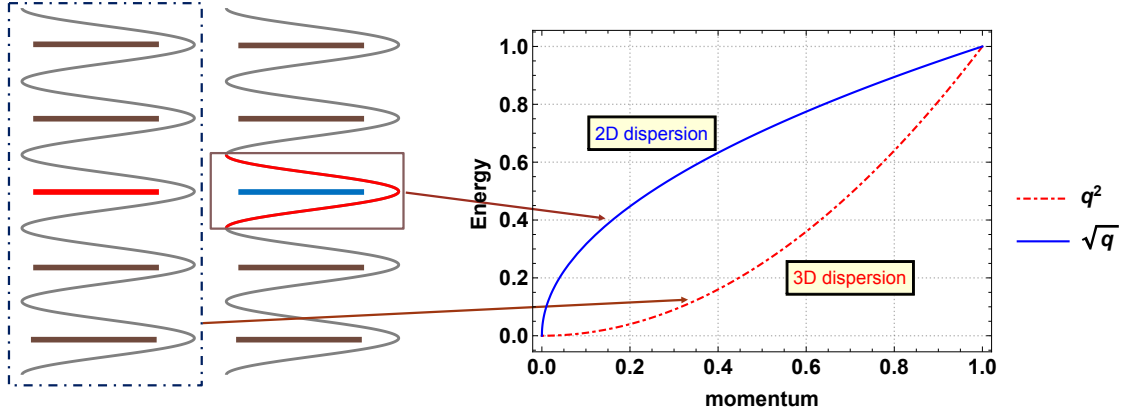[9]In this thesis well-converged results have been obtained for $\eta = 0.02$ eV

Figure 3.3: Schematic representation of a 2D material treated with the 3D and 2D approaches.

have verified that with the use of $\mathbf{G}$-vectors[10] of the form $\{0, 0, G_z\}$, sorted in length order from smallest to largest, crystal local-field effects are properly taken into account for the momenta $\mathbf{q}$ and the energies ω under consideration.

Now, the collective excitations i.e., plasmons are dictated by the zeros in the real part of the so-called macroscopic dielectric function (permittivity) where the imaginary part is small or zero, *this is a plasmon condition to occur*:

$$\epsilon^M = \frac{1}{(\epsilon^{-1})_{\mathbf{00}}}. \tag{3.34}$$

Then, the so-called energy-loss function is related to the imaginary part of the inverse permittivity:

$$E_{\text{LOSS}}(\mathbf{q}, \omega) = -\text{Im}[\frac{1}{\epsilon^M(\mathbf{q}, \omega)}]. \tag{3.35}$$

The approach outlined above is accurate for purely 3D periodic systems where the typically plasmon dispersion is of the form q^2 (see Fig. 3.3), as it is seen in graphite, however, the plasmon dispersion in 2D materials expected is the form $\sqrt{q}$-like.

3.4.2   Density-density response function in 2D systems

To treat a 2D material, in our case graphene, silicene, germanene or graphenene nanoribbons arrays, it is necessary to consider the long-range behavior of the Coulomb interaction Eq. (3.32) along the out-of-plane direction. A reasonably large distance between the system replicas, such as the ~ 20 Å value, which we have used in this thesis, ensures a negligible overlap between the Kohn-Sham single-particle orbitals entering χ^0.

---

[10]51-$\mathbf{G}$-vectors for graphene, silicene and germanene and $\sim$120-$\mathbf{G}$-vectors for graphene nanoribbons arrays

Nonetheless, in the building up of the *interacting* density-response function χ (and, therefore, the energy-loss funcion E_{LOSS} [Eq.(3.35)]) the electron densities that are localized at each plane may still interact with one another through the long-range Coulomb interaction. Such an unwanted effect decreases too slowly with the increase of the separation between the repeated planes, so that a well-converged calculation of the inverse dielectric matrix becomes computationally unaffordable even for finite momenta.

In the long-wavelength limit ($\mathbf{q} \to 0$), the $\mathbf{G} = \mathbf{G'} = \mathbf{0}$ component of the Coulomb interaction diverges; hence, in this limit contributions to the *interacting* density-response function coming from the interaction between the electron densities that are localized in the repeated planes are not negligible, no matter how large their physical distance is. It turns out that in this long-wavelength limit the electronic response and the collective modes of a system composed of replicated 2D planes are *artificially* similar to those encountered in a truly 3D periodic system. A viable solution to this problem is to cut the unwanted contribution from the interaction between the replicas by using a mixed (direct-reciprocal) space representation [106, 19, 107, 20].

First of all, we separate the in-plane and out-of-plane components of the reciprocal lattice vector, which we represent as $\mathbf{G} = \{\mathbf{g}, G\}$. We then select excitation processes where the momentum transfer $\mathbf{q}$ lies within the plane of the slab (i.e., $\mathbf{q}\|\mathbf{k}$), and we look at the following Fourier transforms:

$$\bar{\chi}^0_{\mathbf{gg'}}(z, z') = \frac{1}{L_z} \sum_{G,G'} e^{iGz} \chi^0_{\mathbf{GG'}} e^{-iG'z'} \tag{3.36}$$

and

$$\bar{\chi}_{\mathbf{gg'}}(z, z') = \frac{1}{L_z} \sum_{G,G'} e^{iGz} \chi_{\mathbf{GG'}} e^{-iG'z'}, \tag{3.37}$$

where z represents the out-of-plane coordinate which we restrict to a finite region $[a, b]$ containing the unit-cell of the 3D system and excluding, therefore, the replicas. So, the systems's susceptibility can be expressed as a function of the in-plane wavevector and the out-of-plane coordinate, Eq. (3.30) becomes

$$\bar{\chi}_{\mathbf{gg'}}(z, z') = \bar{\chi}^0_{\mathbf{gg'}}(z, z') + (\bar{\chi}^0 \bar{v} \bar{\chi})_{\mathbf{gg'}}(z, z'), \tag{3.38}$$

or explicitly introducing Eq. (3.30) into Eq. (3.37), one finds:

$$\bar{\chi}_{\mathbf{gg'}}(z, z') = \bar{\chi}^0_{\mathbf{gg'}}(z, z') \tag{3.39}$$
$$+ \frac{1}{L_z} \sum_{G,G'} e^{iGz} \sum_{\mathbf{G_1 G_2}} \chi^0_{\mathbf{GG_1}} \, \kappa_{\mathbf{G_1 G_2}} \, \chi_{\mathbf{G_2 G'}} e^{-iG'z'},$$

where the interaction kernel

$$\kappa_{\mathbf{G_1 G_2}} = \int_a^b dz_1 \int_a^b dz_2 e^{-iG_1 z_1} \bar{v}_{\mathbf{g_1 g_2}}(z_1, z_2) e^{iG_2 z_2} \tag{3.40}$$

is simply:

$$\kappa_{\mathbf{G}_1\mathbf{G}_2} = \frac{2\pi\delta_{\mathbf{g}_1\mathbf{g}_2}f_{G_1G_2}}{|\mathbf{q}+\mathbf{g}_1|}. \tag{3.41}$$

and $\bar{v}_{\mathbf{g}_1\mathbf{g}_2}(z_1, z_2)$ is (in the RPA):

$$\bar{v}_{\mathbf{g}_1\mathbf{g}_2}(z_1, z_2) = \frac{2\pi}{|\mathbf{q}+\mathbf{g}_1|}e^{-|\mathbf{q}+\mathbf{g}_1||z_1-z_2|}\delta_{\mathbf{g}_1\mathbf{g}_2}. \tag{3.42}$$

A back Fourier transform of Eq. (3.39) with respect to the out-of-plane coordinates z, z' yields the Fourier coefficients $\bar{\chi}_{\mathbf{G}\mathbf{G}'}$, which have no spurious contribution from the interaction between the replicated planes. Such an operation restores the advantage of dealing with purely algebraic matrix operations and, at the same time, keeps unaltered the formal definitions of Eqs. (3.30)-(3.35), on which we simply add a *bar*-symbol to recall that the usual Coulomb coefficients $v^0_{\mathbf{G}\mathbf{G}'}$ need to be replaced by those of Eq. (3.40). [11]

For symmetry reasons and computational advantage, we choose $a = -L_z/2$ and $b = L_z/2$, in which case the matrix elements of Eq. (3.40) reduce to the simple form:

$$\kappa_{\mathbf{G}_1\mathbf{G}_2} = v^0_{\mathbf{G}_1\mathbf{G}_2} + \frac{4\pi\delta_{\mathbf{g}_1\mathbf{g}_2}e^{-iL_z\frac{G_1-G_2}{2}}}{L_z|\mathbf{q}+\mathbf{g}_1|} \tag{3.43}$$
$$\times \frac{1-e^{-L_z|\mathbf{q}+\mathbf{g}_1|}}{G_1^2+|\mathbf{q}+\mathbf{g}_1|^2}\frac{G_1G_2-|\mathbf{q}+\mathbf{g}_1|^2}{G_2^2+|\mathbf{q}+\mathbf{g}_1|^2}.$$

We note in passing that the choice $[a, b] \to [-\infty, \infty]$ would bring us back to the original quantities (with no *bar*-symbol), as defined in the previous paragraph.

---

[11]In the specific case of graphene, one can take $z = z' = 0$ in Eqs. (3.36)-(3.39) to obtain the in-plane RPA dielectric matrix defined in Eq. (1) of Ref. [44]. The two approaches are equivalent in the low q-limit, where crystal local field effects play a minor role, so that the loss function may be aproximated as $\bar{E}_{\mathrm{LOSS}} \approx 1/\epsilon_{\mathbf{00}}$ and only the interaction coefficient $\kappa_{\mathbf{00}}$ in Eq. (3.43) is relevant, tending to $2\pi L_z/q$ fo $q \to 0$.

Chapter 4

Plasmonic properties in honeycomb-like materials

Atomically thin materials, organized in hexagonal honeycomb-like geometry, have been through intense scrutiny due to their exceptional electronic and plasmonic properties [71, 57], the most intriguing of which is, perhaps, the strong coupling between their quantized charge-density fluctuations, i.e., plasmons, and light or other charged particles [136, 137]. Furthermore, the plasmon response of these two-dimensional systems, including graphene, graphene-related and beyond-graphene materials, may be tuned by external electric and magnetic fields and have the potential to be integrated in plasmonics for the design of high-speed, low-power consuming nano-devices [138] In this context, doped graphene has been recognized as a novel plasmonic material because of it can produce enhanced collective plasmon oscillations compared to those in noble metals. [139]. Nonetheless, the incompatibility of carbon-based materials with current silicon- and germaniun-based electronics, (semiconductor technology), makes the former unsuitable for immediate use, for which reason, other candidates among the group-IV elements, e.g., silicon and germanium in honeycomb lattice, i.e, silicene and germanene, have been explored, that, similarly to graphene, have, in their free-standing forms, linear dispersing valence (π) and conduction (π^*) bands, crossing at the so-called Dirac K (and K') points.

Here, the excitation and dispersion of surface plasmons in graphene, silicene and germanene take into account intrinsic (undoped) and extrinsic (doped/gated) conditions, are analyzed from the fundamental point of view, using time-dependent density functional theory in linear response regime (methodology in Chapter 3). Density functional calculations, being set up from first principles, do include anisotropic effects in the unique electronic structure of graphene, silicene and germanene that cause remarkable consequences at low-energies. The main signature of this anisotropy is the occurrence of two distinct plasmon modes over a frequency range of few meV to 1 eV, where most photonic devices may operate with large bandwidths and low losses.
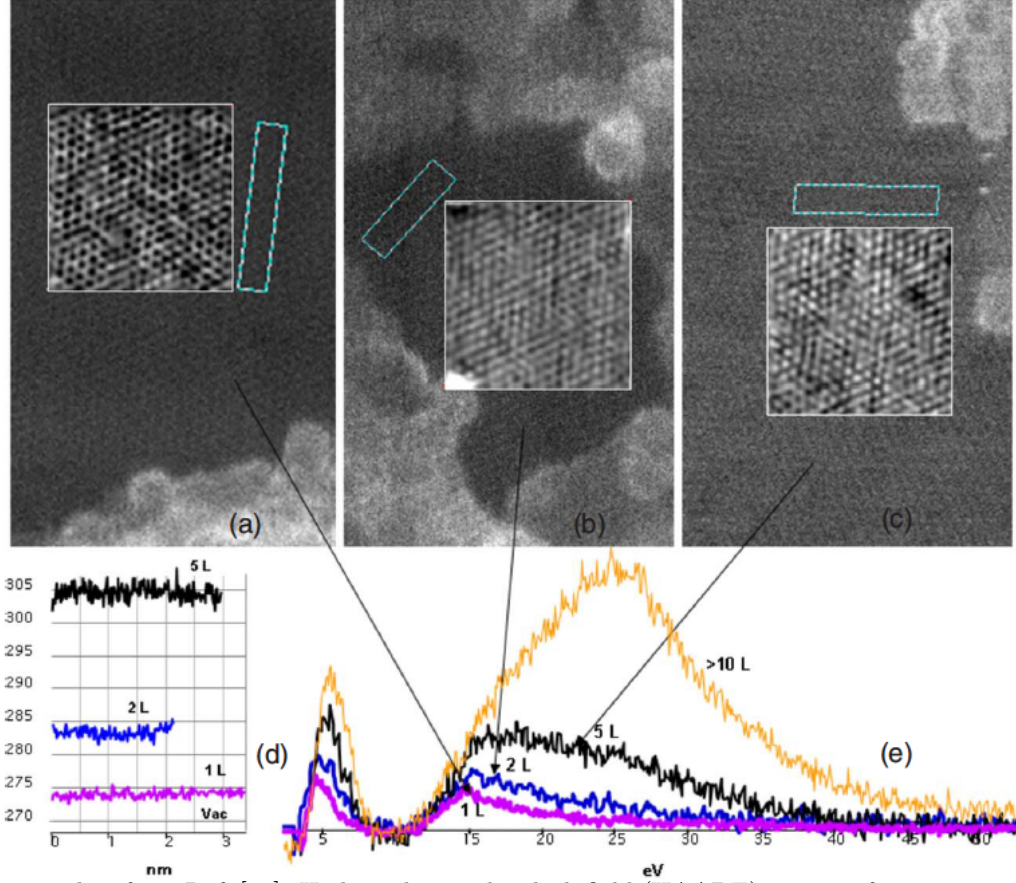
4.1   EELS measurements on graphene

Figure 4.1: Taken from Ref. [34]. High angle annular dark field (HAADF) images of one, two, and five layers of graphene. (d) Intensity traces of the rectangular cyan-framed boxes in (a)-(c); these traces show step-wise increase of the HAADF intensity corresponding to the layer number. (e) Electron energy loss (EEL) spectra of one, two, five and several layers of graphene showing the π and the $\sigma + \pi$ plasmons.

Electron-energy-loss spectroscopy (EELS) is a well-consolidated technique to study the collective properties of surfaces. Indeed, EELS measurements in conjunction with *ab initio* calculations of the loss function, have demonstrated the existence of two in-plane surface plasmon modes in free-standing graphene, so-called π and $\sigma + \pi$ plasmons analogous to the well-known bulk modes in graphite, detected at 7 and 26 eV, respectively [34].

In Fig. 4.1, high angle annular dark field (HAADF) imaging [Fig. 4.1(a)-(b)] and highly spatially resolved EELS [Fig. 4.1(e)] displays the π and $\sigma + \pi$ modes, in one, two, and five layers of graphene [34]. The π plasmon is due to a π to π^* transition and the $\sigma + \pi$ plasmon corresponds to the $\pi - \sigma^*$ and $\sigma - \pi^*$ transitions (as we will see in next subsections at analyzing the band structure of graphene). Interesting enough, the π plasmon is more intense than the $\sigma + \pi$ plasmon in graphene, with the relative intensity of the two peaks changing, in favor of the σ mode, with increasing the number of graphene layers. The electron-energy loss spectrum [Fig.4.1(e)] shows that the π

mode at 7 eV and the $\sigma + \pi$ at 26 eV detected in graphite, have red-shifted to 4.7 eV and 14.6 eV, respectively, in graphene.

However, considering a specific number of layers, these plasmon structures are not controllable from the point of view of applications. Otherwise, with the increase of graphene layers (< 10 layers), the plasmon structures are blue-shifted. Furthermore, these structures for more than 10 layers strongly resembles those of the graphite modes. Thus, the EEL measurements alternatively can be used as an indicators for the presence of graphene with a specific number of layers [34].

4.2 Computational Details

Before clarifying the detailed features of the high-energy plasmon modes in graphene and beyond, we provide the input parameters to compute the ground-state electron-density as well as the Kohn-Sham energies and orbital necessary to carrier out the TDDFT+RPA calculations (described in Chapter 3) on graphene, silicene and germanene with free-standing (monolayer) conformations.

All calculations have been performed at T= 300K. The equilibrium electronic properties of honeycomb-like systems were determined by density functional theory (DFT) [140, 141] in the local density approximation (LDA) [142], with the Kohn-Sham (KS) electron wave functions expanded in the plane-wave (PW) basis. The latter is represented by the space functions:

$$\text{PW}_{\mathbf{k}+\mathbf{G}}(\mathbf{r}) = \Omega_0^{-1/2} e^{i(\mathbf{k}+\mathbf{G})\cdot\mathbf{r}}, \tag{4.1}$$

where $\mathbf{k}$ is a wave vector in the first Brillouin zone (BZ), $\mathbf{G}$ a reciprocal-lattice vector, and Ω_0 the unit-cell volume associated to the real-space lattice [Fig. 4.2(a) and 4.2(b)]. The number of PWs was limited by the energy cut off $|\mathbf{k}+\mathbf{G}|/2 \le 25$ Hartrees. Norm conserving pseudopotentials of the Troullier-Martins type [143] were adopted to eliminate the core electrons. The three-dimensional periodicity inherent our PW-DFT approach was generated by replicating the planes with a minimum separation L of 20 Å.

Geometry optimization and ground state calculations were carried out on the irreducible part of the first BZ [ΓKM triangle in Fig. 4.2(b)], using a Γ-centered and unshifted Monkhorst-Pack (MP) [124] grid of $N = 180{\times}180{\times}1$ $\mathbf{k}$ points. The optimized lattice constant a and buckling parameter Δ are reported in top of Fig. 4.2. As for the LDA electronic structure, the KS energies $\varepsilon_{\nu\mathbf{k}}$ and wave functions

$$\langle \mathbf{r}|\nu\mathbf{k}\rangle = N^{-1/2} \sum_{\mathbf{G}} c_{\nu\mathbf{k}+\mathbf{G}} \text{PW}_{\mathbf{k}+\mathbf{G}}(\mathbf{r}), \tag{4.2}$$

were computed for $\nu \le 60$ bands, with the $\mathbf{G}$ sum being limited by the energy cut off condition set forth above to include ~ 5000 coefficients $c_{\nu\mathbf{k}+\mathbf{G}}$ per wave function. The ground-state electron density for the optimized structures, was used-in a non self consistent run-to improve the resolution on the KS eigensystem $\{|\nu\mathbf{k}\rangle, \varepsilon_{\nu\mathbf{k}}\}$. The latter was recalculated on an MP mesh of $N = 360 \times 360 \times 1$ $\mathbf{k}$ points, including

up to 60 bands. This result was plugged in the TDDFT+RPA machinery, described in Chapter 3 [20, 97], to have an accurate representation of the electronic excitations and energy loss properties in the eV scale. For lower energies we use an equilibrium electronic structure represented on an MP grid of $N = 720 \times 720 \times 1$ **k** points and 12 bands.

4.3 Electronic properties of honeycomb-like structures

The structural analysis of graphene, silicene and germane, was performed for each configuration using PW-LDA exchange–correlation method [142]. The lattice parameters corresponding to a minimum in the ground-state energy for planar configurations is obtained was selected. To investigate the buckling parameter in all structures one of the atom was shifted out of plane initially by 0.2 Å and the optimization routine was run untill minimum force and lattice stress condition were met.

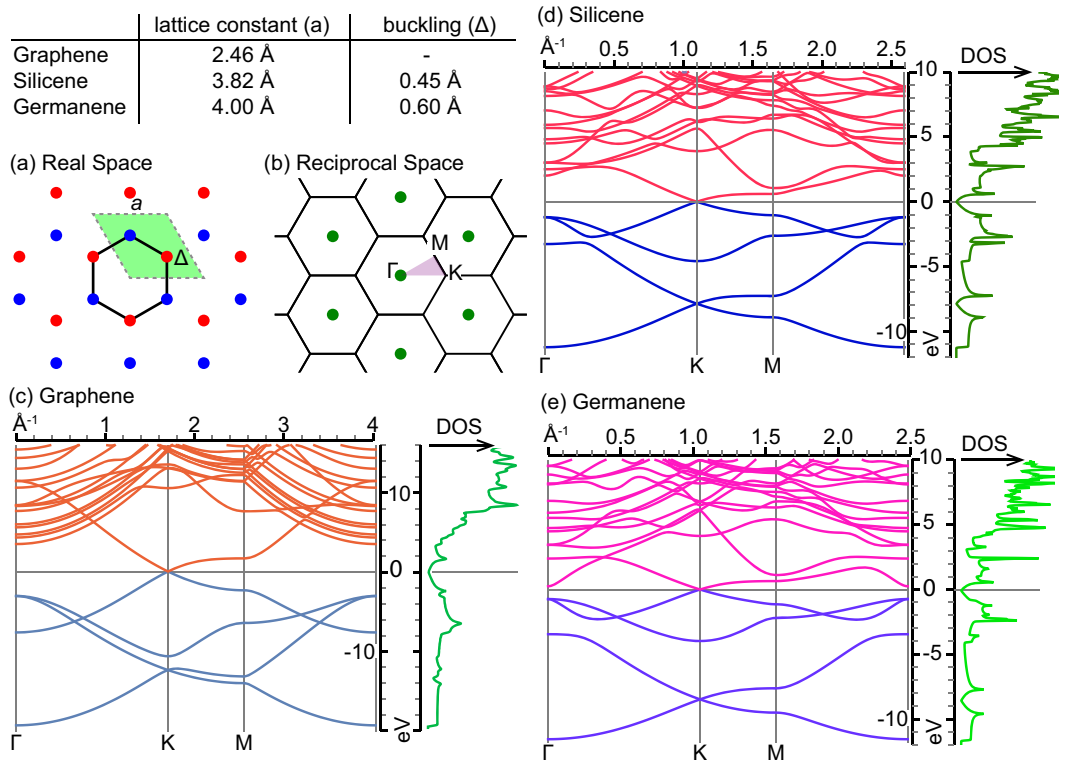|	lattice constant (a)	buckling (Δ)
Graphene	2.46 Å	-
Silicene	3.82 Å	0.45 Å
Germanene	4.00 Å	0.60 Å

Figure 4.2: Structural and electronic properties of graphene, silicene and germanene: (a) direct lattice, unit cell (green rhomboid), lattice constant a (Å), and buckling parameter Δ (Å); (b) reciprocal lattice, first BZ, irreducible BZ (purple shaded triangle), and high-symmetry points Γ, K, M; (c)-(d) band structure along ΓKMΓ and density of states (DOS), with the Fermi level set to zero energy of graphene, silicene and germane, respectively.

The optimized lattice constant (a) and buckling parameter (Δ) of all structures are reported in Fig. 4.2 (Top left). For a comparative understanding the band structures of graphene, silicene and germane are shown in Fig. 4.2(c)-(e).

We see that these honeycomb-like structures behave as quasi-metals having zero band gap with linear energy dispersion and vanishing DOS at the K-point. Then, at low energies around the Fermi level (<0.8 eV) the electrons in these structures behave like massless Dirac-fermions [54]. We have corroborated previous results confirming that the Fermi velocity (V_F) in graphene and silicene is less than half of the value reported for graphene [44]. Since graphene is sp^2 hybridized, the coupling between the nearest-neighbor atoms (σ-bonds) is very strong and π electrons can easily tunnel from one atom to another. This explains the larger velocities of electrons in germane [144, 44] compared to silicene and germane. On the other hand, silicene and germane prefer a mixed sp^3-sp^2 hybridization due to their low-buckled structural conformations ($\Delta = 0.45$ Å and $\Delta = 0.60$ Å, respectively), say, the sp^2 hybridized orbitals get slightly dehybridized into sp^3-like orbital, which causes weakening of π bonds leading to buckled structure of silicene and germane.

Looking at DOS as function of the band energies [Fig.4.2], we notice in all structures, two peaks closest to Fermi energy (E_F), which correspond to the π and π^* flat band dispersions at the M point. Other two peculiar and well-defined DOS-peak structures (absent in graphene) appear at 3-4 eV above and below E_F that are direct consequence of the mixed sp^3-sp^2 hybridization and buckled conformation of silicene and germane. These characteristics (not found in graphene) play an important role in the plasmonic properties of silicene and germane at probing energies larger than 1.5 eV [145], as we will see in the following.
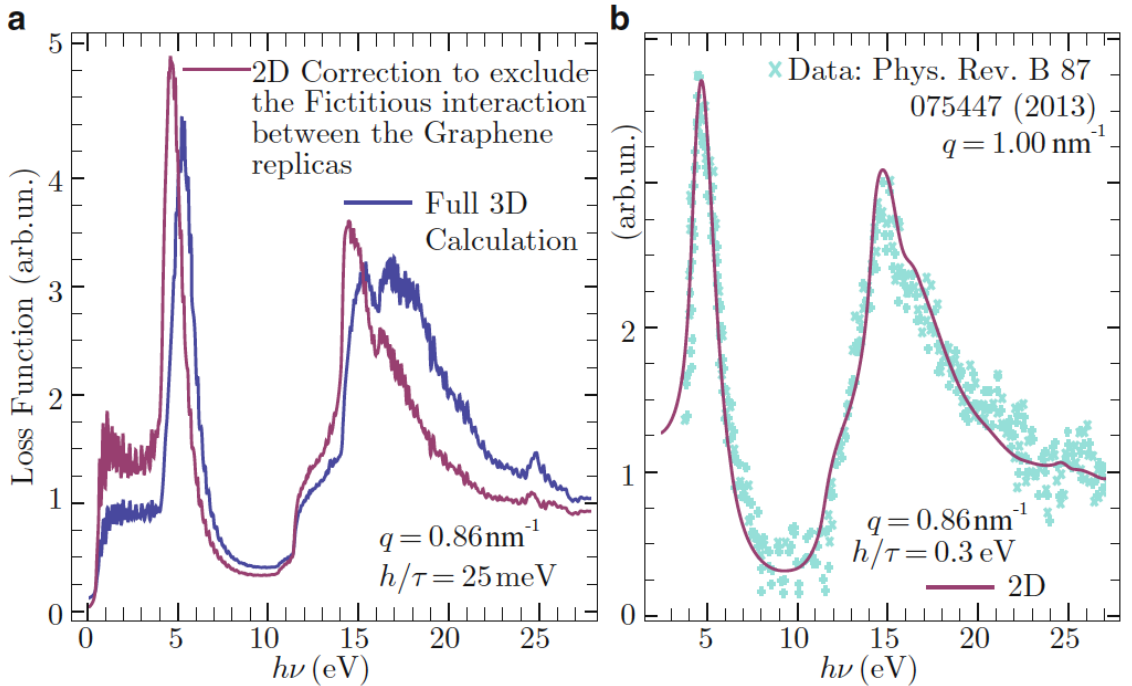

Figure 4.3: Taken from Ref. [146]. (a) Energy loss function of graphene on the eV scale computed with the methodology described in Chapter 3, with the bare 3D Coulomb potential and using the corrected 2D potential. An incident momentum of 0.86 nm^{-1} along the ΓK direction of the 1st BZ and a relaxation time of ~ 26.33 fs are used; (b) Two-dimensional loss function of panel (a), with a relaxation time of ~ 2.20 fs, and the EELS measure taken from Ref. [34, 19].

4.4 High energy plasmons: intrinsic conditions

To test the validity of our TDDFT+RPA methodology described in Chapter 3, the theoretical energy loss (EL) function of graphene is applied to the experimental loss spectrum of Ref. [34], including both the bare 3D Coulomb potential and the corrected 2D potential [19]. It turns out that the corrected loss is in amazingly close (energy and structure) agreement with the data, acquired from a suspended single layer graphene film on the eV scale [146, 19].
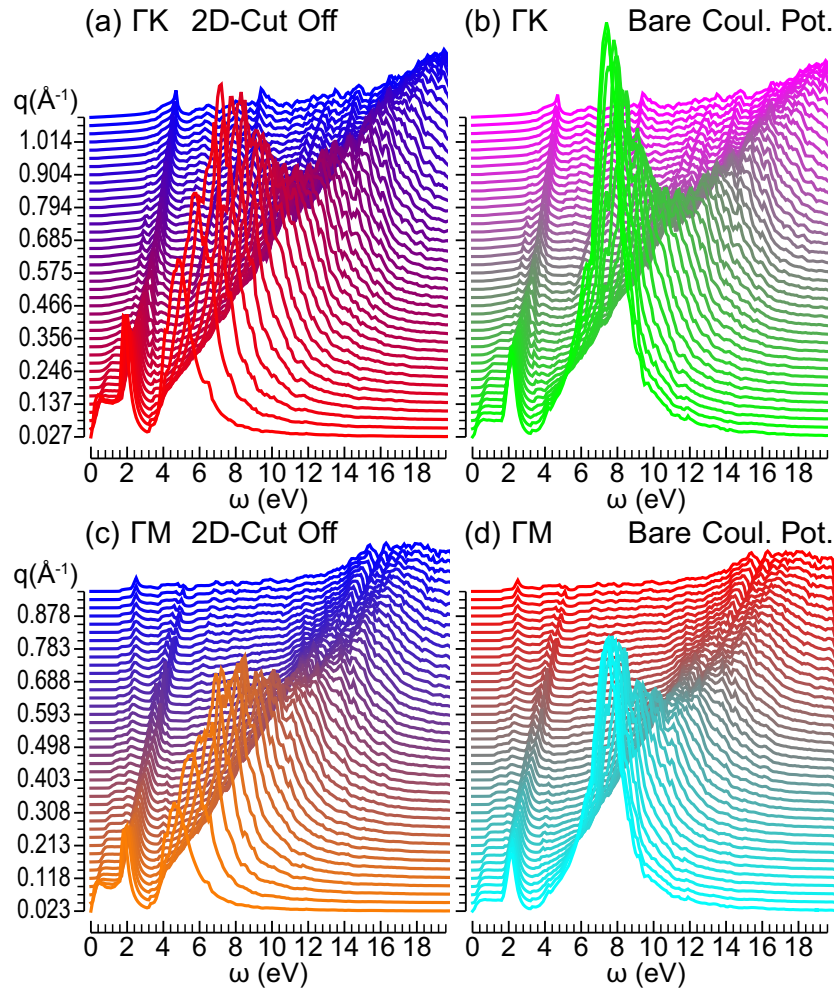

Figure 4.4: Taken from Ref. [145]. Energy-loss (EL) function of silicene, obtained with the TDDFT+RPA method described in Chapter 3, using the 2D corrected potential (cut off potential) [(a),(c)] and the bare 3D Coulomb potential [(b),(d)]. The loss curves (shifted vertically for clarity), are plotted vs $\omega < 20$ eV for sampled $\mathbf{q}$ values (in Å^{-1}) along ΓK [(a),(b)] and ΓM [(c),(d)].

Similarly, we focus on the long wavelength limit ($q \rightarrow 0$) and low frequency range (0-20 eV) of the plasmon spectra of silicene, and consider some previous theoretical results for comparison [147, 148]. Mohan and coworkers [147] have reported two plasmon features, with the π plasmon lying at 2.16 eV and the $\sigma + \pi$ plasmon being peaked at 7.6 eV. The same peaks have been predicted to be around 2 eV and 9 eV, respectively, by Das *et al* [148]. To verify these results, we have solved the Dyson-like equation

for the full susceptibility with the bare 3D Coulomb potential coefficients of Eq. **??** (Chapter 3).

The resulting loss function presents a narrow π plasmon peak at 2 eV and a broad $\sigma + \pi$ plasmon peak at 7 eV along both ΓK and ΓM, at the lowest sampled q values [Fig. 4.4(b) and 4.4(d)]. On the other hand, with the two-dimensional cut off procedure described in Chapter 3 the very same two plasmons appear red-shifted [Fig. 4.4(a) and 4.4(c)], in agreement with the calculations by Matthes and coworkers [149, 150]. The disagreement between the two approaches is particularly strong at the lowest sampled **q** points. Additionally, the calculations of Fig. 4.4 also demonstrate that applying a two-dimensional cut off on the Coulomb potential becomes unnecessary for values of the momentum transfer larger than 0.2 Å^{-1}, which is not surprising because the larger q-components of the Coulomb potential do not contribute to coupling of the repeated slab [145].

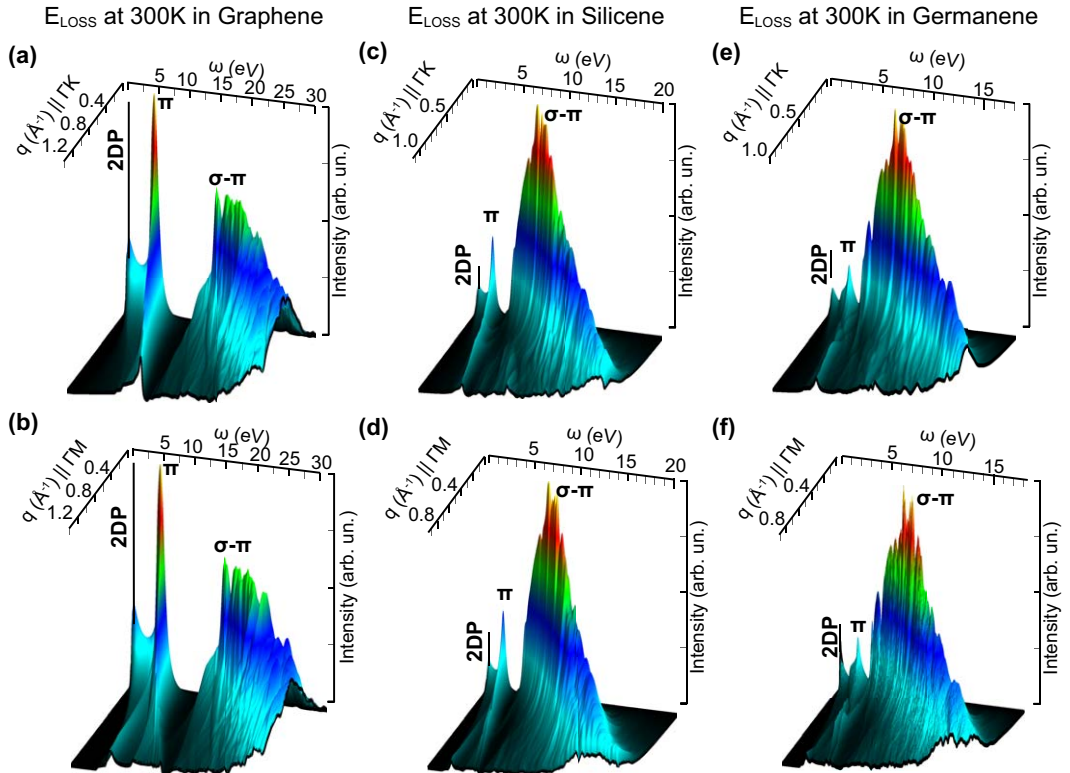## 4.4.1 Comparison of high energy plasmons on graphene, silicene and germane

Figure 4.5: EL function of intrinsic (undoped) graphene [(a),(b)], silicene [(c),(d)] and germane [(e),(f)] vs ω (in eV) for a momentum **q** in Å^{-1} along the ΓK and ΓM paths. The EL calculations are performed at T= 300K. The two-dimensional plasmon (2DP) is activated by temperature.

We have seen that the 2D corrected TDDFT+RPA approach (described in Chapter 3) seems to provide a solid ground for an accurate evaluation of plasmon modes in honeycomb-like materials. With this idea, we offer a comparison of the plasmon

response and plasmon dispersions in graphene, silicene, germane [Fig. 4.5] considering both intrinsic (undoped) and extrinsic (doped/gated) conditions at high- and low-energies, respectively.

First we focus in high-energy spectrum along ΓK and ΓM paths. A direct comparison of Figs. 4.5(a),(b) shows that the EL spectrum of graphene is characterized by two interband plasmon dispersion at energies above 4 eV, these are the above mentioned π plasmon (narrow peak at ~ 4.5 eV) and $\sigma + \pi$ plasmon (broad peak at ~ 14.5 eV). Additionally, one intraband plasmon dispersion is observed at low energies and momentum, that corresponds to the conventional two-dimensional plasmon (2DP, discussed in detail below), which is activated by the partial population of the π^* band as effect of temperature (T= 300K) [97]. Similarly, silicene and germane are characterized by two interband plasmon dispersions at energies above 2 eV, analogous to the well-known π and $\sigma + \pi$ plasmons of graphene and graphite [97, 20, 34, 151], and one intraband plasmon that correspond a 2DP activated by temperature. Nevertheless, the reduced width of the π (π^*) and σ (σ^*) bands in silicene [Fig.4.1(d)] and germane [Fig.4.1(d)] and their peculiar DOS features respect to graphene [Fig.4.1(c)], cause a red-shift and a different relative weight of the intrinsic plasmon peaks [145, 152].
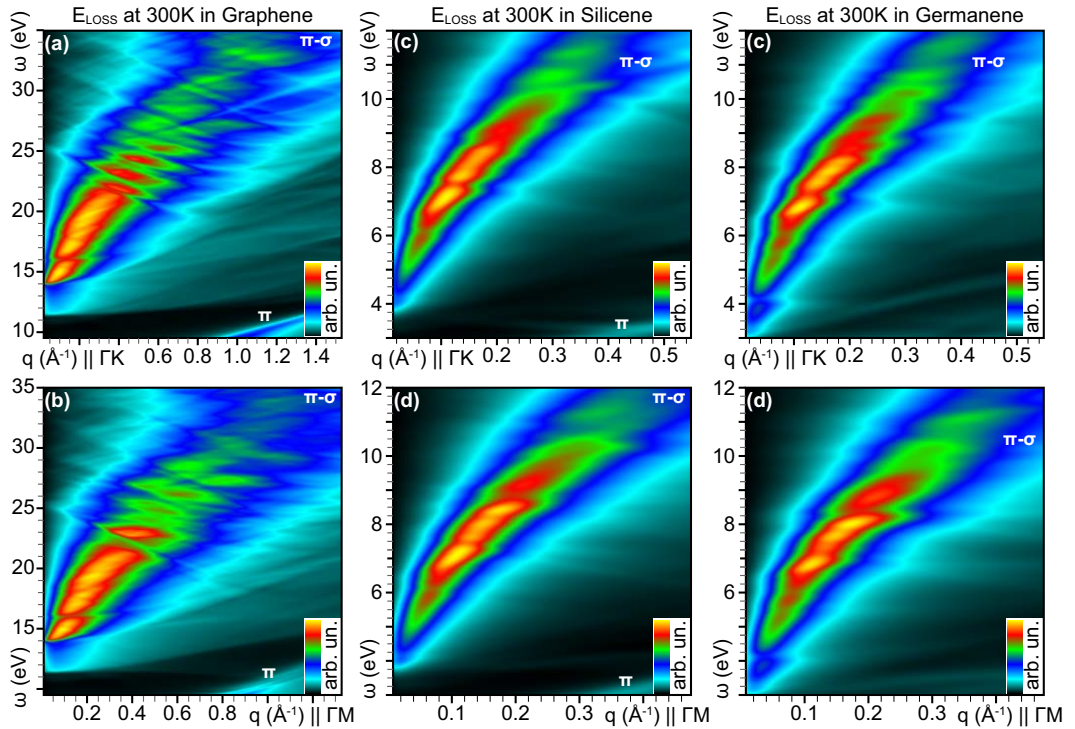

Figure 4.6: Density plots of $\sigma + \pi$ plasmon structure of undoped graphene [(a),(b)], silicene [(c),(d)] and germane [(e),(f)] vs ω (in eV) for a momentum **q** in Å^{-1} along the ΓK and ΓM paths. The calculations are performed at T= 300K.

To clarify the relative plasmon intensity and furthermore the plasmon dispersion feature (i.e., linear or quadratic), we represent the energy-loss spectrum as a density plot vs **q** and ω along the ΓK and ΓM paths for the $\sigma + \pi$ plasmon in Fig.4.6, and the π plasmon in Fig.4.7. Without considering the 2DP plasmon structure, the π and

$\sigma + \pi$ plasmon structures of graphene have similar peak intensities, whereas the $\sigma + \pi$ peak of silicene and germane is generally larger (by a factor of 3 at $q > 0.1$ Å^{-1}) than the π peak [145]. This fact can be ascribed to the weakening of the π bonds in silicene and germane due to the mixed sp^2-sp^3 hybridization discussed above.
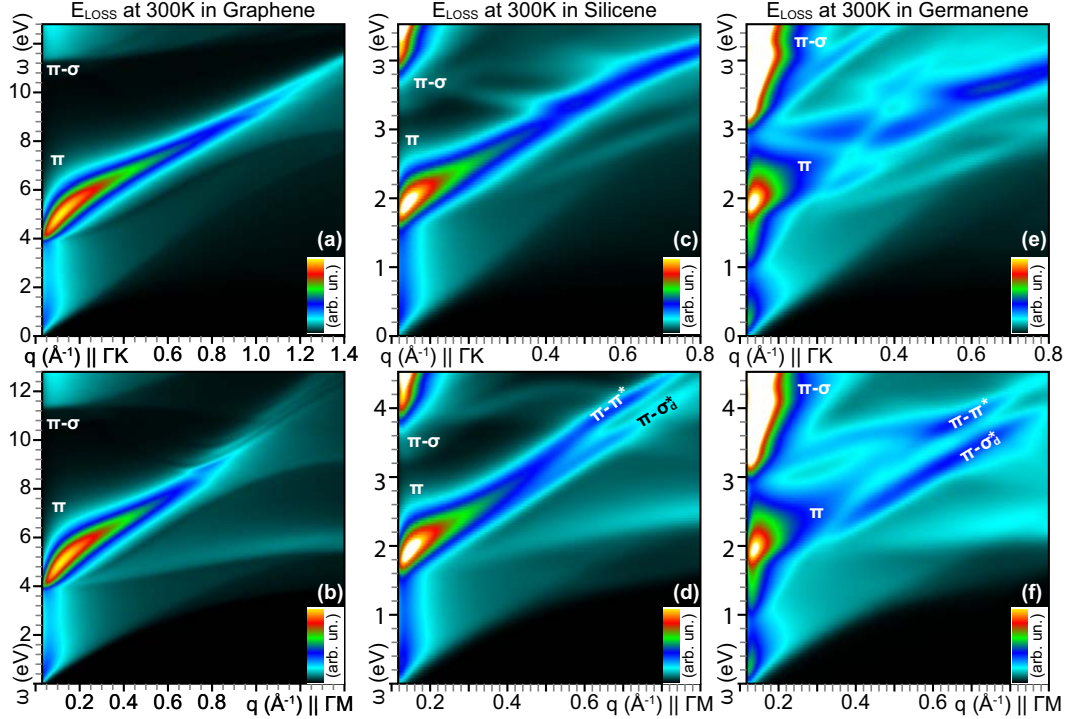

Figure 4.7: Density plot of π plasmon: E_{LOSS} of undoped graphene [(a),(b)], silicene [(c),(d)] and germane [(e),(f)] vs ω (in eV) for a momentum **q** in Å^{-1} along the ΓK and ΓM paths. The EL calculations are performed at T= 300K.

At small momentum ($q < 0.1$ Å^{-1}), the $\sigma + \pi$ plasmon in graphene, silicene and germane seems to be characterized by a quadratic (q^2) dispersion, apparently changes to a $\sqrt{q}$-like dispersion at higher energies [Fig.4.6].

As for the π mode, it shows a $\sqrt{q}$-like dispersion up to $q < 0.1$ Å^{-1}, and at $q > 0.1$ Å^{-1} a linear dispersion is observed [Fig.4.7]. Although, graphene is clearly characterized by a π plasmon with a linear dispersion at $q > 0.3$ Å^{-1}, silicene and germane, really, display a double (quasilinear) dispersion of the π plasmon at larger momentum ($q > 0.3$ Å^{-1}), which will be treated, in the next paragraphs, as a π-like plasmon.

This particular characteristic (π-like plasmon) in silicene, germane (and absent in graphene), is more clearly visible in the energy-momentum region $\omega \gtrsim 2.5$ eV and $q \gtrsim 0.3$ Å^{-1}, along the ΓM path [Fig. 4.7(d)-(f)]. In this region, the collective oscillation is associated to single-particle excitations [145] between high DOS points connecting the π and σ or π^* bands [Fig. 4.1(d),(e)]. Thus we can see how the mixed sp^3-sp^2 hybridization and low-buckled conformation of silicene ($\Delta = 0.45$ Å) and germane ($\Delta = 0.60$ Å) plays an important role in the π-like plasmon dispersion, which is obviously absent in graphene, due to its planar conformation ($\Delta = 0$).

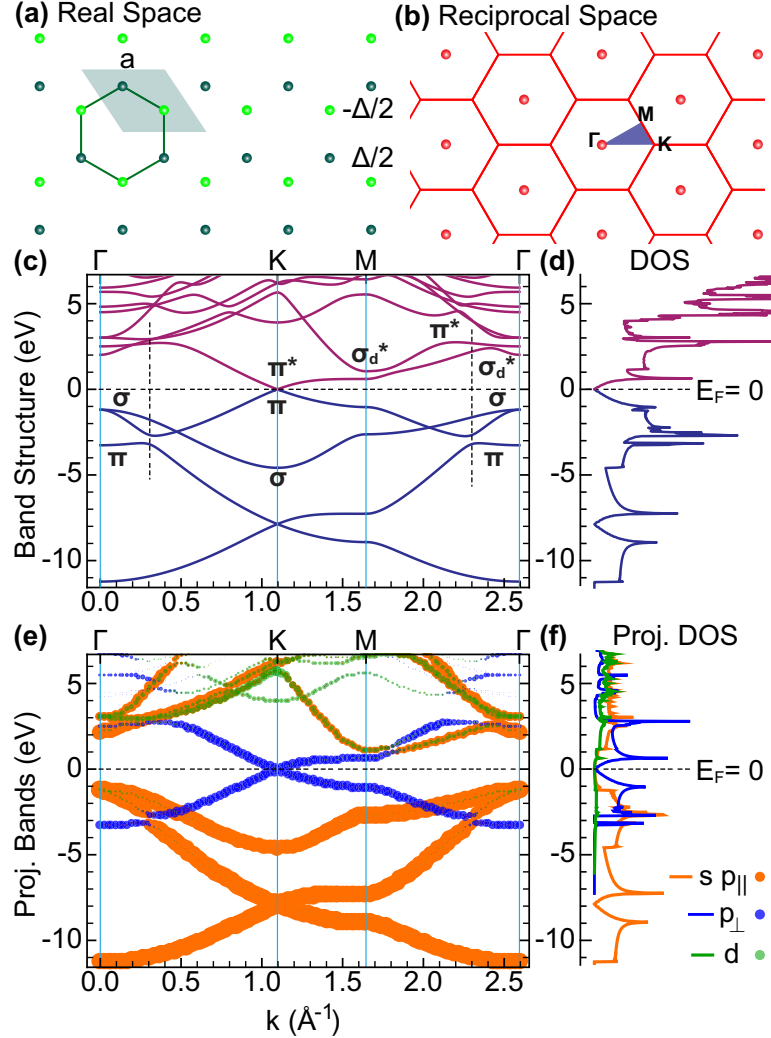### 4.4.2 Hybridized π-like plasmon in silicene

Figure 4.8: Taken from Ref. [145]. Geometric and ground state properties of silicene: (a) direct lattice, unit cell (green shaded rhomboid), lattice constant $a = 3.82$ Å, and buckling parameter $\Delta = 0.45$ Å; (b) reciprocal lattice, first BZ, irreducible BZ (blue shaded triangle), and high-symmetry points Γ, K, M; (c) band structure along $\Gamma K M \Gamma$, with the Fermi level set to zero energy; (d) DOS profile corresponding to the energy width of panel (c); (e) orbital projected band structure along $\Gamma K M \Gamma$ onto $s\,p_\parallel$, $p_\perp$ and d states of the unit-cell atoms (with $\parallel$ denoting the in-plane bonds and $\perp$ the out-of-plane bonds). The radius of each point is proportional to the weight of the corresponding atomic contribution; (f) orbital projected DOS corresponding to the orbital projected bands of panel (e).

Before entering the specific details of hybridization effects on the plasmon response of silicene, we move back to its band structure (Fig. 4.8). A simple visual perspective of the band energies [Fig. 4.8(c)] shows that silicene presents a Dirac cone structure at the K points around the Fermi energy E_F. A more detailed insight back to hybridization mechanisms [145] is offered by the orbital projected band structure and DOS of Fig. 4.8(e) and 4.8(f), respectively, where we have separated the contribution of s and $p_\parallel$ states, forming sp^2 like bonds, from $p_\perp$ states, involved in π bonds, and d states of the unit-cell Si atoms.
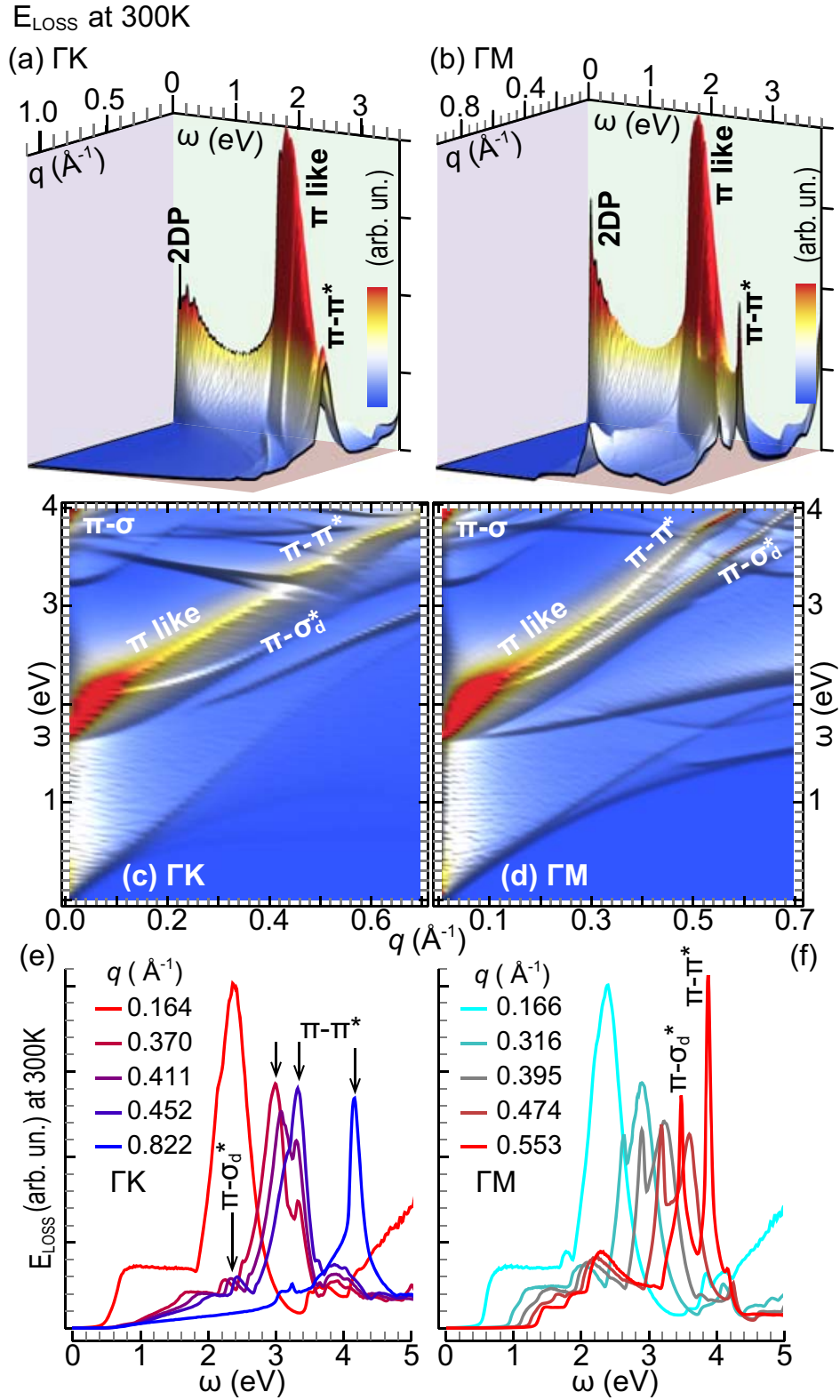
Figure 4.9: Taken from Ref. [145]. E_{LOSS} of undoped silicene vs $\omega < 5$ eV and momentum $q < 0.7$ Å^{-1} along ΓK [(a),(c),(e)] and ΓM [(b),(d),(f)].

The valence bands have well-defined σ and π characters, with sharp avoided-crossing features in correspondence of the DOS peaks at 2.5-3.5 eV, below E_F. The conduction states above the Dirac point are also of the π form, yielding an antibonding π^* band responsible for the DOS peak at 2.7 eV above E_F. Another conduction band denoted σ_d^* lies close to the π^* band and produces a DOS peak at 3 eV above E_F. It has a dominant σ-character contaminated by d states. Other conduction bands are strongly influenced by d, f, and higher principal quantum numbers, as it can be deduced by comparing the full DOS and its projected $s\,p_\parallel$, $p_\perp$ and d components at energies larger than ~ 3 eV above E_F. These characteristics (not found in graphene) play an important role in the plasmonic properties of silicene at probing energies larger than 1.5 eV, as we will see below.

A more detailed view on the π-like plasmon of silicene is offered by Fig. 4.9, where we see how the very close (or overlapping) energy levels in the π^* and σ_d^* bands [Fig. 4.8(c)] generate distinct plasmon features at high-DOS points [Fig. 4.8(d)]. For small incident momenta around the M point ($q < 0.1$ Å^{-1}) and energies below 2.5 eV, the large π^* DOS peak hides the σ_d^* contribution [Fig. 4.8(e) and 4.8(f)], and a single plasmon character dominates along both ΓK and ΓM. As q increases above ~ 0.3 Å^{-1} and ω gets larger than 3 eV, the σ_d^* component increases becoming of the same order as the π^* component [Fig. 4.8(d) and 4.8(f)]. This increase is associated to a larger splitting between the antibonding bands, which leads to a well-resolved two-peak structure in the energy-loss spectra. The latter presents markedly distinct features along ΓK and ΓM, being a signature of the deeply anisotropic character of the dielectric response of the system.

In either cases, the π-like plasmon is indeed a hybridized plasmon where the role of π-π^* and π-σ^* components, i.e., the relative spectral weight of the associated SP processes, is modulated by the excited electronic structure. In addition, slight changes in the lattice constant cause some distortions of the π-like plasmon peaks without altering the peak ratio of the π-π^* and π-σ^* parts (as we will see below). Besides the π-like and π-σ plasmons (discussed above), Fig. 4.9(a),(b) also shows a non-negligible intraband plasmon, peaked at energies below 0.5 eV, which is generated by a conduction electron concentration n^* of 1.06×10^{12} cm^{-2} at room temperature. This value is much larger (roughly by a factor of 10) than the one found in graphene, because of the smaller Fermi-velocity values that characterize silicene and corresponds to a lower slope in the vanishing DOS at the K-points [145]. Hence, intraband plasmons are also possible in the intrinsic limit when finite temperature is considered.

4.5 Low energy plasmons: extrinsic conditions

Given the similarities of silicene and germane (low-buckled conformation and mixed $sp^3 - sp^3$ hybridization), in this section we explore only the extrinsic plasmon response of silicene, and compare it to the extrinsic plasmon response of graphene (planar conformation and sp^2 hibridization).

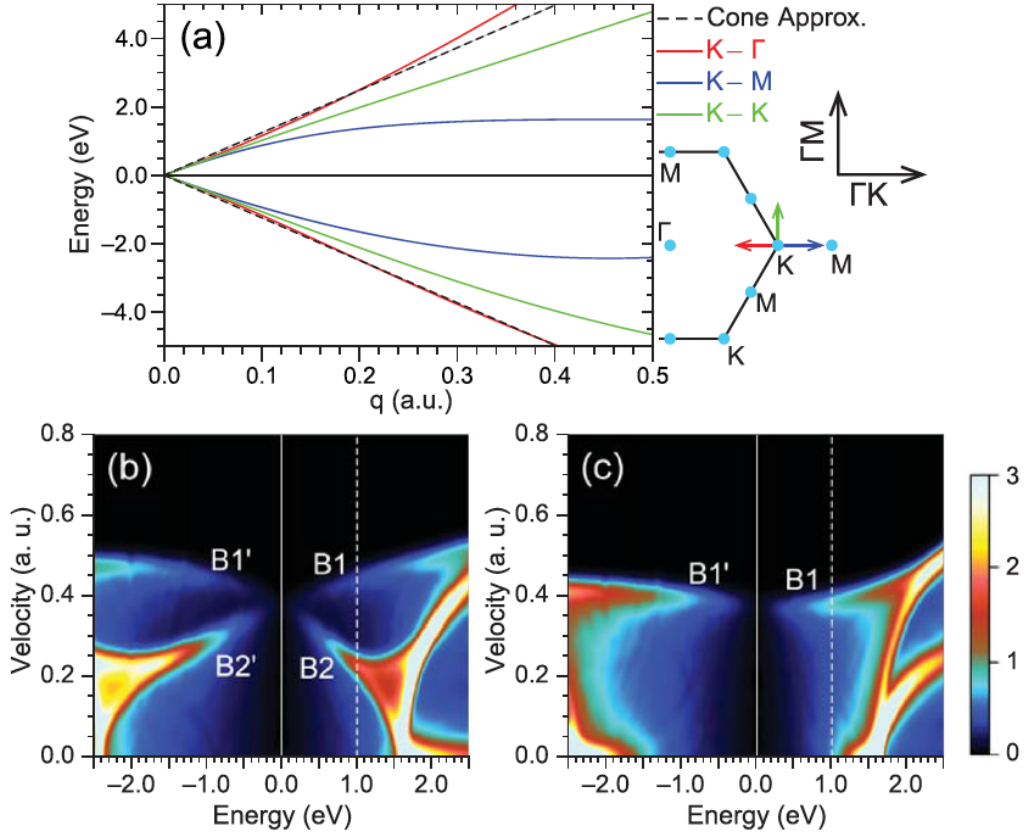## 4.5.1 Partial density of states in graphene and silicene

Figure 4.10: Taken from Ref. [44]. Graphene LDA band structure in the vicinity of the K point, as obtained along the three high-symmetry paths: the KΓ and KM branches (red and blue lines, respectively) in the ΓK direction, and the KK branch (green line) in the ΓM direction; the Dirac-cone approximation is represented by a black dashed line. Partial density of states along (b) ΓK and (c) ΓM vs the single-particle energy E and the group velocity. The solid and dashed vertical lines represent the Fermi level of intrinsic graphene and extrinsic graphene (with $\Delta E = 1$ eV), respectively.

Here, we provide a short insight into the anisotropic band structure of graphene (the failure of the Dirac cone approximation), which has been revealed by DFT computations [44, 146] and shown in Fig. 4.10(a).

In particular, we look at the partial density of states, for the π valence and the π^* conduction bands alone, as a function of the single-particle energy E and the group velocity[1] [Fig. 4.10(b),(c)]. We observe an unique anisotropic behavior in graphene. In fact, along the ΓM direction [Fig. 4.10(c)] the density of states is peaked around one single Fermi velocity $V_F \sim 10^6$ ms^{-1}, say, a peak B1 above the Dirac point and peak B1' below. On the other hand, the partial DOS along the ΓK direction [Fig. 4.10(b)] is peaked at two distinct velocities, say, peaks B1 and B2 above the Dirac point, and B1' and B2' below within the very same band.

---

[1] The group velocity for each band n as $v_n = \nabla_{\mathbf{k}} E_n(\mathbf{k})$, where $E_n(\mathbf{k})$ represents the energy dispersion of the nth band. The partial density of states is then readily calculated by 'counting' the number of states with a given energy E and velocity v_i in the i-direction. By integrating over v_i, the conventional density of state is obtained as a function of E.

This anisotropy allows the coexistence of carriers moving with two distinct Fermi velocities along the ΓK path, which explain the existence of two type of collective excitations, called 2DP and acoustic plasmon (AP). The same feature is expected in any honeycomb-like material, like silicene and germane. Indeed, we have performed the same analysis in silicene [152, 145], whose average Fermi velocity value $V_F = 0.54 \times 10^{-6}$ m/s (extracted from the band data) is roughly 65% of that derived from local density calculations in graphene [44], and reflects a relatively reduced mobility of the massless Dirac fermions of silicene. A detailed inspection of the partial DOS
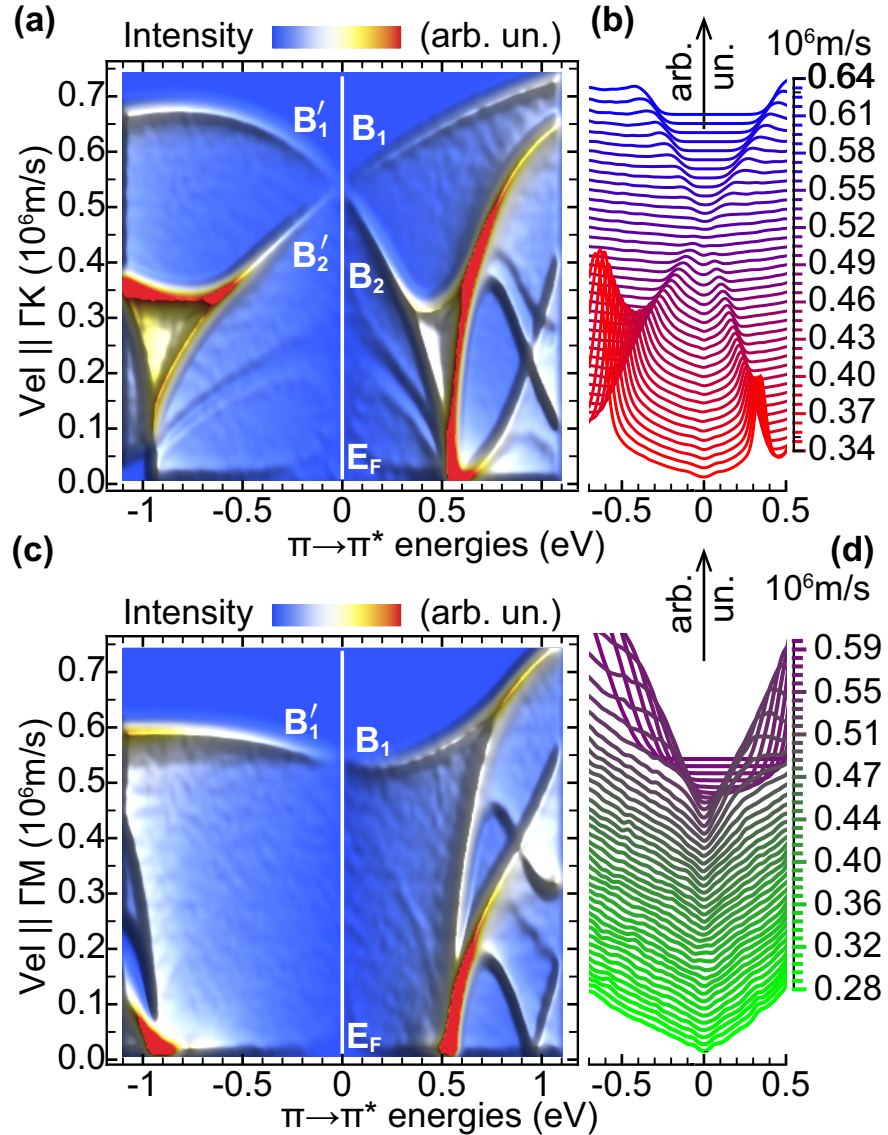

Figure 4.11: Taken from Refs. [145]. Partial DOS vs the one-electron energy of the π and π^* bands and group velocity along ΓK [(a),(b)] and ΓM [(c),(d)]; (b) and (d) provide a complementary view of (a) and (c), respectively, with the partial DOS curves being reported for fixed group velocity values and shifted vertically for clarity.

as function of the π-π^* energies and group velocities parallel to ΓK [Figs. 4.11(a) and 4.11(b)] and ΓM [Fig. 4.11(c) and 4.11(d)], allow us to see that along ΓK, the DOS

is peaked at two distinct Fermi-velocity values, corresponding to the B_1', B_2' branches below E_F and the B_1, B_2 branches above E_F in Fig. 4.11(a). Otherwise, along ΓM, the DOS is peaked around one single Fermi velocity value, associated to the B_1' branch below E_F and B_1 branch above E_F in Fig. 4.11(b). Like in graphene, this anisotropic behavior stands outside the Dirac cone approximation[2]), and furthermore two extrinsic plasmon responses along ΓK are expected also in silicene or germane.

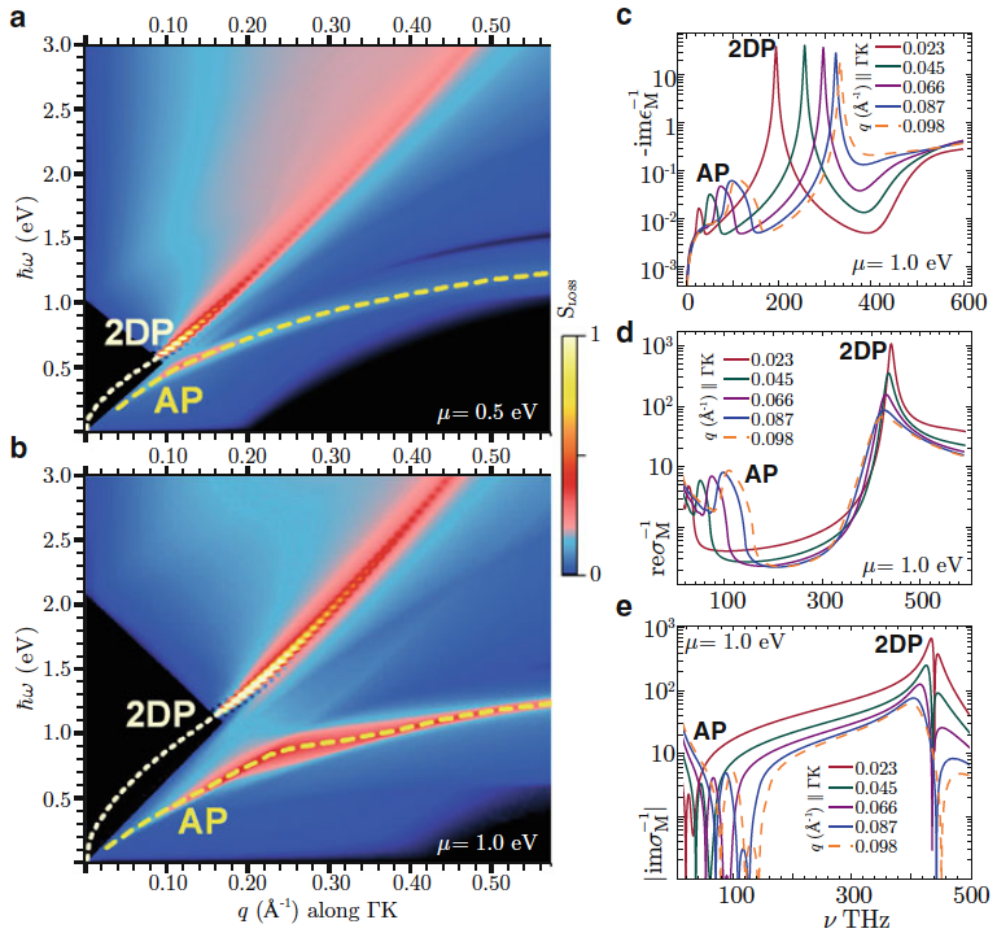### 4.5.2   2D plasmon and acoustic mode in graphene and silicene

Figure 4.12: Taken from Refs. [44, 146]. E_{LOSS} for extrinsic graphene vs ω and **q** along ΓK for Fermi shift i.e., $\Delta E_F = 0.5$ eV (a) and $\Delta E_F = 1.0$ eV (b); E_{LOSS} (c) and average resistivity (d),(e) vs ν at fixed $\Delta E_F = 1.0$ eV and $q = 0.023 - 0.098$ Å^{-1}.

In Fig. 4.12(a),(b); two collective excitations (plasmons) [44, 146] are clearly visible that are strictly absent in intrinsic graphene at T= 0K [97]. One of them is the conventional 2D plasmon (2DP) of graphene, which within the gap (where single-particle processes are absent) propagates undamped with a $\sqrt{q}$-like dispersion, as the conventional plasmon of a 2D electron gas [153, 153]. Outside the gap (where single-particle excitations occur), the 2DP mode has a finite linewidth.

---

[2] A symmetric-two-band thigh-binding model considering only the π and π^* bands

The other mode is a well-defined low-frequency acoustic plasmon (AP), whose energy exhibits at long wavelengths ($q \to 0$) a linear dependence on q. While the 2DP mode is present along the ΓK and ΓM paths, the AP mode is present only along ΓK, and strongly depends on the doping level [44, 146]. Fig. 4.12(c) shows how both modes propagate with different energies and shapes with increasing the transferred momentum.
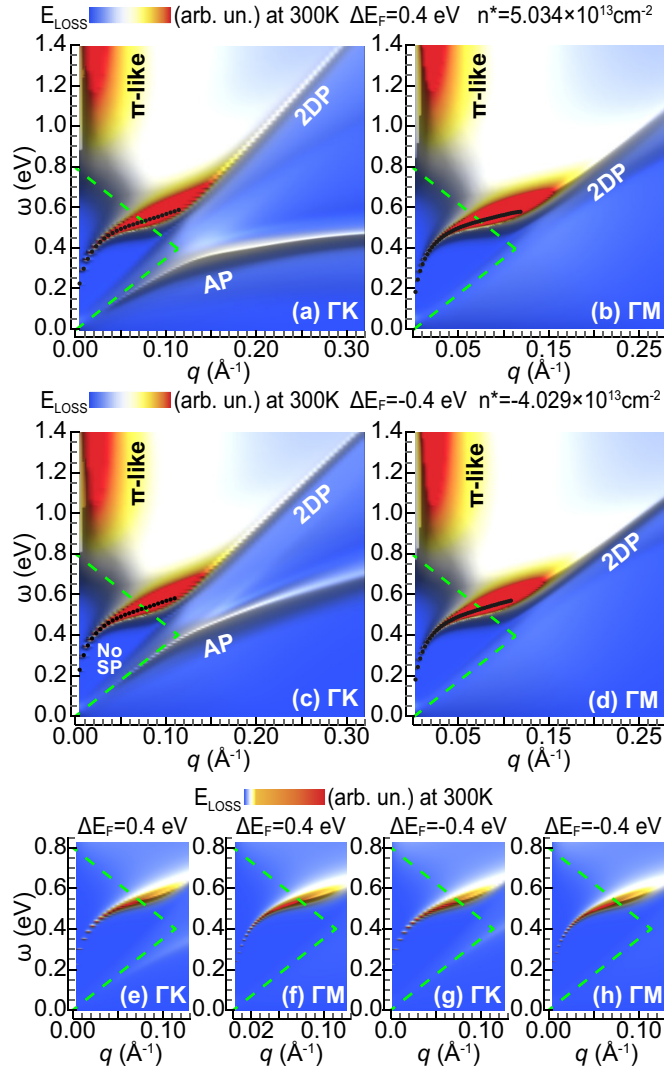

Figure 4.13: Taken from Ref. [145]. Energy-loss function of positively or negatively doped silicene for $\Delta E_F = \pm 0.4$ eV, i.e., E_{LOSS} vs $\omega < 1.2$ eV and $q < 0.27$ Å^{-1} along ΓK [(a),(c)] and ΓM [(b), (d)]. The intensity scale is cut at 5% of the π like plasmon peak [Fig. 4.9], visible at $q < 0.05$ Å^{-1} and $\omega > 0.8$ eV, which corresponds to 0.1% of the 2DP peak. The black dots represent the plasmon condition to occur, i.e., the (q, ω) values at which Re(ϵ^M) = 0 and Im(ϵ^M) is zero or small. These mostly fall in a region where SP excitations are absent, where the 2DP looks like a non-Landau damped peak. An insight onto the no-SP-excitation region (delimited by dashed green lines) is given in (e)-(h), where the intensity scale is cut at 3% of the 2DP peak.

Additionally, Figs. 4.12(d),(e) show the effect of the AP mode in the graphene resistivity. We can see that in the low momentum region the 2DP plasmon seem to dominate the scene, because the band structure anisotropic effects are small [146]. This mode (2DP) has been predicted and analyzed in a number of theoretical studies on extrinsic graphene [44, 146, 154, 155], ranging from two-band models in the Dirac cone approximation to TDDFT approaches and it is at the heart of technological applications in graphene plasmonics. Both collective oscillation (the 2DP and AP) stem from the coexistence of carriers moving with two distinct Fermi velocities [Fig. 4.10] [44, 146]: (i) in one mode (2DP) the two types of carriers oscillate in phase with one another with an energy that is along ΓK slightly larger than along ΓM, in which case only one type of carriers participate and the 2DP dispersion, and (ii) another mode (AP) which corresponds to an acoustic oscillation of lower frequency with the two types of carriers oscillating out-of-phase. If supported by experimental observation, the AP mode will bring new concepts to the field of graphene plasmonics and device design.

Now the loss properties of extrinsic silicene with LDA-optimized geometry (lattice constant $a = 3.82$ Å and buckling parameter $\Delta = 0.45$ Å) is presented in Fig 4.13. We specifically have considered two different charge-carrier concentrations, inducing negative and positive Fermi energy shifts ΔE_F, relative to the Dirac cone. To achieve these extrinsic conditions, we adjusted the occupation factors $f_{\nu \mathbf{k}}$ and $f_{\nu' \mathbf{k+q}}$ in Eq. (3.29) by shifting the Fermi-energy values by $\Delta E_F = -0.4$ and $\Delta E_F = +0.4$ respectively. A summary of the sampled doping levels and corresponding conduction electron or valence-hole densities is given in Table 4.1. The π like and $\sigma + \pi$ plasmons of silicene described above, were found to be rather insensitive to the simulated extrinsic conditions, as already indicated by several studies on graphene-related systems [44, 97, 146, 152, 98].

The energy-loss spectra for $\Delta E_F = \pm 0.4$ eV are shown as density plots in Figs. 4.13. The most striking feature here is the appearance of two distinct plasmon resonances like in graphene. The most intense peak is associated to a 2DP, which is clearly manifested

Table 4.1: Fermi-level shifts ΔE_F induced by adding (+) or removing(-) $\bar{n}_0$ electrons per unit cell, with positive or negative charge-carrier concentrations n_0^*, which correspond to charge-carrier concentrations n^* at $T = 300$ K.

ΔE_F (eV)	$\bar{n}_0$ (el per uc)	n_0^* ($10^{13} \times$ cm^{-2})	n^* ($10^{13} \times$ cm^{-2})
-0.4	-0.0349	-2.764	-4.029
0.0	-	-	0.117
0.4	0.0434	3.437	5.034

along both ΓK and ΓM, and exhibits a $\sqrt{q}$-like dispersion at optical wave lengths ($q \to 0$). A second plasmon corresponds to the AP (it shows a linear energy-dispersion in the low-q limit), which is clearly visible for momentum transfers along ΓK, being generated by the two type of Dirac electrons responsible for the different Fermi velocity values along ΓK [Fig. 4.13(a) and 4.13(c)]. Like in graphene, the 2DP corresponds to the two types of electrons oscillating in-phase with one another, and the AP mode corresponds to electrons oscillating out-of-phase [145].

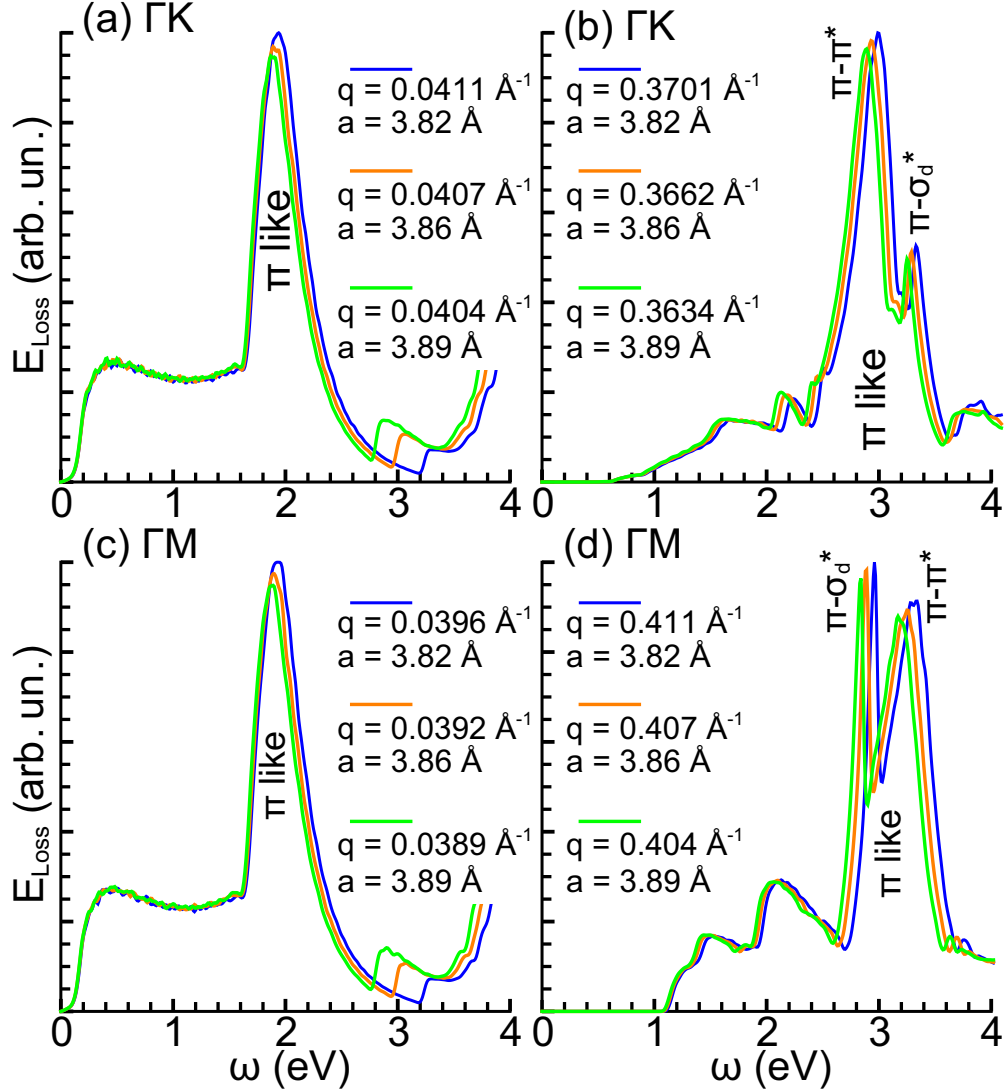### 4.5.3   Unit-cell extension effect on low energy plasmons in silicene

Figure 4.14: Taken from Ref. [145]. E_{LOSS} of undoped silicene vs $\omega \leq 4$ eV for specific small and large q values (in Å^{-1}) along ΓK (a),(b) and ΓM (c),(d). Slightly different lattice constant values (a=3.82, 3.86, 3.89 Å) have been tested.

Now we present how the plasmon response of silicene is affected by geometry, specifically focusing on the intrinsic π like and extrinsic plasmon features, discussed above.

To this end, we applied the TDDFT+RPA scheme on three different Si-Si bond lengths (yielding the lattice constant values a =3.82, 3.86, 3.89 Å that have been quoted in the literature [156, 69]. The buckling parameter has been fixed to its LDA-optimized value in all cases (Δ =0.45 Å). The calculated energy loss E_{LOSS} function is shown in Fig. 4.14 for intrinsic silicene and Fig. 4.15 for extrinsic silicene. The only sensible effect is a red-shift of the π like plasmon peaks with the increase of a.

In particular, at long wavelengths $q \rightarrow 0$, peak variations of 3.8% (along ΓK for

$q = 0.04$ Å^{-1}) and 1.3% (along ΓM for $q = 0.02$ Å^{-1}) are recorded in response to a change in lattice constant of 1.8%. The same change yields a peak variation of 4% at small wavelengths along both ΓK and ΓM for $q = 0.4$-0.45 Å^{-1}. The extrinsic plasmon structure appears to be independent on lattice-constant variations with buckling fixed to 0.45 Å, as considered here.

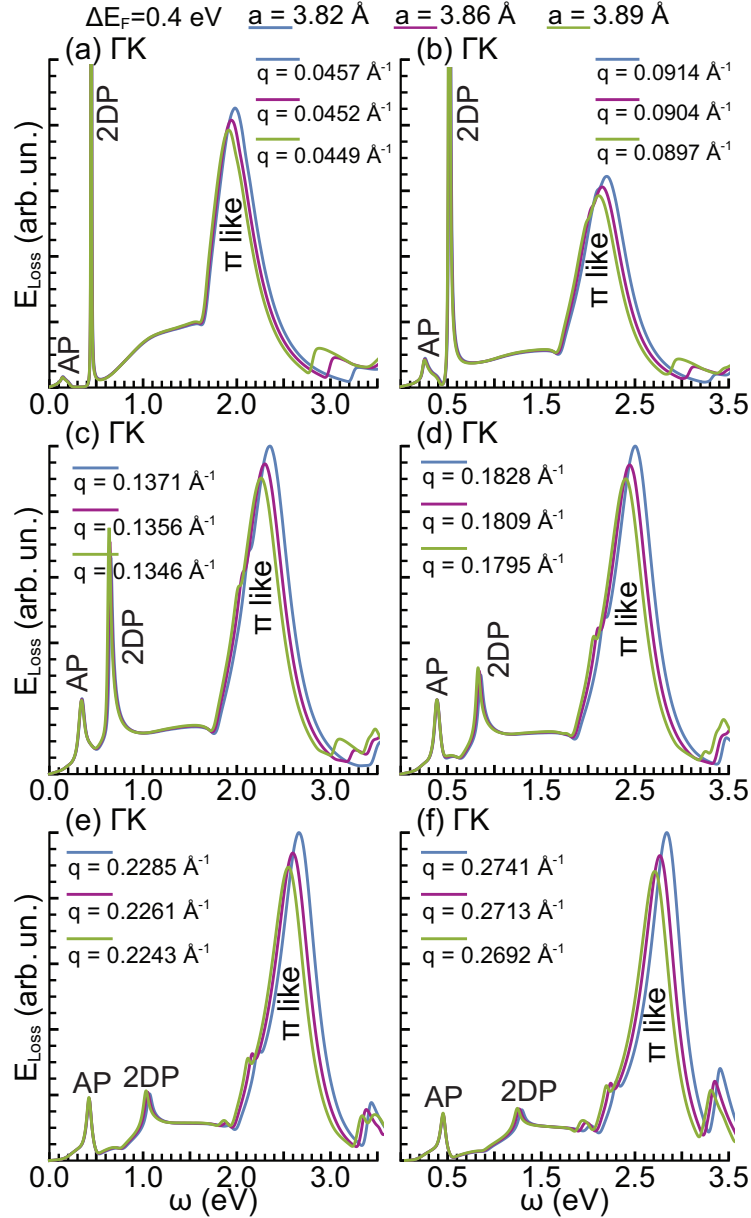Figure 4.15: Taken from Ref. [145]. E_{LOSS} of undoped silicene vs $\omega \leq 3.5$ eV for specific small and large q values (in Å^{-1}) along ΓK. Slightly different lattice constant values (a=3.82, 3.86, 3.89 Å) have been tested.

4.5.4 New extrinsic intraband plasmon in germanene

The energy loss function (at T= 300K) of doped germane is shown in Fig 4.16(a)-(d). Interesting enough, a positive or negative doping ($\Delta EF = \pm 0.4$) produce a gap opening (black triangle) in the single particle excitation region, likely in graphene and silicene. A positive doping of $\Delta E_F = 0.4$ eV that corresponds to charge-carrier concentration of 5.17×10^{13} cm^{-2}, one can observe clearly three distinct plasmon modes along ΓK [Fig 4.16(a)].
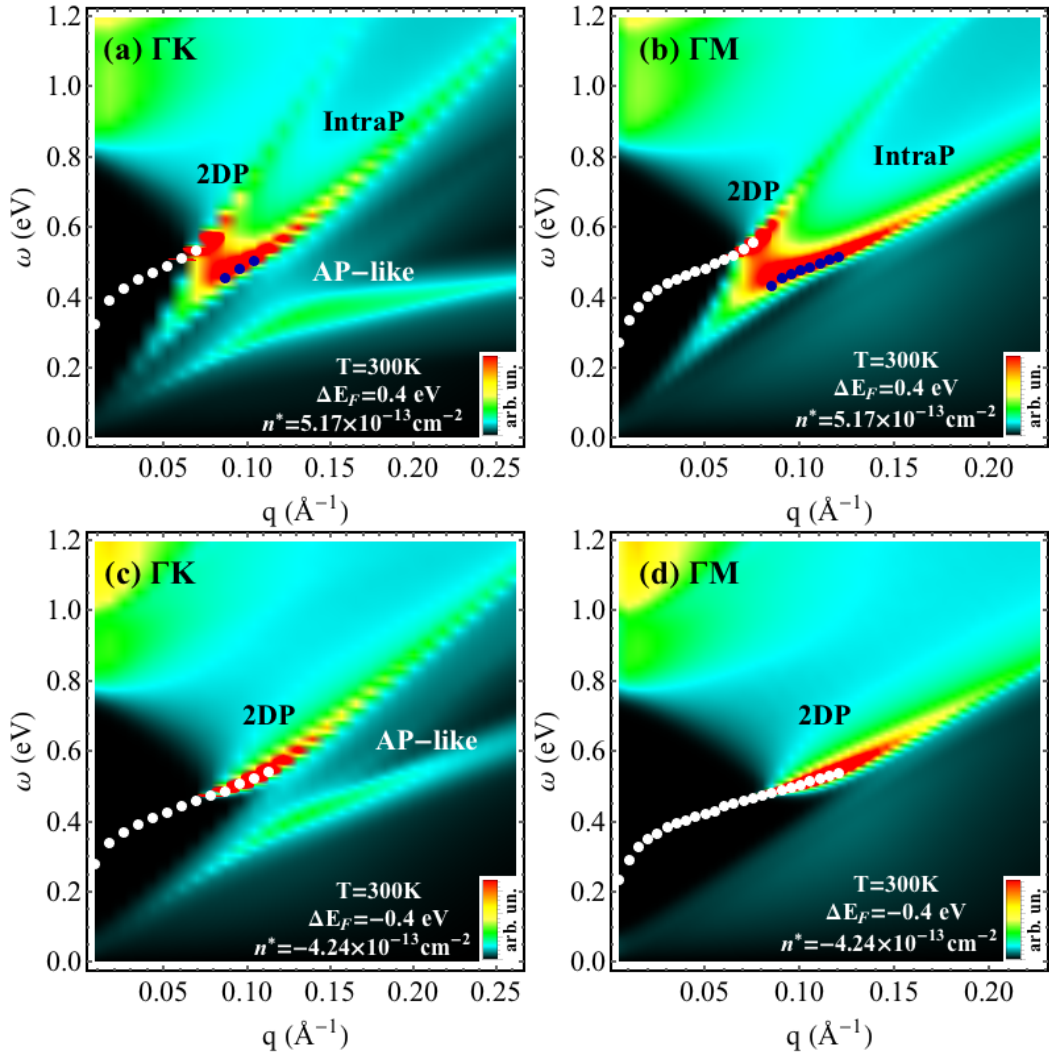

Figure 4.16: E_{LOSS} of positively [(a),(b)] or negatively [(c),(d)] doped germane for $\Delta E_F = \pm 0.4$ eV, $\omega \leq 1.2$ eV and $q \leq 0.25$ Å^{-1}, along ΓK and ΓM paths. The black dots represent the plasmon condition to occur, i.e., the (q,ω) values at which Re(ϵ^M) = 0 and Im(ϵ^M) is zero or small-momentum region where the 2DP and the new intraband plasmon are characterized by zeros in the real part of permittivity and the imaginary part is small (Plasmon condition to occur).

The first mode is the conventional 2DP originated by two electrons oscillating in-phase, and exhibits at long wavelengths a $\sqrt{q}$-like dispersion. In the non-single particle excitation region (black triangle) the 2DP is no damped because it is well-defined by zeros (white dots) in the real permittivity where the imaginary permittivity is small.

The second one is an damped (non-zeros in the real permittivity) acoustic plasmon (AP) originated for two electrons oscillating out-of-phase with two different Fermi velocities and shows a q dispersion dependency. Both collective oscillations have been previously described in silicene and graphene.

Together them a **new extrinsic intraband plasmon**, denoted as IntraP, is predicted to occur. This new mode is activated due to the partial occupation of the σ^* band at the Γ point [see Fig. 4.2(e)] and a q dispersion dependency is observed. This IntraP is found inside of the non-single particle region (black triangle) and defined as undamped mode by zeros (blue dots) in the real permittivity for $0.4 < \omega < 0.5$ eV and $0.8 < \omega < 1.2$ Å^{-1}, furthermore it resides between the 2DP and AP. These three plasmon modes prove to be modulabes changing the doping level (positive or negative) and charge-carrier concentrations. Finally, we can see that the new intraP can be activated along ΓK and ΓM, only with a positive Fermi shift (i.e., doping level) >0.3 eV [Fig 4.16(a),(b)].

Chapter 5

Plasmon modes in graphene nanoribbons (GNRs) arrays

With the rise of low-dimensional materials, a number of theoretical and experimental studies have been oriented to launch, control, manipulate and detect plasmons in graphene-related structures, which are expected to be embedded in next-generation nano-devices that may operate from infrared to terahertz frequencies [157]. As a noteworthy example, graphene nanoribbons (GNRs) preserve most of the exceptional features of monolayer graphene, with the additional property that they are semiconductors and their band-gap is geometrically controllable [157, 84]. Additionally, GNRs have demonstrated an enhanced plasmon response with respect to graphene. A clear picture is experimentally evidenced with the detection of a confined edge (interband) and surface (intraband) plasmons in GNRs, as wide as 100-500 nm, by using nano-infrared imaging technics [36]. On the theoretical side, some nearest-neighbor tight-binding and semiclassical electromagnetic approaches [158, 159, 160], have been able to characterize the intraband mode, being generally excited by a terahertz electromagnetic-field pulse. Very recently, an *ab initio* analysis has elucidated the role of both intraband and interband plasmons in thin GNRs below $\sim 1 - 2$ nm in width [97, 98].

Here, we present an comprehensive characterization of the dielectric properties of semiconducting (armchair) and semimetallic (zigzag) GNRs sorting a wide range of frequencies, from the lower terahertz to extreme ultraviolet (UV). Specifically, we provide an *ab initio* study (based on the methodology introduced in Chapter 3) of plasmon excitations in regular planar arrays of GNRs, whose ends are passivated by hydrogen atoms. This modeling mimics a situation of long suspended ribbons with fixed edges on the far ends.
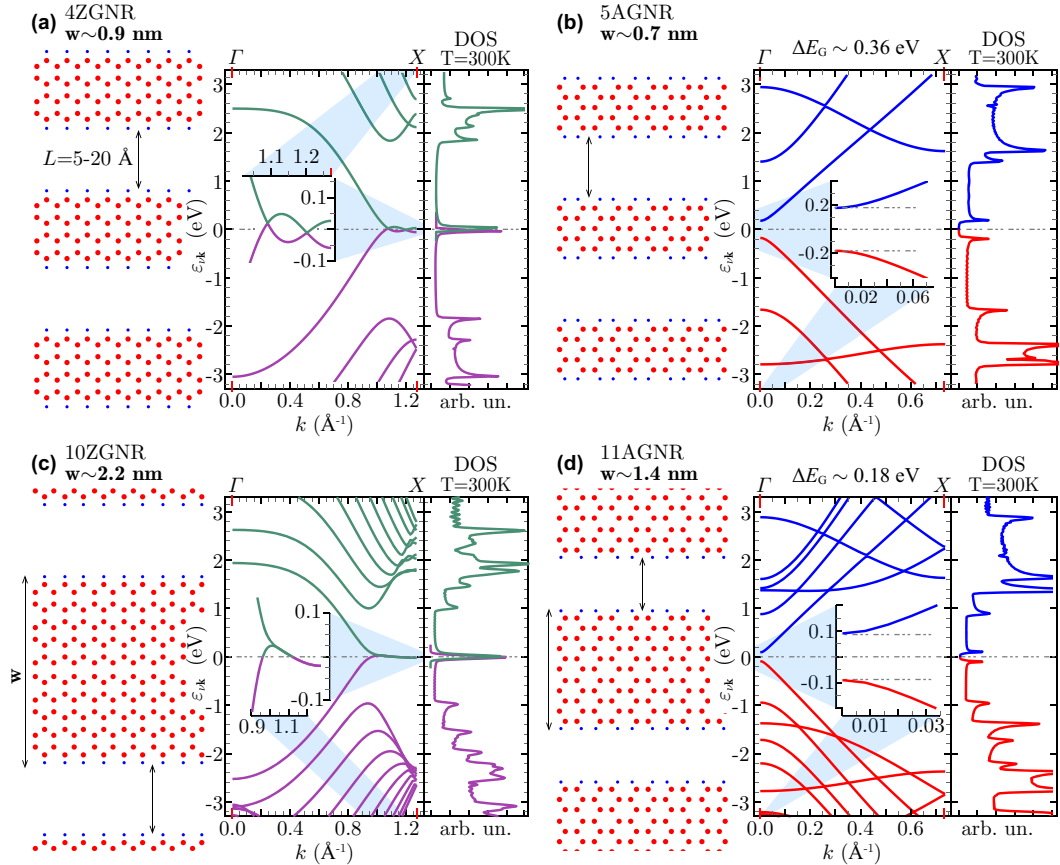
5.1   Computational Details

Figure 5.1: Taken from Ref. [97, 98].Geometry, band-structure and DOS for regular planar arrays of 4ZGNR (a), 5AGNR (b), 10ZGNR (c), and 11AGNR (d). The ground-state features of the different GNRs are strongly sensitive to the value of the C-C bond-length (here fixed to 1.426 Å for the ZGNRs and 1.42 Å for the AGNRs), while they are practically unaffected by in-plane vacuum distances larger than 5 Å.

To begin, we briefly account for the theoretical tools that we have used to explore the electronic structure and dielectric properties of 5AGNR, 11AGNR and 4ZGNR, 10ZGNR (at T= 300K), which are characterized by four, ten zigzag (4ZGNR, 10ZGNR) chains and five, eleven dimer lines (5AGNR, 11AGNR) across the GNR width [84]. The equilibrium electronic structures of the systems are computed using density functional theory (DFT) [140, 141] under the local density approximation (LDA) [142] with suitable norm-conserving pseudopontentials and the Plawe-Wave (PW) basis [143]. Ground state calculations are carried out on a $60 \times 1 \times 1$ Monkhorst-Pack (MP) [124] grid, resulting in a uniform sampling of the first 1st one-dimensional Brillouin zone (BZ), say, the ΓX segment of Fig. 5.2. The converged electron densities are then used to calculate the Kohn-Sham (KS) eigensystems on a denser MP mesh, including 180 points along ΓX and 120 bands, which allows an accurate representation on the dielectric properties of the GNRs on the eV scale.

To explore the infrared band (> 1 eV), a more finely resolved MP sampling is

considered, including roughly 1000 points along ΓX and 30 bands. A correct insight into the lower terahertz region requires an MP sampling of ΓX with 12500 points, which is done by taking into account only the top valence band (VB) and bottom conduction band (CB) of the systems. Permittivity calculations on the full two-dimensional (2D) BZ are performed as well on an MP grid of $270 \times 40 \times 1$ points to scrutinize the role of incident perturbation with oblique propagation vectors, relative to the ribbons axis.

The three-dimensional periodicity required by PW-DFT approach is generated by replicating the GNR arrays over an out-of-plane distance L of 15 Å, which ensures negligible overlap (but not negligible interaction) of the charge density between the replicas. For comparison, we have added in this chapter some features of the dielectric properties graphene.

5.2 Structural and Electronic Properties

In the GNR arrays (5AGNR, 11AGNR and 4ZGNR, 10ZGNR), the C-C length is allowed to range from 1.414 to 1.426 Å, while the C-H bond length is fixed to 1.09 Å, with a bond-angle of 120^0. It has been demonstrated that relaxation effects play a minor role in 4ZGNR and 5AGNR [97]. The main results of our DFT computations are summarized in the plots of Fig. 5.1, which shows the different geometry, band structure and density of states (DOS) of the GNR arrays under study. Zigzag systems, say, 4ZGNR and 10ZGNR behave as semimetals [97, 84], with barely touching valence and conduction bands [Fig. 5.1(a),(c)]. Instead, armchair systems, say, 5AGNR and 11AGNR, are small gap semiconductors [97, 84] [Fig. 5.1(b),(d)], contrary to nearest-neighbor TB approaches in which all AGNRs appear gapless [84, 159].

Indeed, several DFT studies have carefully characterized the band gaps of ZGNRs and AGNRs. In particular, local spin density calculations suggest the opening of a band gap larger than 0.1 eV in ZGNRs [84]. Additionally, GW approaches predict larger band gaps in both ZGNRs and AGNRs by roughly 1 eV with respect to local density calculations [82]. Nonetheless, band-gap values of the same order of the LDA band gap of 5AGNR have been measured for some GNRs as wide as about 20 nm grown on Au(111) [161].

Thus, the application of an RPA scheme to the LDA band structure of 5AGNR and 11AGNR can be of help in interpreting plasmon measurements on currently synthesized GNR structures. Instead, the LDA analysis of a virtually gapless GNR, i.e., 4ZGNR or 10ZGNR, in comparison with 5AGNR and 11AGNR, is particularly instructive to emphasizing the different role played by doping in separating the extrinsic plasmon modes [97, 98].

As for the LDA calculations, the different geometry of the assemblies [Fig. 5.1(a)-(d)] produces electronically distinct band dispersions and DOS. 4ZGNR and 10ZGNR [Fig. 5.1(a),(c)] appear as semimetallic compound with the VB and CB overlaping close to the X point.

The quasi-flat dispersion near the intrinsic Fermi level (E_F) give rise to strong peaks in the DOS, as opposite to graphene where the linear dispersing VB and CB yield a vanishing DOS at E_F. 5AGNR and 11AGNR [Fig. 5.1(b),(d)] are semiconductor with

the VB and CB having parabolic-like dispersions around a small gap of ~ 0.36 eV in 5AGNR and of ~ 0.18 eV in 11AGNR that result in two peaks in the DOS [97, 98]. The peculiar electronic structure of 4ZGNR and 10ZGNR [Fig. 5.1(a),(c)] and 5AGNR and 11AGNR [Fig. 5.1(b),(d)], as compared to the well-known band dispersion of graphene, is reflected in the energy loss (EL) spectra of the intrinsic systems.
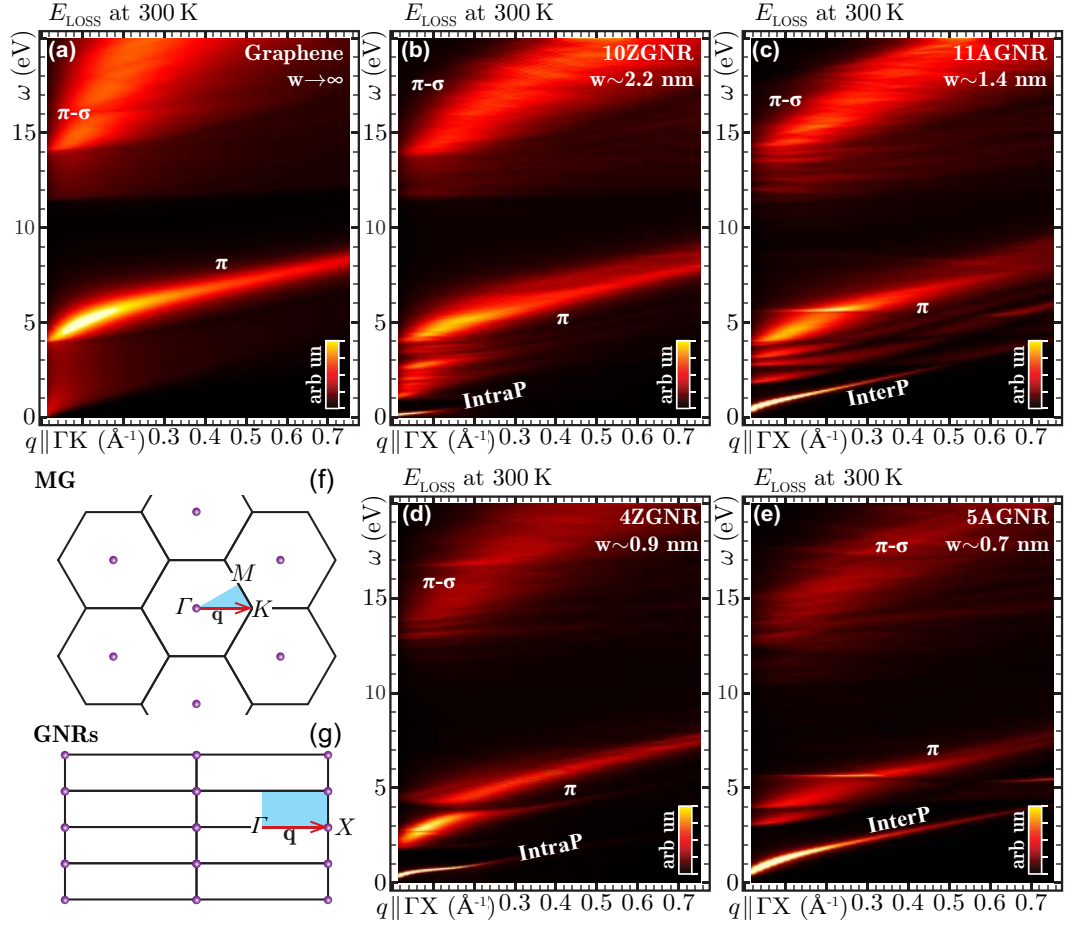

Figure 5.2: Taken from Ref. [98]. EL function E_{Loss} of the undoped systems vs frequency ω (in eV) for incident momenta $\mathbf{q}$ (in $\mathring{A}^{-1}$) along the path ΓX for the different GNRs (for comparison the E_{Loss} of undoped graphene along the path ΓK). The calculations have been performed at room temperature (T=300K). Intraband and interband plasmon modes are denoted IntraP and InterP, respectively. (a) Graphene, (b) 10ZGNR, (c) 11AGNR, (d) 4ZGNR, and (e) 5AGNR.

5.3 High energy plasmons

Independently on the ribbon width ($\sim 0.7 - \sim 2.2$) and chirality (zigzag and armchair conformations), all GNRs are characterized by two interband plasmons at excitation energies above ~ 2 eV that follow one-electron transitions connecting BZ points with high DOS values in the π-π^*, σ-π^* and π-σ^* bands. These excitations, shown in Fig. 5.2(b)-(e), are analogous to the well-known π and $\pi + \sigma$ plasmons of graphene, as displayed in

Fig. 5.2(a). Similar features occur in bilayer graphene, multilayer graphene, graphene-metal interfaces and graphite [20, 34, 162].

In our applications, the intensity of the π and $\pi + \sigma$ modes increases with increasing the GNR-width, getting its maximum brightness in graphene, which may be seen as an infinite-width GNR.

The energy window displayed in Fig. 5.2 does not show the complete energy-momentum dispersion of the $\sigma + \pi$ plasmon, however, the latter seems to be quadratic in graphene and linear in the GNRs. At long wavelengths ($q \to 0$), the π plasmon of all systems has a $\sqrt{q}$-like dispersion, while at $q > 0.2$ $\mathring{A}^{-1}$, it presents a linear behavior. The intrinsic plasmons of 10ZGNR and 11AGNR appear in the same energy region as graphene, i.e., at $\omega \sim 4 - 5$ eV and the $\omega \sim 14 - 15$ eV, respectively. On the other hand, they are red-shifted in 4ZGNR and 5AGNR, with the π plasmon being peaked at $\omega \sim 2 - 3$ eV and the $\omega \sim 13 - 14$ eV.

Furthermore, the π and $\sigma + \pi$ plasmons detected in 4ZGNR ($w \sim 0.9$ nm) and 5AGNR ($w \sim 0.7$ nm) exhibit markedly discontinuous dispersions, being split into more branches. This is a consequence of the narrow-widths of the two systems that generate several, distinct one-dimensional bands of the π and σ character [Fig. 5.1(c),(d)] [97, 98]. By increasing the GNR-width ($w > 1$ nm), the number of bands increases, and less disjoint plasmon dispersions appear, which clearly tend to the continuous patterns of graphene ($w \to \infty$). Thus, semiconducting and semimetallic GNRs have plasmons resonances in the visible (VIS) to ultraviolet (UV) regime that may be controlled by the GNR-width; this tunability feature is evidently absent in graphene.

Now, we can observe that quantum confinement and chirality are key factors for plasmon resonances at frequencies smaller than 2 eV even in intrinsic conditions. We see that zigzag systems exhibit an extra intraband plasmon (denoted IntraP), while armchair systems present an extra interband plasmon (denoted InterP) [Fig. 5.2(b)-(e)]. These two modes correspond to the surface (IntraP) and edge (InterP) plasmons detected in large-width, extrinsic GNR-arrays fabricated on Al_2O_3 [36].

The surface plasmon of ZGNRs is originated by the large DOS-peak observed at the Fermi energy (E_F) [Fig. 5.1(a),(c)]. This mode shows a $\sqrt{q}$-like dispersion and seems to be analogous to the *conventional* 2D plasmons of extrinsic graphene. The edge plasmon of AGNRs appears as an effect of collective excitations generated close to E_F, associated to single-particle excitations that connect the two DOS-peaks around E_F [Fig. 5.1(b),(d)]. The characteristics of this interband mode are similar to those of the π plasmon of intrinsic graphene, i.e., at long wavelengths the interband plasmon shows a $\sqrt{q}$-like dispersion, while at $q > 0.1$ $\mathring{A}^{-1}$ it displays a linear dispersion.

5.4 Low energy plasmons

5.4.1 Intrinsic plasmons

A detailed analysis of these plasmon structures are more clearly visible in Fig. 5.3(a)-(d) and Fig. 5.4(a)-(d) that correspond to 4ZGNR and 5AGNR, respectively. The large DOS value close to E_F in 4ZGNR yields a concentration of $n^* = 3.96 \times 10^{12}$ cm^{-2}
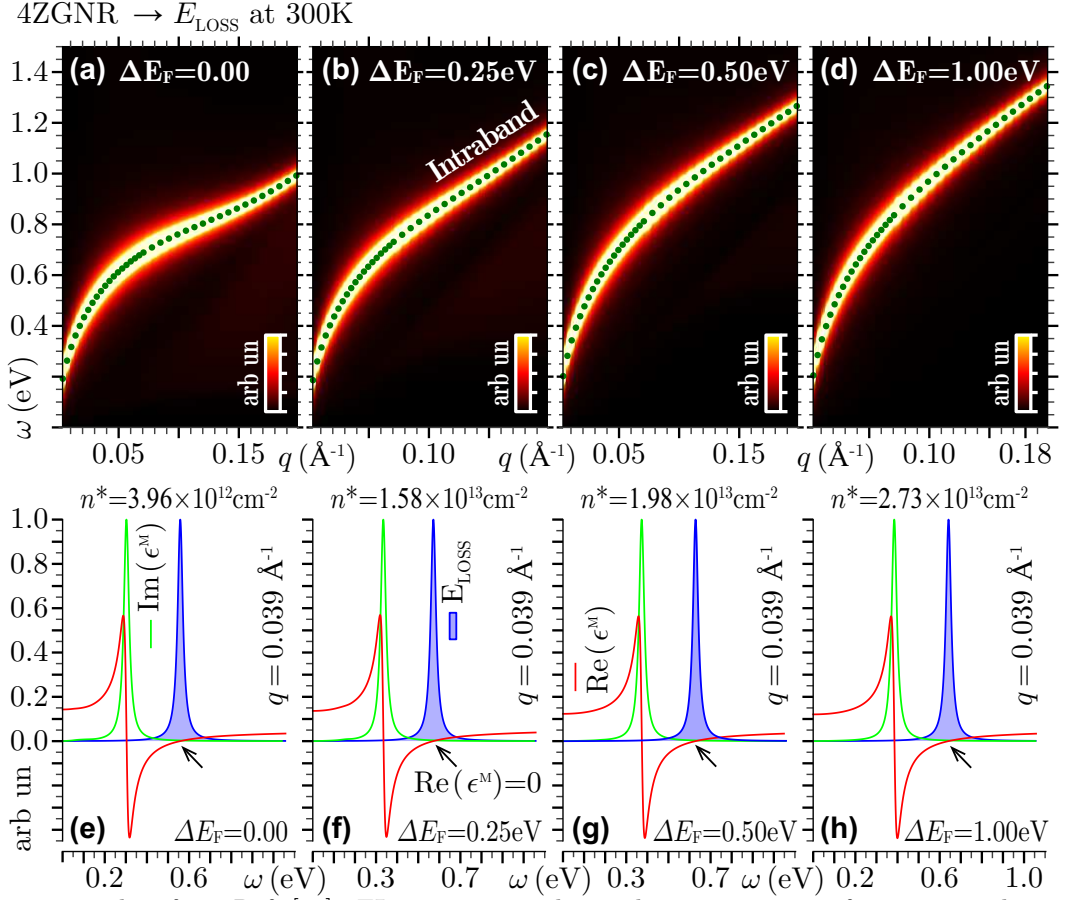
Figure 5.3: Taken from Ref. [97]. EL spectrum and complex permittivity of intrinsic and extrinsic 4ZGNRs at room temperature. (a-d) E_{Loss} vs $\omega < 1.5$ eV and $q < 0.18$ Å^{-1}. (e-h) Re(ϵ^M), Im(ϵ^M) and E_{Loss} vs $\omega < 1.5$ eV at $q = 0.039$ Å^{-1}. The dark green dots denote the (ω, q)-dispersion of the IntraP, and n^* being the concentration of conduction electrons. The vertical grid-lines mark the q value used in the plots of (e-h).

conduction electrons, which allows the appearance of an intraband plasmon with $\sqrt{q}$-like dispersion, where the charge-carries located on each ribbon of the array oscillate as a single 2D gas [Fig. 5.3(a)]. The latter has been mostly observed in graphene, which even in the intrinsic case allows for a weak intraband contribution at room temperature due to a concentration $n^* = 1.15 \times 10^{11}$ cm^{-2} conduction electrons.

On the other hand, the energy gap at E_F in 5AGNR yields a negligibly small intra-band mode due to the tiny concentration of conduction electrons at room temperature of $n^* = 8.70 \times 10^8$ cm^{-2}. The latter can be characterized at small momentum. In contranst, an interband 2D plasmon is clearly recorded in the low-energy spectrum of 5AGNR, as testified by the intense signal in Fig. 5.4(a)-(d); this corresponds to a collective mode that is triggered by transitions between the valence and conduction DOS peaks at Γ [Fig 5.1(b)]. The collective nature of the newly detected modes in 4AGNR and 5AGNR is proved in Fig 5.3(e) and Fig 5.4(e), respectively, where we see that each excitation peak in the EL spectrum corresponds to a zero in the real permittivity Re(ϵ^M), at a frequency where the imaginary permittivity Im(ϵ^M) is small.
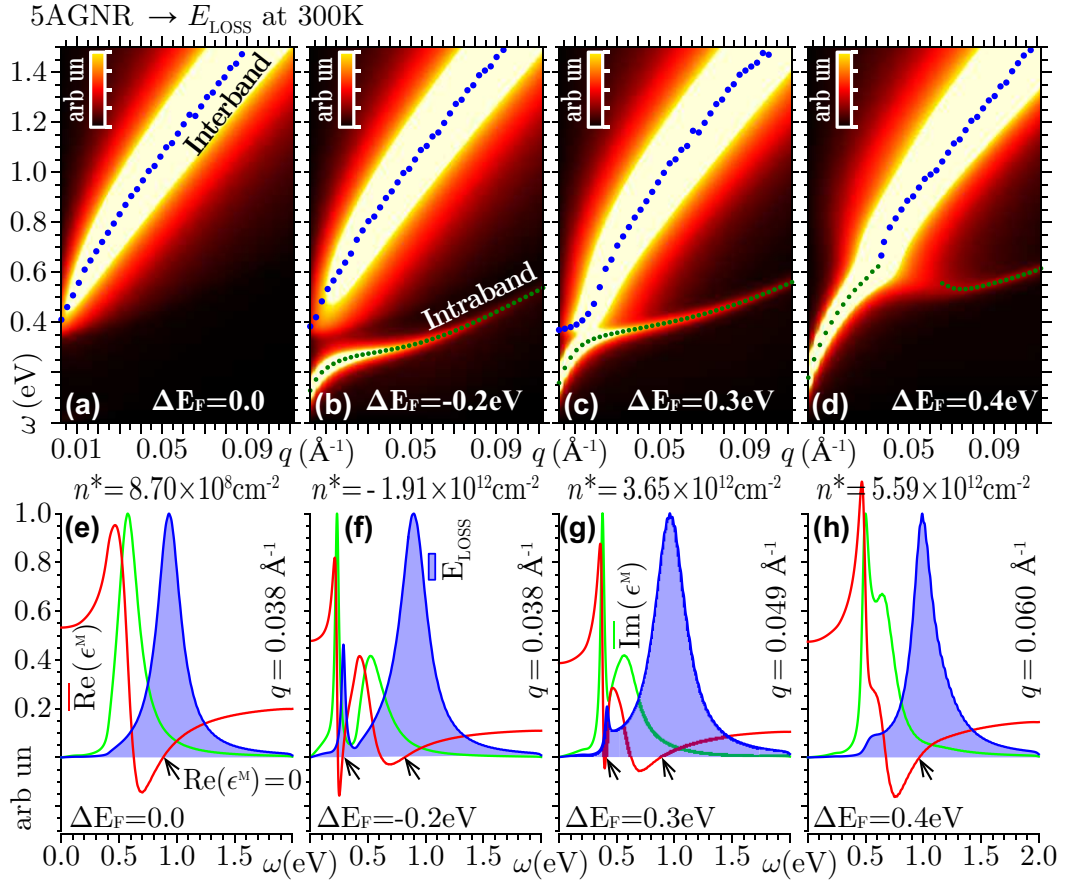
Figure 5.4: Taken from Ref. [97], EL spectrum and complex permittivity of intrinsic and extrinsic 5AGNRs at room temperature. (a-d) E_{Loss} vs $\omega < 1.5$ eV and $q < 0.11$ Å^{-1}. (e-h) $Re(\epsilon^M)$, $Im(\epsilon^M)$ and E_{Loss} vs $\omega < 2$ eV at $q = 0.038$ Å^{-1} [(e),(f)], $q = 0.049$ Å^{-1} (c) and $q = 0.060$ Å^{-1} (d). The dark green and blue dots denote the (ω, q)-dispersion of the IntraP and InterP, respectively, and n^* being the concentration of conduction electrons. The vertical grid-lines mark the q value used in the plots of (e-h).

These excitations are indeed genuine plasmons [97, 98], which can be used in practical terahertz applications. Moreover, as is the case of the high-energy π excitations, these low-energy modes arise from transitions involving the π bands, which means that their intensities and energy-momentum dispersions can be modulated according to external factors that change the band levels, such as the already mentioned ribbons width, in-plane distance and chirality.

5.4.2   Extrinsic plasmons

Now the dielectric properties of the GNR arrays are investigated by injection/ejection of electrons, i.e., by doping or gating. Extrinsic systems are simulated here by slightly changing the level populations in Eq. (3.29), in such a way that band dispersion and single-particle KS orbitals are negligibly altered by the applied variations of the $f_{\nu\mathbf{k}}$ factors. For doping levels ΔE_F not larger than ~ 1 eV the high-energy end ($\omega > 2$ eV) of our EL spectra is practically unaffected [97, 98].

On the contrary, unprecedented new features are recorded at the low-energy end ($\omega < 2$ eV). In Fig. 5.3(a)-(d) we show the low-ω and low-$\mathbf{q}$ region of the EL spectrum of the 4ZGNR array, zooming on the undoped case ($\Delta E_F = 0$) and analyzing three positive doping levels, namely $\Delta E_F = 0.25, 0.5, 1.0$ eV.

In all cases, we observe a single dispersive structures, the intraband plasmon, which is a genuine collective mode, with the EL peak corresponding to a zero in $\text{Re}(\epsilon^M)$ and a small value of $\text{Im}(\epsilon^M)$ [see. Fig. 5.3(e)-(h)]. We also notice minor differences in the four EL spectra, with the plasmon energy slightly increasing with increasing ΔE_F [Fig. 5.3(a)-(d)].

More interesting features are observed in doped arrays of 5AGNR, whose low-ω and low-$\mathbf{q}$ response is show in Fig.5.4. In the undoped case ($\Delta E_F = 0$) a single dispersive peak is detected in the EL spectrum, which represents an interband plasmon following coherent electronic excitations between the VB and CB.

When a small doping is introduced ($\Delta E_F = -0.2, 0.3$, values experimentally available [82]) the conduction conduction electron/valence hole concentration bursts from $\pm 10^9$ to $\pm 10^{12}$ cm^{-2}, and another dispersive peak appears in the EL spectrum due to a clearly resolved intraband plasmon [see Fig. 5.4(b),(c),(f),(g)]. For these low wavevectors ($q < 0.02$ Å^{-1}), the intraband mode is the most intense contribution, while the interband plasmon is depressed because the doping partially fills the CB near Γ thus inhibiting quasi-vertical ($q \to 0, \omega$) interband transitions. In the $0.02 < q < 0.06$ Å^{-1} region, both the intraband plasmon becomes the most intense peak while the intraband plasmon is strongly damped.

A slightly larger value of the doping ($\Delta E_F = 0.4$ eV) leads to an even more intriguing situation: the single dispersive peak visible in Fig. 5.4(d),(h) has a **double nature**, as testified by the kink in peak dispersion and the abrupt decrease in intensity (increase in width) found at $q \sim 0.05$ Å^{-1}. Indeed, interband transitions between the high-DOS points of Fig. 5.1(b) for $q < 0.04$ Å^{-1} are strongly quenched by electron population of conduction levels.

Thus, the intense peak showing the pq dispersion is mostly originated by the intraband plasmon. Conversely, for $q > 0.04$ Å^{-1} the intraband plasmon enters a region where it is damped by interband transitions; as a result, most of the spectral weight is concentrated on the interband plasmon, while the overdamped intraband plasmon only appears as a faint peak.

5.4.3 Oblique extrinsic plasmons

Now, let us briefly focus on how the interplay between the intraband and interband modes can be also detected by probing 5AGNR with oblique incident momenta of in-plane modulus q forming different angles θ relative to the ribbon axis. This is shown in Fig. 5.5 where the 1^{st}BZ of the system with an MP mesh of $270 \times 40 \times 1$ points.

We see that specific combination of incident momentum/angles lead the two modes to be superimposed, whereas other choices leave the two peak-structure separated in momentum space. At $\theta = 0^o$ and $\theta = 33.4^o$ both plasmon modes exist, however, at $\theta = 69.2^o$ the interband is well-defined only at specific momentum values ($q > 0.012$
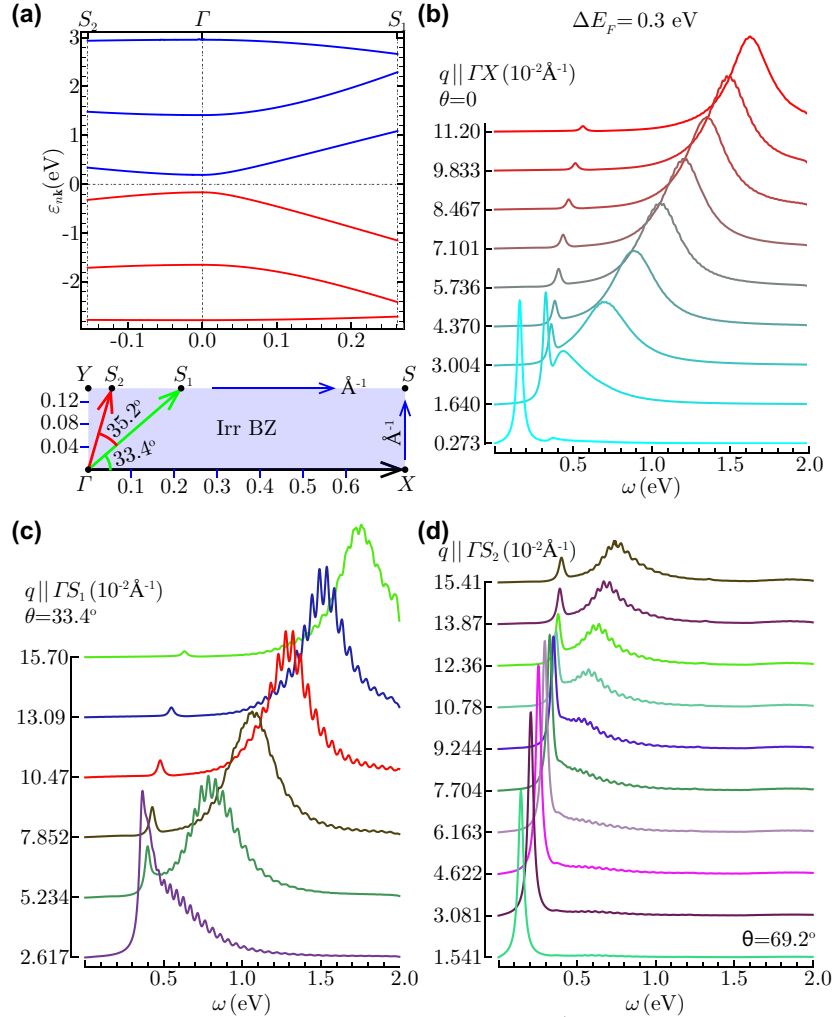
Figure 5.5: Taken from Ref. [97]. Band structure (a, Top), 1^{st}BZ (a, Bottom) and loss spectrum of extrinsic 5AGNRs at $T = 300$ K, $\Delta E_F = 0.3$ eV. The E_{Loss} curves are obtained by re-sampling 1^{st}BZ with an MP mesh of $270 \times 40 \times 1$ k–points. These are shown vs $\omega < 2$ eV for some incident momenta along different directions, forming angles of $\theta = 0$ (ΓX, b), 33.4 (ΓS_1, c) and 69.2° (ΓS_2, d) relative to the ribbon axis.

Å^{-1}) [Fig. 5.5(d)].

5.4.4 Temperature effect on plasmon response

As shown in the previous subsections, the large tunability in the intraband plasmon mode of 5AGNR is critically dependent on the electron (hole) occupancy of conduction/valence states, lying within an energy window of $0.5 - 1.0$ eV around the Fermi level. Such a population is given by the Fermi-Dirac statistical factors $f_{v\mathbf{k}}$ and $f_{v\mathbf{k}+\mathbf{q}}$ that are significantly influenced, within the considered energy range, by even moderate temperatures changes below ~ 1000 K. This effect inevitably plays a major role in any nanodevice design approach.

To quantify and characterize it, we ran EL calculations on undoped 5AGNR with

electronic temperature values larger than 500 K. All other settings were the same as for room temperature calculations. The resulting EL spectra are reported in Fig. 5.6 for energies below ~ 1 eV and momentum smaller than 0.03 Å^{-1}.

At $T = 300$ K, the interband plasmon is clearly visible. Nevertheless a faint intraband peak may be spotted at energies below ~ 0.1 eV, and the intraband plasmon dispersion can be computed. As the temperature is increased to 500 K, the intraband plasmon peak beings to appear in the same intensity scale as the interband plasmon. At higher temperatures, say, T=700, 900 K, the intraband plasmon is well resolved and also well separated from the interband plasmon.
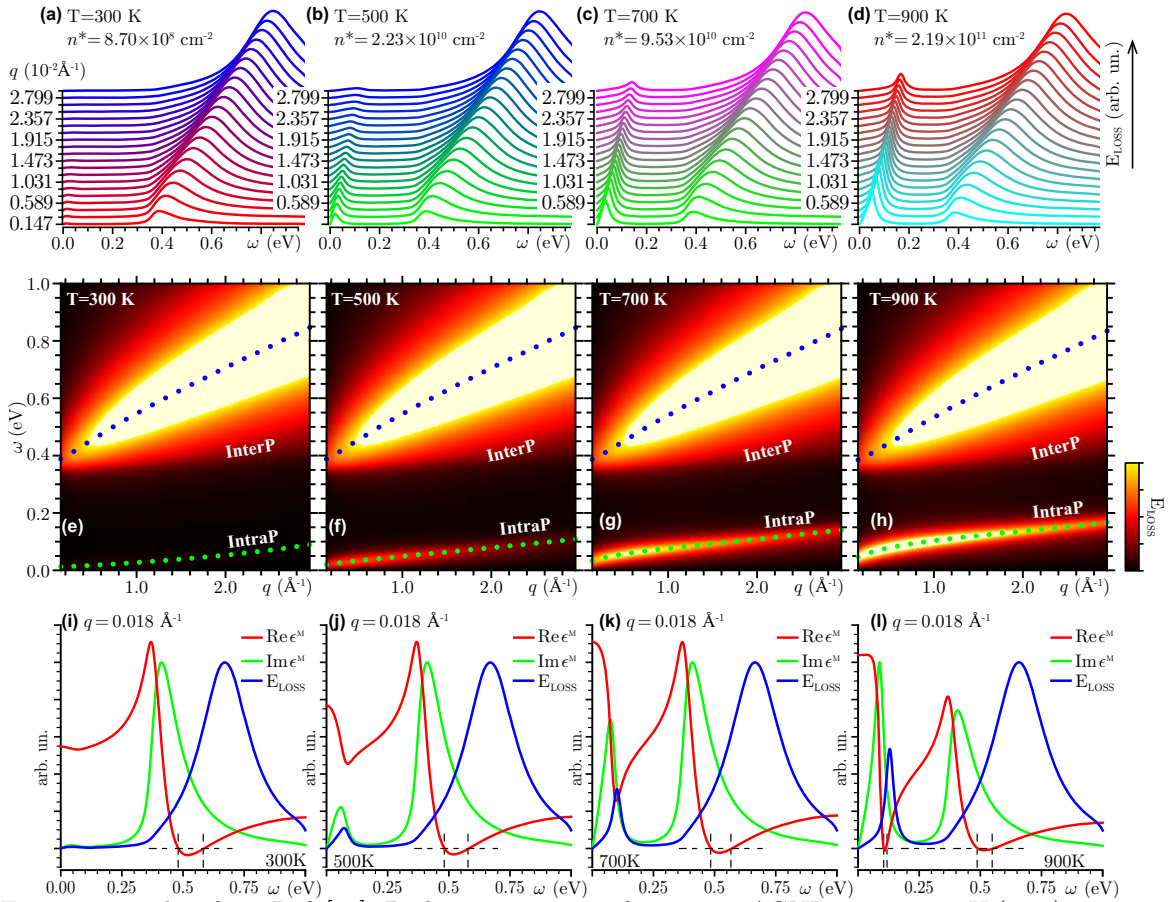

Figure 5.6: Taken from Ref. [97]. Dielectric response of intrinsic 5AGNR at $T = 300$ K (a,e,i), $T = 500$ K (b,f,j), $T = 700$ K (c,g,k), $T = 900$ K (d,h,l). E_{Loss} is represented as sequence of shifted spectra in (a-d) and density plots in (e-h). The green and blue dots denote the intraband and interband plasmon (ω, q)-dispersions, respectively. $\text{Re}(\epsilon^M)$, $\text{Im}(\epsilon^M)$ and E_{Loss} vs $\omega < 1$ eV at $q = 0.018$ Å^{-1} in (i-l). The dashed gridlines indicate the zeroes of $\text{Re}(\epsilon^M)$.

The increase of the intraband plasmon intensity is readily understood considering how the electronic temperature affects the population of the KS states near theFermi level. At room temperature the number of electrons that are capable to overcome the 0.36 eV gap is small, with a concentration of the order of 10^9 cm^{-2}. Thus, interband excitations are dominant. At T= 500 K the electron population of the conduction band becomes appreciable, with a concentration of roughly 2×10^{10} cm^{-2}, generating the

small peak in the EL spectrum. As the Temperature further increases (T≤ 700 K), the smearing width of the Fermi-Dirac distribution function increases, the conduction electron concentrations become larger than 10^{11} cm^{-2}, and the intraband plasmon fully appears in the EL spectrum. Charge carrier concentrations triggered by temperature increase are nevertheless much smaller than those obtained with doping or gating. For this reason, no particular interference is recorded in Fig. 5.6 between intraband and interband plasmon modes. It should be however mentioned that in the realistic case of GNR-arrays suspended on top of a substrate, the substrate phonons become relevant and significantly affect the plasmon damping at temperatures above 500 K.

5.5   Tunable edge and surface plasmons

We proceed by clarifying the role played by the geometric and conformational parameters in the different GNRs, whose intrinsic response is shown in Fig. 5.2 together with that of graphene. In the following, we will also evaluate several extrinsic conditions associated to Fermi energy shifts ΔE_F in the range of -0.2 to 0.2 eV. The simulations characterize the tunability properties of the GNR-plasmons. In particular, (i) GNR-widths(w) around 0.7-2.2 nm are sorted out; (ii) zigzag and armchair edges are considered, to elucidate the role played by chirality; (iii) in-plane vacuum distances from 5 to 20re tested; (iv) different unit-cell extensions are simulated by changing the C-C bond of about 0.5%, to account for stretching effects.

5.5.1   Ribbon width and chirality

In Fig. 5.7 we report the macroscopic dielectric function and the EL function of the different GNR-arrays for a selected momentum value($q = 0.011$Å^{-1}) and a negative doping level ($\Delta E_F = -0.1$eV). We see that 10ZGNR and 4ZGNR present similar plasmonic features, with the intraband plasmon resonance being blue-shifted by increasing the GNR-width [Fig. 5.7(a),(c)].

In 11AGNR and 5AGNR, not only the peak position but also the interplay of the interband and intraband plasmon is strongly dictated by the doping level and the GNR-width [Fig. 5.7(b),(d)]. In 5AGNR, the two modes are well resolved in energy, with the zeroes of the real permittivity being hidden by the Landau damping mechanism, associated to single-particle excitation processes.

In 11AGNR the same modes strongly interfere and largely dominate with respect to single-particle excitations. A similar interplay was observed in extrinsic 5AGNR subject to a positive doping of about 0.3 eV. These outcomes are basically due to the different band gap values of the two AGNRs, which according to our predictions are ~ 0.18 eV for 11AGNR, and ~ 0.36 eV for 5AGNR. Accordingly, less energy requirements are needed to produce a well-defined intraband collective electronic excitation in 11AGNR.

On the other hand, a positive doping larger than 0.2eV yields a well-defined intraband plasmon in 5AGNR. Interestingly enough, some GNRs with band gap values of the same order of 11AGNR and 5AGNR have been recently synthetized on Au (111) [161].

Then, our ab initio analysis can be of help in interpreting plasmon measurements on currently synthesized GNR-structures.

Chirality seems to be a major key-point for the design of GNRs-based plasmonic devices. One or two plasmon modes can be exploited, depending on the shape of the GNR-edges. In this respect, negative or positive doping acts as a modulating factor of the plasmon modes [98].
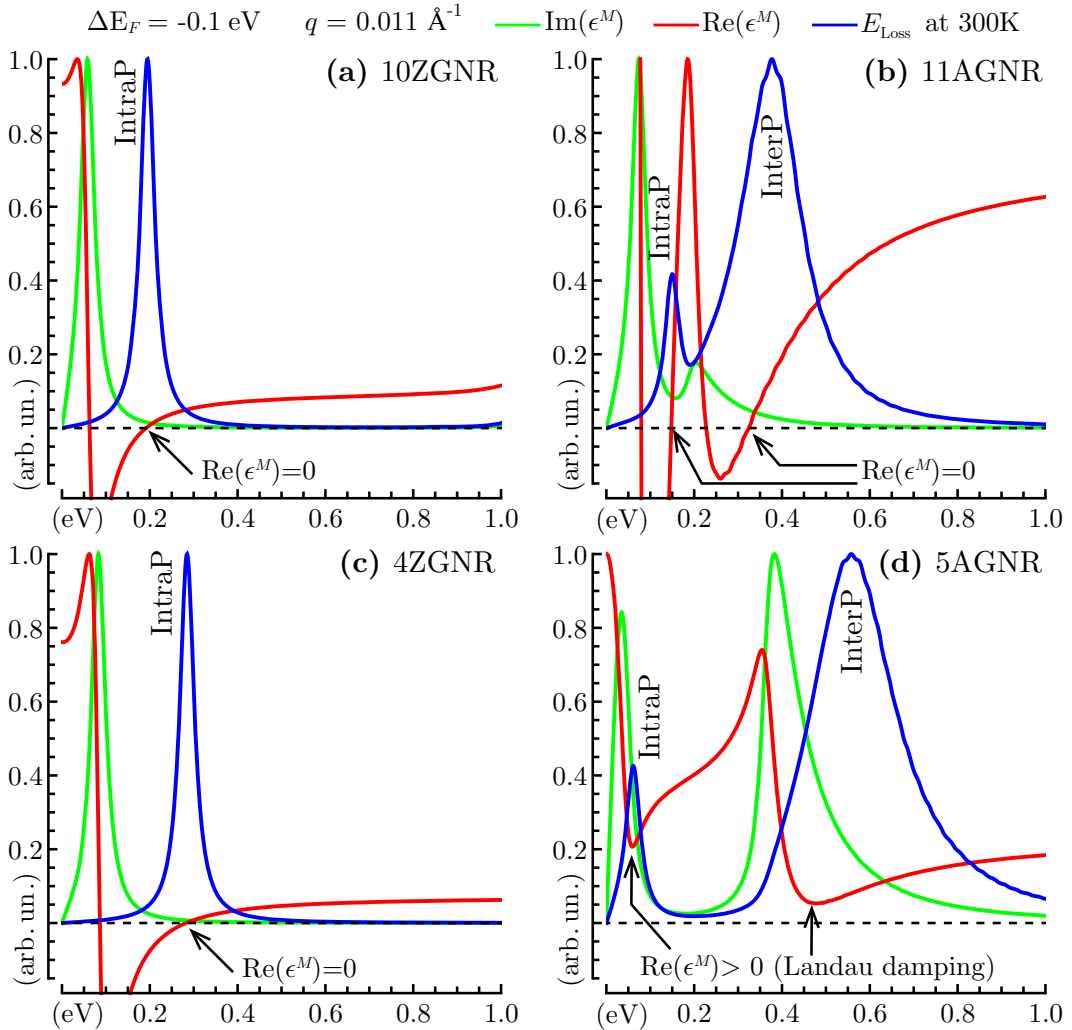

Figure 5.7: Taken from Ref. [98]. Macroscopic permittivity and EL function for (a) 10ZGNR, (b) 11AGNR, (c) 4ZGNR and (d) 5AGNR. The energy region $\omega \leq 1$ eV is explored at a fixed momentum along ΓX ($q = 0.011$ Å^{-1}) and a negative doping level ($\Delta E_F = -0.1$ eV). The intraband and interband plasmons are denoted IntraP and InterP, as in Fig 5.2.

In Fig. 5.8 we see that a change in doping sign, from -0.1 to 0.1 eV, produces a slight red-shift in the intraband plasmon of 10ZGNR and the interband plasmon of 11AGNR [Fig. 5.8(a),(b)]. More significant variations are observed in the intraband plasmon of 11AGNR, which is markedly blue shifted and doubled in intensity by the same change of extrinsic conditions [Fig. 5.8(b)]. Therefore, an asymmetric response is observed in the intraband plasmon of semiconducting GNRs [Fig. 5.8(b)]. Moreover,
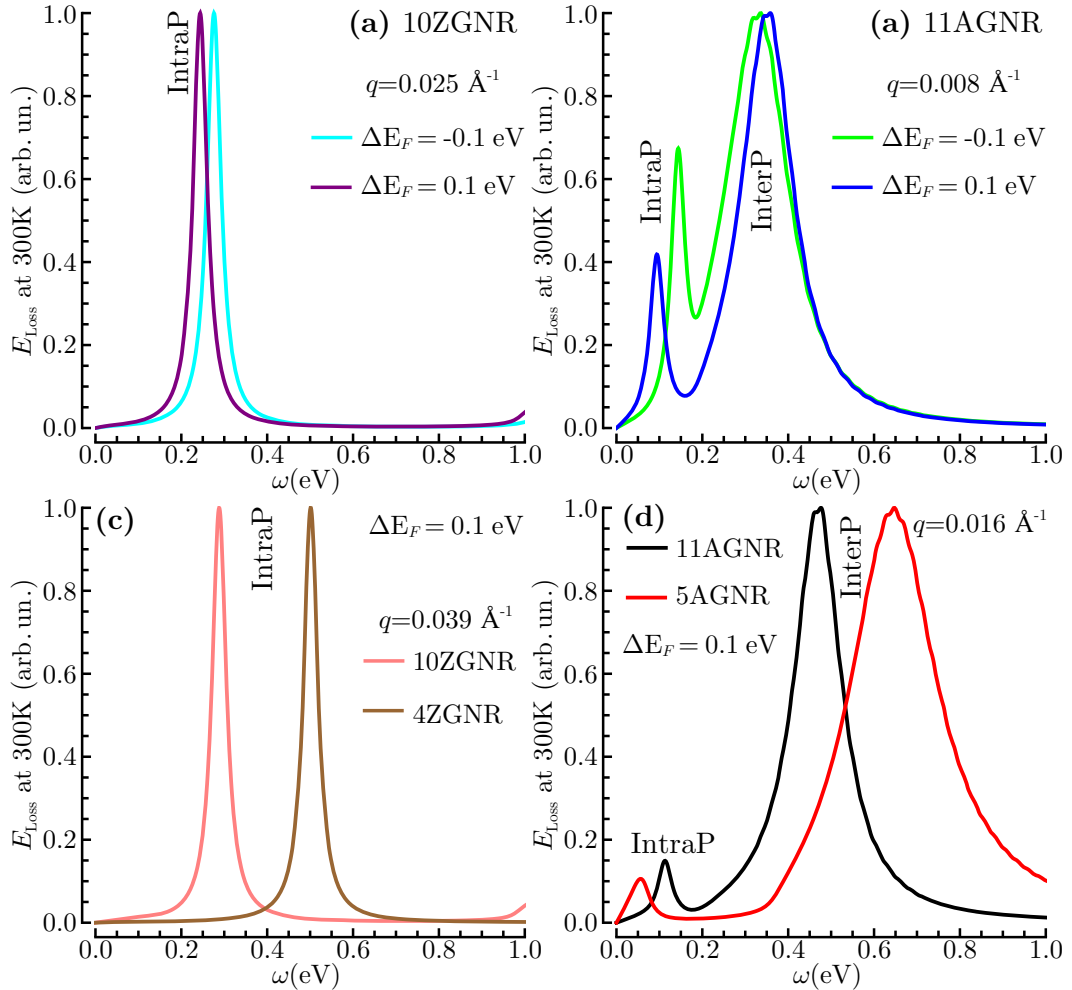
Figure 5.8: Taken from Ref. [98]. The EL function (E_{Loss}) of 10ZGNR, 11AGNR, 4ZGNR and 5AGNR is reported vs $\omega \leq 1$ eV at different doping levels of ± 0.1 eV and transferred momentum values along the path ΓX.

as the GNR-width decreases an appreciable blue/red shiftis detected in the plasmon peaks of both ZGNRs and AGNRs [Fig. 5.8(c),(d)]. Thus, a tunable energy response may be more strongly influenced by the ribbon width than the doping level.

5.5.2   Mechanical deformations

Now we see how the fascinating plasmonic features of semiconducting GNRs are affected by changes the in-plane separation. With reference to the 5AGNR-case, we take a positive doping value of 0.2 eV and consider vacuum distances L, between continuous arrays, in the range of 5 to 20Å[Fig. 5.9]. As a first result, we see that both intraband and interband plasmon modes exist in 5AGNR, no matter how far apart the arrays are. The intraband plasmon is however affected in intensity, while the interband plasmon is blue-shifted as the vacuum distance decreases down to 5 Å. This effect is clearly visible at $q = 0.025$Å^{-1} in Fig. 5.9(d), where a broad interband plasmon peak is detected at $\omega \sim 0.6 - 1$eV.
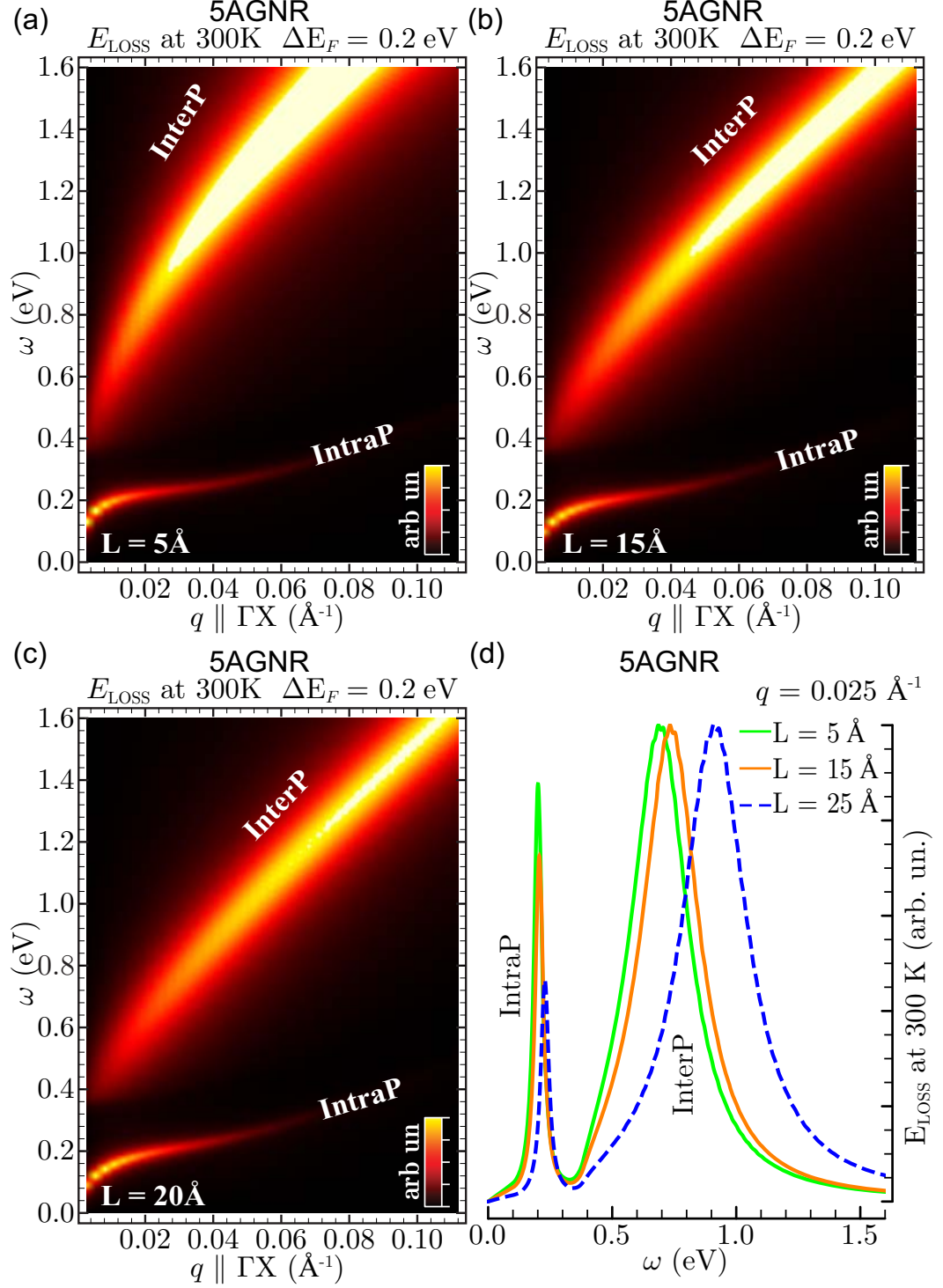
Figure 5.9: Taken from Ref. [98]. (a)-(c) EL function (E_{Loss}) of positively doped 5AGNR vs $\omega < 1.6$ eV and $q < 0.12$ Å^{-1} along ΓX, with three different values of the in-plane vacuum distance L=5, 15, 20 Å^{-1}; (d) Comparison the different of panels (a)-(c) at $q = 0.025$ Å^{-1}.

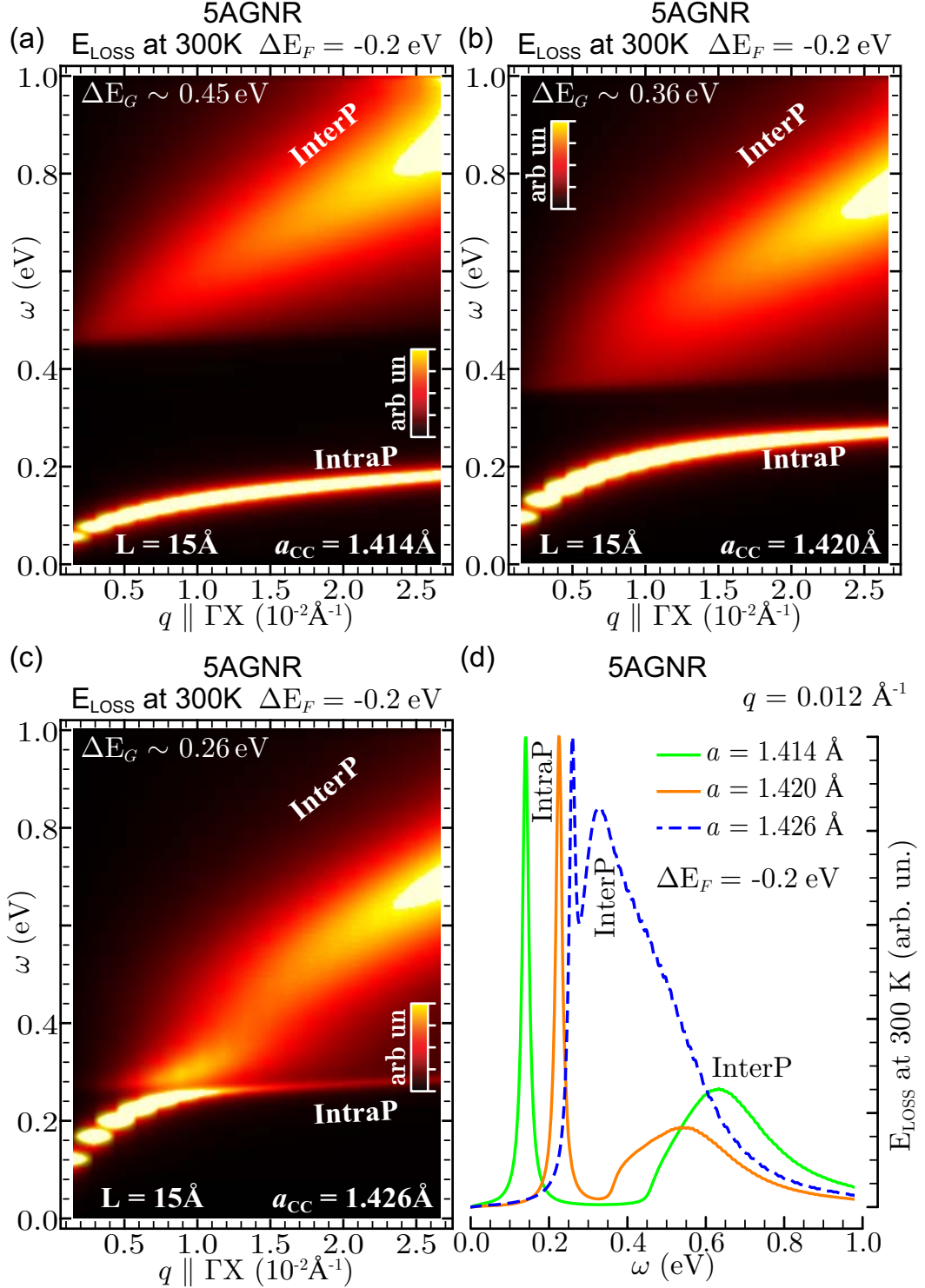Figure 5.10: Taken from Ref. [98]. (a)-(c) EL function (E_{Loss}) by stretching effects of negatively doped 5AGNR vs frequency ω (in eV) for a momentum $\mathbf{q}$ (in Å^{-1}) along path ΓX. Lattice constants along axis: (a) $a = 1.414$ Å^{-1}, (b) $a = 1.420$ Å^{-1}, and (c) $a = 1.426$ Å^{-1}. (d) Comparison of E_{Loss} vs $\omega \leq 1$ eV at $q = 0.012$ Å^{-1} as function of the a.

Both the large blue-shift of the interband plasmon, and the intensity decrease of the intraband plasmon, are consistent with the idea that as the GNR-arrays get closer a large graphene area is created. When the vacuum distance becomes negligibly small, the interband plasmon detected in AGNRs enters the region where the π plasmon of graphene are found, while the intraband plasmon decreases in intensity to a small contribution, reported in room temperatures calculations of slightly doped graphene.

Finally, we show how the intraband and interband plasmons of 5AGNR are affected by stretching/shrinking the unit-cell of the system of about 0.5%, with respect to its nominal value associated to a C-C bond-length a of 1.42 Å. In this application, the in-plane vacuum distance is fixed to 15 is and a negative doping level of 0.2 eV is considered. As shown in Fig. 5.10, the band gap decreases with increasing stretching the unit-cell from $a = 1.414$ to $a = 1.426$ Å.

Accordingly, the interference between the intraband and interband plasmons strongly increases. A similar interference has been reported in undeformed 5AGNR-arrays doped by positive Fermi energy shifts larger than 0.4 eV, however, such doping values seem to be impractical for current GNR applications.

5.6   Semiclassical and Tight binding vs TDDFT

First, we have compared the electronic properties of GNRs with widths of $\sim 0.7 - 1.4$ nm. Recently, GNRs of the same order of width (5-10nm) have been synthesized on germanium substrates with well-defined armchair shaped edges [85, 163]. Thus, the application of the TDDFT+RPA approach to 5AGNR is appropriated and useful to interpret the plasmon measurements on currently synthesized armchair GNR structures. In Fig. 5.11(b),(f) we report the LDA band structure of the AGNRs, which appear as semiconductors characterized by small band gap values ΔE_G of 0.36 and 0.18 eV [97, 98].

Now, using the nearest-neighbor TB model [Fig. 5.11(c),(g)] [164], the AGNRs are gapless, say, they behave as semi-metals with a linear energy dispersion at the point, similar to monolayer graphene. On the other hand, the semiclassical model [Fig. 5.11(d),(h)] [160] can be adjusted to reproduce the LDA band gap values of 5AGNR and 11AGNR. In this model, the energy dispersions of the band levels vs wave vectors $\mathbf{k}$ have the form:

$$E_{\nu\mathbf{k}} = \pm\frac{\Delta E_G}{2}\sqrt{\nu^2 + \frac{2\hbar k^2}{m^*\Delta E_G}} \tag{5.1}$$

Here the upper/lower ($\pm$) signs refer to the conduction and valence levels (with the Fermi energy set to 0), k is parallel component of $\mathbf{k}$ to ΓX and m^* denotes the effective of charge carriers. ΔE_G turns out to depend on the ribbon width (w) and a velocity parameter V_F, being of the order of 10^6 m/s $\Delta E_G = \frac{2\pi V_F \hbar}{w}$. The effective mass may be estimated as $m^* = \frac{\Delta E_G}{2V_F^2}$.
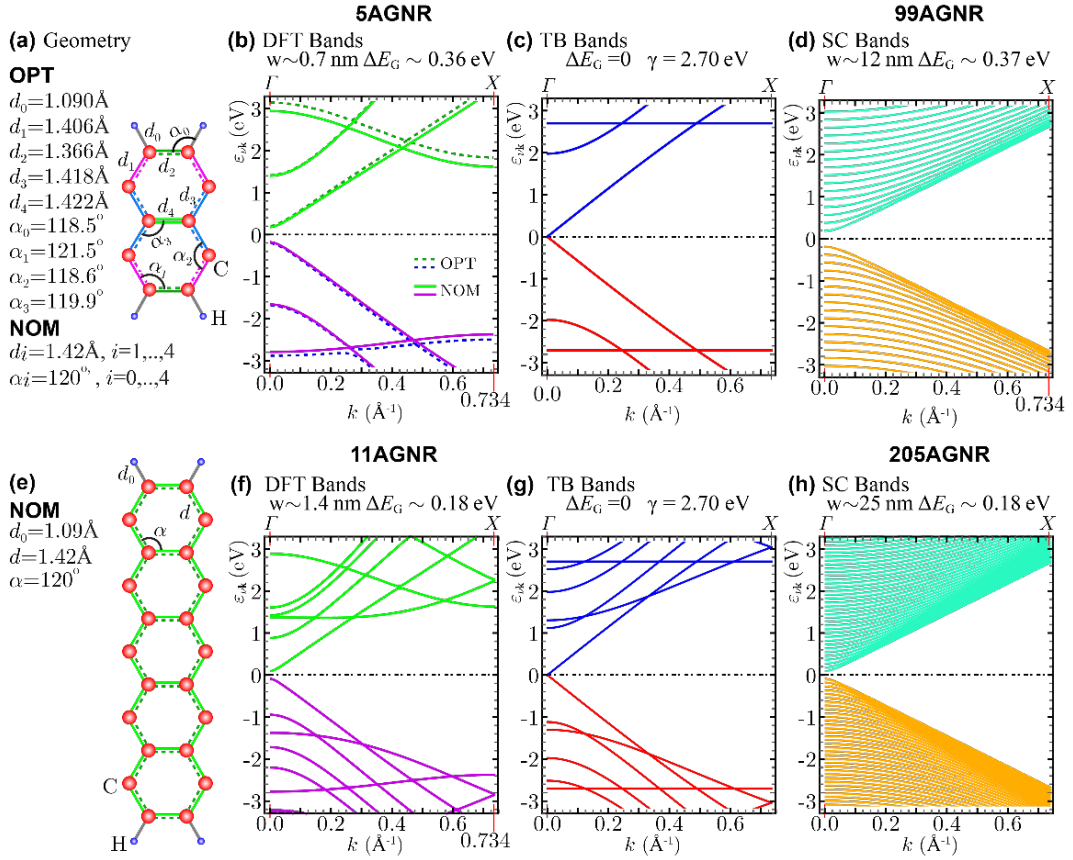
Figure 5.11: Structural and electronic properties of 5AGNR(a)-(c) and 11AGNR(e)-(g), i.e., unit-cells (a),(e) and energy bands obtained by PW-DFT in the LDA (b),(f) and nearest-neighbor TB model, with hopping parameter 2.7eV (c),(g). In (a) the LDA-optimized(OPT) unit-cell of 5AGNR is shown, whereas in (e) the ideal or nominal (NOM) unit-cell of 11AGNR is reported. Interestingly enough the geometrically optimized values of the bond-lengths and angles differ by 1% from the corresponding nominal values. Additionally, the band structure of 5AGNR within 2eV from the Fermi level is practically unaffected by relaxation effects (b). Electronic properties of 99AGNR(d) and 205AGNR(h), obtained from semi-classical(SC) approach, showing that the two wide AGNRs have the same band gap ΔE_G as the DFT+LDA band gap of 5AGNR and 11AGNR, respectively

However, the approach is valid only for wide nanoribbons, as testified by the fact that to obtain the same band gap values as the LDA band gaps (0.36 eV for 5AGNR and 0.18 eV for 11AGNR), we need to consider AGNRs of 12 nm and 25 nm in with, which would correspond to 99AGNR and 205AGNR, respectively. Furthermore, the energy dispersion of all bands computed are parabolic, which is far from a realistic DFT-based picture on narrow width GNRs [97, 98]. At this point TDDFT+RPA calculations are comparable with the semiclassical approach at low-energies < 100 terahertz where the intraband plasmon exists.

We present a comparison of the intraband dispersion of 5AGNR with the calculations based on the nearest-neighbor tight-binding model [164] [Fig. 5.12(a)] and the semi-classical approach [160][Fig. 5.12(b)(c)]. In the nearest-neighbor tight-binding model, a two-dimensional Coulomb potential was adopted, depending on an effective localization parameter of the p_z orbitals. The correlation matrix elements of Eq. were
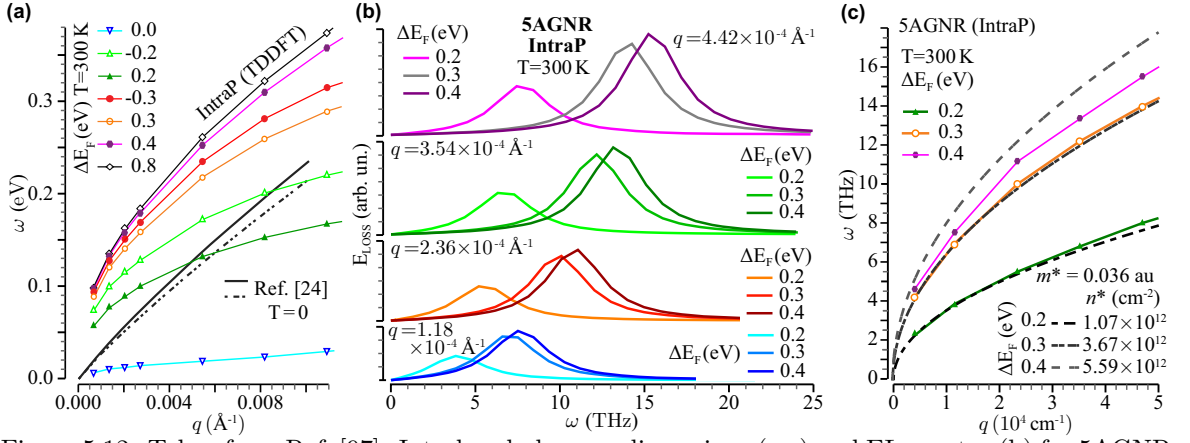
Figure 5.12: Taken from Ref. [97]. Intraband plasmon dispersions (a,c) and EL spectra (b) for 5AGNR at room temperature, low frequencies ($\omega < 100$ terahertz), and small momenta ($q < 10^5$ cm^{-1}). Our TDDFT calculations are shown in (a) and compared with the TB calculations of Ref. [164] (black continuous and dashed lines). The EL spectra in (b) are computed with a TDDFT approach that include only the VB and CB states. The intraband plasmon dispersions of (b) are shown in (c) and compared with the semiclassical model of Ref. [160] (dashed lines).

approximated by the low-$\mathbf{q}$ limit form, $\rho_{\nu\nu'}^{\mathbf{kq}}(0) = \langle\nu\mathbf{k}||\nu'\mathbf{k} + \mathbf{q}\rangle$, and a gapless band-structure was taken into account [Fig. 5.12(c),(g)]. The TB electronic features of 5AGNR allow only intraband modes that nevertheless, appear at the same scale as the TDDFT intraband plasmon of doped 5AGNR[Fig.5.12(a)].

For a careful scrutiny of the terahertz region, well converged results were obtained with a broadening life time parameter of *eta* of ~ 0.5 terahertz. The energy loss spectra for 5AGNR at T=300 K and $\omega \leq 20$ terahertz where computed by TDDFT+RPA with the highest valence band and the lowest conduction band on an MP mesh of 12500x1x1 $\mathbf{k}$-points shown. The corresponding intrabnand plasmon spectra are shown in Fig. 5.12(b). The plasmon dispersion curves are reported in Fig. 5.12(c) and compared to the semiclassical approach, where the plasmon responses in doped GNRs arrays of 10-100 nm width were described by the following analytical expression:

$$\omega = \text{Re}\left(\sqrt{\frac{2\pi n^* q cos^2\theta}{m^*} - \eta^2 - i\eta}\right) \tag{5.2}$$

Eq. 5.2 (here expressed in Hartree atomic units) depends on the concentration n^* of conduction electrons, and the effective mass m^*. The analytical and numerical curves turn out to be amazingly similar for $\Delta E_F < 0.5$ eV. Our findings demonstrate that these plasmon modes can be controlled and exploited for future nanodevice technology working on terahertz frequencies.

Chapter 6

Conclusions

In this thesis we have presented a full TDDFT+RPA approach sustainable for the analysis of the dielectric screening and plasmon resonances in graphene–related and beyond–graphene materials, which offer a wide range of potentials technological applications and represent an important field for fundamental research. Our main focus has been on graphene, silicene and germanene in free-standing monolayer conformations as well periodic 2D arrays of suspended semiconducting and semimetallic graphene nanoribbons with fixed edges on the far ends.

The intrinsic and extrinsic energy-loss function of free-standing monolayer graphene is presented in the Chapter 4. We have explored the energy-momentum range $\omega \leq 30$ eV and $q \leq 1.0$ Å^{-1}, respectively. In the eV scale from 1 eV to 30 eV, two plasmon peaks have been detected on undoped graphene in amazing agreement (energy and structure) with the experimental data [34, 19]. These are the π and $\sigma + \pi$ interband plasmons analogous to the well-known π and $\sigma + \pi$ plasmons of bilayer graphene and graphite [20, 34, 19]. Both interband plasmons in graphene are red-shifted respect to those in graphite. A narrow π plasmon is found at $\sim$ 4.5 eV and a broad $\sigma + \pi$ plasmon at $\sim$ 14.5 eV. The graphene π and $\sigma + \pi$ plasmons shown a relative similar intensity. Interesting enough at long-wavelengths ($q \to 0$), the π plasmon exhibits a $\sqrt{q}$ dispersion, and for $q > 0.2$ Å^{-1} the plasmon dispersion changes linearly. The energy-window considered up to ≤ 30 eV, was not plenty to describe the plasmon dispersion feature of the $\sigma + \pi$ plasmon, but it seems to quadratic at $q \to 0$, which changes to a $\sqrt{q}$-like dispersion with momentum (q) increase. The latter is consistent with a previous result [107].

At low energies < 1 eV, the energy-loss spectra on doped graphene were found to be very sensitive to doping i.e., electron or hole injections. Due to the anisotropic electron band structure (discussed in Chapter 4) observed in the ground-state of graphene, two type of carries moving with two distinct Fermi velocities were detected [44, 146], this particular effect is reflected in two distinct plasmon responses. First, a two-dimensional plasmon (2DP) is generated along the ΓK and ΓM directions by the two types of electrons oscillating in phase with one another. At long-wavelengths this 2DP displays a $\sqrt{q}$ dispersion as the conventional plasmon of a 2D electron-gas.

Second, an acoustic plasmon (AP) is originated only along the ΓK direction by the two types of electrons oscillating out-of-phase. The latter is not detected using the Dirac cone approximation because of an isotropic electron band structure is assumed in graphene. The AP shows a q dependent dispersion at small momentum. A gap opening in the single particle region is observed, inside it the 2DP is undamped and outside the 2DP begins to be damped. The results show that the 2DP and AP are tunable varying the positive or negative charge-carrier concentrations, and both plasmon modes also are expected to happen in the other honeycomb-like systems considered in this thesis.

The high energy loss spectrum ($1 \leq \omega \leq 20$ eV and momentum $q \leq 1$ Å^{-1}) of undoped silicene and undoped germanene have single out two interband plasmons structures along ΓK and ΓM paths. These interband collective excitations resembles to the π and $\sigma + \pi$ plasmons of graphene. The π plasmon is found at ~ 1.8 eV in silicene and germanene, while the $\sigma + \pi$ plasmon is found at ~ 4 eV in silicene and at ~ 3.2 eV in germanene. Unlike in graphene, silicene and germanene are characterized by a narrow π plasmon less intense than the broad $\sigma + \pi$ plasmon. Both interband plasmons show a $\sqrt{q}$ dispersion at long-wavelengths. Important enough, the optical spectra extracted from the imaginary part of the complex permittivity in silicene and germanene, have been found in agreement with previous absorbance calculations [149, 150] at $q \approx 10^{-2}$ Å^{-1}, which also has corroborated the validity and adaptability of our approach. A careful analysis in silicene has reveled that the π plasmon shows a hybridized behavior (π-like plasmon), which is assisted by single-particle processes between hybridized sp^3 and sp^2 states, connecting the π band to the π^* and σ^* like bands. This effect generates a double energy-momentum dispersion, which is more clearly resolved for momentum transfer along the ΓM path. These characteristics are consequence of the hybridization states, detectable in the ground state band structure. A similar high energy loss features were found in germanene.

Like in graphene, the low energy loss spectrum (< 1 eV) of silicene and germanene also were found to be very sensitive to doping. Likely, a non-single particle region (gap opening) is observed in each case. Silicene and germanene in free–standing conformations launch a 2DP plus an AP modes, which share many common features with the 2DP and AP modes of graphene, and whose relative strength can be modulated by positive or negative doping concentrations. Interesting enough, a new intraband plasmon (IntraP) is detected in germanene which is predicted to occur only with a positive doping $\Delta E_F > 0.3$ eV, along the ΓK and ΓM paths. This new IntraP is consequence of the partial occupation of the σ^* like band at the Γ point. More importantly, the 2DP and AP modes appear to be a signature of the honeycomb-like lattices, independently of the chemistry of the group-IV element, buckling parameter, or hybridization state [145].

We have discussed the dielectric properties and plasmon dispersions in planar GNR arrays [97, 98] scrutinizing the excitation energy regime going from the THz to the UV scale in the Chapter 5. At VIS to UV frequencies, we have found the two standard interband excitations of carbon-based materials, namely the π and $\sigma + \pi$ plasmons, with the π plasmon being strongly influenced by the GNR geometry. On the THz regime,

we have detected new collective modes of different nature. Semimetallic GNRs display an intraband 2D plasmon with large intensity relative to the high energy plasmons even in the intrinsic case. Semiconducting GNRs experience a fascinating interplay of intraband and interband collective modes, whose relative intensities and dispersions are strongly influenced by the actual occupation of single-particle levels near the Fermi energy. This strong sensitivity allows for a high tunability and control of the new plasmons. Indeed, nano-infrared imaging measurements in patterned GNRs on Al_2O_3 have revealed the appearance of an confined edge (interband) plasmon superimposed to a conventional (intraband) plasmon. The two modes are well resolved in space on GNR samples of 480 nm width at a working frequency of ~ 0.15 eV with a doping level of 0.3 eV [36]. In our narrow-width GNRs, the interband and intraband features can be resolved in momentum space, only. We also have corroborated that these modes are strongly sensitive to a bunch of geometrical/conformational parameters, such as the width, chirality and unit-cell extension of each GNR, as well as the in-plane vacuum distance between two contiguous GNRs.

All the results presented in this thesis demonstrate that it is possible to construct new materials with plasmonic resonances that are tunable to suit a specific demand in both the VIS-UV and THz regimes, by means of chemical doping, electronic gating, and also by means of a careful choice of the geometry. These findings if confirmed by further experiments would widen the perspectives on applications of graphene–related and beyond–graphene materials for the engineering of nanophotonic, nanoplasmonic and nanoelectronic devices.

Bibliography

[1] L. Novotny and B. Hecht, *Principles of nano-optics* (Cambridge university press, 2012).

[2] D. K. Gramotnev and S. I. Bozhevolnyi, Nature Photonics **4**, 83 (2010).

[3] J. B. Jackson and N. J. Halas, Proceedings of the National Academy of Sciences **101**, 17930 (2004).

[4] A. Tao, P. Sinsermsuksakul and P. Yang, Nature nanotechnology **2**, 435 (2007).

[5] M. Kahraman, P. Daggumati, O. Kurtulus, E. Seker and S. Wachsmann-Hogiu, Scientific reports **3** (2013).

[6] M. I. Stockman, Nature Photonics **2**, 327 (2008).

[7] L. Cao and M. L. Brongersma, Nature Photonics **3**, 12 (2009).

[8] A. B. Dahlin, N. J. Wittenberg, F. Höök and S.-H. Oh, Nanophotonics **2**, 83 (2013).

[9] N. G. Khlebtsov and L. A. Dykman, Journal of Quantitative Spectroscopy and Radiative Transfer **111**, 1 (2010).

[10] H. Im, H. Shao, Y. I. Park, V. M. Peterson, C. M. Castro, R. Weissleder and H. Lee, Nature biotechnology **32**, 490 (2014).

[11] T. B. Hoang, G. M. Akselrod, C. Argyropoulos, J. Huang, D. R. Smith and M. H. Mikkelsen, Nature communications **6** (2015).

[12] J. Song, P. Huang, H. Duan and X. Chen, Accounts of chemical research **48**, 2506 (2015).

[13] J. Li, S. K. Cushing, F. Meng, T. R. Senty, A. D. Bristow and N. Wu, Nature Photonics **9**, 601 (2015).

[14] A. Kriesch, S. P. Burgos, D. Ploss, H. Pfeifer, H. A. Atwater and U. Peschel, Nano letters **13**, 4539 (2013).

[15] H. A. Atwater, Scientific American **296**, 56 (2007).

[16] R. Zia, J. A. Schuller, A. Chandran and M. L. Brongersma, Materials today **9**, 20 (2006).

[17] M. I. Stockman, Phys. Today **64**, 39 (2011).

[18] M. I. Stockman, Optics express **19**, 22029 (2011).

[19] V. Despoja, D. Novko, K. Dekanić, M. Šunjić and L. Marušić, Physical Review B **87**, 075447 (2013).

[20] M. Pisarra, A. Sindona, M. Gravina, V. Silkin and J. Pitarke, Physical Review B **93**, 035440 (2016).

[21] B. Wu, N. Mathews and T.-C. Sum, Surface plasmon resonance, in *Plasmonic Organic Solar Cells*, pp. 25–31, Springer, 2017.

[22] K. Wang, L. Chen, H. Zhang and J. Chen, Applied Physics Letters **110**, 021105 (2017).

[23] Z. Liu, H. Lee, Y. Xiong, C. Sun and X. Zhang, science **315**, 1686 (2007).

[24] L. Hunt, Gold Bulletin **9**, 134 (1976).

[25] L. Rodríguez-Lorenzo, R. A. Alvarez-Puebla, I. Pastoriza-Santos, S. Mazzucco, O. Stéphan, M. Kociak, L. M. Liz-Marzán and F. J. García de Abajo, Journal of the American Chemical Society **131**, 4616 (2009).

[26] F. Schedin, A. Geim, S. Morozov, E. Hill, P. Blake, M. Katsnelson and K. Novoselov, Nature materials **6**, 652 (2007).

[27] J. Chen, J. Ge, L. Zhang, Z. Li, J. Li, Y. Sun and L. Qu, Microchimica Acta **183**, 1847 (2016).

[28] M. Gullans, D. Chang, F. Koppens, F. G. de Abajo and M. D. Lukin, Physical review letters **111**, 247401 (2013).

[29] G. Mie, Annalen der physik **330**, 377 (1908).

[30] A. C. Neto, F. Guinea, N. M. Peres, K. S. Novoselov and A. K. Geim, Reviews of modern physics **81**, 109 (2009).

[31] L. Ju *et al.*, Nature nanotechnology **6**, 630 (2011).

[32] J. Christensen, A. Manjavacas, S. Thongrattanasiri, F. H. Koppens and F. J. Garcia de Abajo, ACS nano **6**, 431 (2011).

[33] C. Sönnichsen, B. M. Reinhard, J. Liphardt and A. P. Alivisatos, Nature biotechnology **23**, 741 (2005).

[34] T. Eberlein, U. Bangert, R. Nair, R. Jones, M. Gass, A. Bleloch, K. Novoselov, A. Geim and P. Briddon, Physical Review B **77**, 233406 (2008).

[35] S. Liou, C.-S. Shie, C. Chen, R. Breitwieser, W. Pai, G. Guo and M.-W. Chu, Physical Review B **91**, 045418 (2015).

[36] Z. Fei *et al.*, Nano letters **15**, 8271 (2015).

[37] C. Vacacela Gomez, M. Pisarra, M. Gravina, J. M. Pitarke and A. Sindona, Phys. Rev. Lett. **117**, 116801 (2016).

[38] J. Zhao *et al.*, Progress in Materials Science **83**, 24 (2016).

[39] T. Stauber, Journal of Physics: Condensed Matter **26**, 123201 (2014).

[40] T. Stauber, J. Schliemann and N. Peres, Physical Review B **81**, 085409 (2010).

[41] S. Reich, J. Maultzsch, C. Thomsen and P. Ordejon, Physical Review B **66**, 035412 (2002).

[42] A. Grüneis, C. Attaccalite, L. Wirtz, H. Shiozawa, R. Saito, T. Pichler and A. Rubio, Physical Review B **78**, 205425 (2008).

[43] Y. Mao, J. Yuan and J. Zhong, Journal of Physics: Condensed Matter **20**, 115209 (2008).

[44] M. Pisarra, A. Sindona, P. Riccardi, V. Silkin and J. Pitarke, New Journal of Physics **16**, 083003 (2014).

[45] R. Mas-Balleste, C. Gomez-Navarro, J. Gomez-Herrero and F. Zamora, Nanoscale **3**, 20 (2011).

[46] A. Gupta, T. Sakthivel and S. Seal, Progress in Materials Science **73**, 44 (2015).

[47] K. I. Bolotin, K. Sikes, Z. Jiang, M. Klima, G. Fudenberg, J. Hone, P. Kim and H. Stormer, Solid State Communications **146**, 351 (2008).

[48] X. Wang, L. Zhi and K. Müllen, Nano letters **8**, 323 (2008).

[49] Y. Wu *et al.*, Nano letters **12**, 3062 (2012).

[50] S. Z. Butler *et al.*, ACS nano **7**, 2898 (2013).

[51] N. J. Roome and J. D. Carey, ACS applied materials & interfaces **6**, 7743 (2014).

[52] A. Dimoulas, Microelectronic Engineering **131**, 68 (2015).

[53] K. S. Novoselov, A. K. Geim, S. V. Morozov, D. Jiang, Y. Zhang, S. V. Dubonos, I. V. Grigorieva and A. A. Firsov, science **306**, 666 (2004).

[54] K. S. Novoselov, A. K. Geim, S. Morozov, D. Jiang, M. Katsnelson, I. Grigorieva, S. Dubonos and A. Firsov, nature **438**, 197 (2005).

[55] A. K. Geim and K. S. Novoselov, Nature materials **6**, 183 (2007).

[56] K. R. Paton *et al.*, Nature materials **13**, 624 (2014).

[57] P. Miró, M. Audiffred and T. Heine, Chemical Society Reviews **43**, 6537 (2014).

[58] K. S. Novoselov *et al.*, Nature **490**, 192 (2012).

[59] J. O. Sofo, A. S. Chaudhari and G. D. Barber, Physical Review B **75**, 153401 (2007).

[60] X. Du, I. Skachko, A. Barker and E. Y. Andrei, arXiv preprint arXiv:0802.2933 (2008).

[61] M. Orlita *et al.*, Physical review letters **101**, 267601 (2008).

[62] P. R. Wallace, Physical Review **71**, 622 (1947).

[63] D. Pesin and A. H. MacDonald, Nature materials **11**, 409 (2012).

[64] Q. Xiang, J. Yu and M. Jaroniec, Chemical Society Reviews **41**, 782 (2012).

[65] A. J. Huber, F. Keilmann, J. Wittborn, J. Aizpurua and R. Hillenbrand, Nano letters **8**, 3766 (2008).

[66] P. Szumniak, S. Bednarek, B. Partoens and F. Peeters, Physical review letters **109**, 107201 (2012).

[67] K. Takeda and K. Shiraishi, Physical Review B **50**, 14916 (1994).

[68] Y. Cai, C.-P. Chuu, C. Wei and M. Chou, Physical Review B **88**, 245408 (2013).

[69] S. Balendhran, S. Walia, H. Nili, S. Sriram and M. Bhaskaran, small **11**, 640 (2015).

[70] B. Mortazavi, O. Rahaman, M. Makaremi, A. Dianat, G. Cuniberti and T. Rabczuk, Physica E: Low-dimensional Systems and Nanostructures **87**, 228 (2017).

[71] S. Cahangirov, M. Topsakal, E. Aktürk, H. Şahin and S. Ciraci, Physical review letters **102**, 236804 (2009).

[72] L. Li and M. Zhao, The Journal of Physical Chemistry C **118**, 19129 (2014).

[73] L. Lew Yan Voon, E. Sandberg, R. Aga and A. Farajian, Applied Physics Letters **97**, 163114 (2010).

[74] L. Matthes, O. Pulci and F. Bechstedt, Journal of Physics: Condensed Matter **25**, 395305 (2013).

[75] A. O?hare, F. Kusmartsev and K. Kugel, Nano letters **12**, 1045 (2012).

[76] S. Wang, Physical Chemistry Chemical Physics **13**, 11929 (2011).

[77] S. Trivedi, A. Srivastava and R. Kurchania, Journal of Computational and Theoretical Nanoscience **11**, 781 (2014).

[78] C. J. Tabert and E. J. Nicol, Physical Review B **87**, 235426 (2013).

[79] L. Stille, C. J. Tabert and E. J. Nicol, Physical Review B **86**, 195405 (2012).

[80] Z. Ni, Q. Liu, K. Tang, J. Zheng, J. Zhou, R. Qin, Z. Gao, D. Yu and J. Lu, Nano letters **12**, 113 (2011).

[81] R. Quhe *et al.*, Scientific reports **2**, 853 (2012).

[82] M. Y. Han, B. Özyilmaz, Y. Zhang and P. Kim, Physical review letters **98**, 206805 (2007).

[83] X. Wang, Y. Ouyang, X. Li, H. Wang, J. Guo and H. Dai, Physical review letters **100**, 206803 (2008).

[84] Y.-W. Son, M. L. Cohen and S. G. Louie, Physical review letters **97**, 216803 (2006).

[85] R. M. Jacobberger *et al.*, Nature communications **6** (2015).

[86] F. Schwierz, Nature nanotechnology **5**, 487 (2010).

[87] T. Mueller, F. Xia and P. Avouris, Nature Photonics **4**, 297 (2010).

[88] F. Bonaccorso, Z. Sun, T. Hasan and A. Ferrari, Nature photonics **4**, 611 (2010).

[89] P. Avouris, Nano letters **10**, 4285 (2010).

[90] S. Rao, A. Stesmans, K. Keunen, D. Kosynkin, A. Higginbotham and J. Tour, Applied Physics Letters **98**, 083116 (2011).

[91] M. Ezawa, Physical Review B **73**, 045432 (2006).

[92] J. Lan, J.-S. Wang, C. K. Gan and S. K. Chin, Physical Review B **79**, 115401 (2009).

[93] D. A. Abanin, P. A. Lee and L. S. Levitov, Physical review letters **96**, 176803 (2006).

[94] L. Yang, C.-H. Park, Y.-W. Son, M. L. Cohen and S. G. Louie, Physical Review Letters **99**, 186801 (2007).

[95] E.-j. Kan, Z. Li, J. Yang and J. Hou, Journal of the American Chemical Society **130**, 4224 (2008).

[96] K. Nakada, M. Fujita, G. Dresselhaus and M. S. Dresselhaus, Physical Review B **54**, 17954 (1996).

[97] C. V. Gomez, M. Pisarra, M. Gravina, J. M. Pitarke and A. Sindona, Physical Review Letters **117**, 116801 (2016).

[98] C. V. Gomez, M. Pisarra, M. Gravina and A. Sindona, Beilstein Journal of Nanotechnology **8**, 172 (2017).

[99] S. H. Vosko, L. Wilk and M. Nusair, Canadian Journal of physics **58**, 1200 (1980).

[100] X. Blase, A. Rubio, S. G. Louie and M. L. Cohen, Physical review B **51**, 6868 (1995).

[101] E. S. Kryachko and E. V. Ludeña, Phys Rep **544**, 123 (2014).

[102] M. Malagoli and J. Brédas, Chemical Physics Letters **327**, 13 (2000).

[103] E. K. Gross and R. M. Dreizler *Density functional theory* Vol. 337 (Springer Science & Business Media, 2013).

[104] R. Kuzuo, M. Terauchi and M. Tanaka, Japanese journal of applied physics **31**, L1484 (1992).

[105] W. Brandt and G. Lapicki, Physical Review A **23**, 1717 (1981).

[106] V. Despoja, D. J. Mowbray, D. Vlahović and L. Marušić, Physical Review B **86**, 195429 (2012).

[107] D. Novko, V. Despoja and M. Šunjić, Physical Review B **91**, 195407 (2015).

[108] J. C. Slater *Quantum theory of molecules and solids* Vol. 1 (McGraw-Hill New York, 1963).

[109] L. H. Thomas, The calculation of atomic fields, in *Mathematical Proceedings of the Cambridge Philosophical Society* Vol. 23, pp. 542–548, Cambridge Univ Press, 1927.

[110] E. Fermi, Rend. Accad. Naz. Lincei **6**, 602 (1927).

[111] P. A. Dirac, Note on exchange phenomena in the thomas atom, in *Mathematical Proceedings of the Cambridge Philosophical Society* Vol. 26, pp. 376–385, Cambridge Univ Press, 1930.

[112] P. Hohenberg and W. Kohn, Physical review **136**, B864 (1964).

[113] W. Kohn and L. J. Sham, Physical review **140**, A1133 (1965).

[114] V. Fano and L. Fano, (1980).

[115] R. M. Martin, *Electronic structure: basic theory and practical methods* (Cambridge university press, 2004).

[116] M. C. Payne, M. P. Teter, D. C. Allan, T. Arias and J. Joannopoulos, Reviews of Modern Physics **64**, 1045 (1992).

[117] L. Hedin and B. I. Lundqvist, Journal of Physics C: Solid State Physics **4**, 2064 (1971).

[118] D. M. Ceperley and B. Alder, Physical Review Letters **45**, 566 (1980).

[119] J. P. Perdew and K. Burke, International journal of quantum chemistry **57**, 309 (1996).

[120] O. Gunnarsson, M. Jonson and B. Lundqvist, Physical Review B **20**, 3136 (1979).

[121] V. I. Anisimov, F. Aryasetiawan and A. Lichtenstein, Journal of Physics: Condensed Matter **9**, 767 (1997).

[122] A. D. Becke, The Journal of chemical physics **98**, 1372 (1993).

[123] J. Ziman, Solid State Physics **26**, 1 (1971).

[124] H. J. Monkhorst and J. D. Pack, Physical review B **13**, 5188 (1976).

[125] G. Bachelet, D. Hamann and M. Schlüter, Physical Review B **26**, 4199 (1982).

[126] D. Vanderbilt, Physical Review B **41**, 7892 (1990).

[127] J. C. Slater, Physical Review **36**, 57 (1930).

[128] B. H. Bransden and C. J. Joachain, *Quantum mechanics* (Pearson Education, 2000).

[129] S. Boys, The integral formulae for the variational solution of the molecular many-electron wave equations in terms of gaussian functions with direct electronic correlation, in *Proceedings of the Royal Society of London A: Mathematical, Physical and Engineering Sciences* Vol. 258, pp. 402–411, The Royal Society, 1960.

[130] J. M. Soler, E. Artacho, J. D. Gale, A. García, J. Junquera, P. Ordejón and D. Sánchez-Portal, Journal of Physics: Condensed Matter **14**, 2745 (2002).

[131] C. Kramberger *et al.*, Physical review letters **100**, 196803 (2008).

[132] J. Yan, K. S. Thygesen and K. W. Jacobsen, Physical review letters **106**, 146803 (2011).

[133] S. L. Adler, Physical Review **126**, 413 (1962).

[134] N. Wiser, Physical Review **129**, 62 (1963).

[135] G. Onida, L. Reining and A. Rubio, Reviews of Modern Physics **74**, 601 (2002).

[136] A. Nemilentsau, T. Low and G. Hanson, Physical review letters **116**, 066804 (2016).

[137] I. Soto Lamata, P. Alonso-Gonzalez, R. Hillenbrand and A. Y. Nikitin, ACS Photonics **2**, 280 (2015).

[138] A. Grigorenko, M. Polini and K. Novoselov, Nature photonics **6**, 749 (2012).

[139] F. H. Koppens, D. E. Chang and F. J. García de Abajo, Nano letters **11**, 3370 (2011).

[140] X. Gonze *et al.*, Computational Materials Science **25**, 478 (2002).

[141] X. Gonze *et al.*, Computer Physics Communications **180**, 2582 (2009).

[142] J. P. Perdew and A. Zunger, Physical Review B **23**, 5048 (1981).

[143] N. Troullier and J. L. Martins, Physical review B **43**, 1993 (1991).

[144] G. Borghi, M. Polini, R. Asgari and A. MacDonald, Solid State Communications **149**, 1117 (2009).

[145] C. V. Gomez, M. Pisarra, M. Gravina, P. Riccardi and A. Sindona, arXiv preprint arXiv:1610.03652 (2016).

[146] A. Sindona, M. Pisarra, D. Mencarelli, L. Pierantoni and S. Bellucci, Plasmon modes in extrinsic graphene: Ab initio simulations vs semi-classical models, in *Fundamental and Applied Nano-Electromagnetics*, pp. 125–144, Springer, 2016.

[147] B. Mohan, A. Kumar and P. Ahluwalia, Physica E: Low-dimensional Systems and Nanostructures **53**, 233 (2013).

[148] R. Das, S. Chowdhury, A. Majumdar and D. Jana, RSC Advances **5**, 41 (2015).

[149] L. Matthes, P. Gori, O. Pulci and F. Bechstedt, Physical Review B **87**, 035438 (2013).

[150] L. Matthes, O. Pulci and F. Bechstedt, New Journal of Physics **16**, 105007 (2014).

[151] M. Lin, C. Huang and D. Chuu, Physical Review B **55**, 13961 (1997).

[152] C. V. Gomez, M. Pisarra, M. Gravina, S. Bellucci and A. Sindona, Ab initio modelling of dielectric screening and plasmon resonances in extrinsic silicene, in *Research and Technologies for Society and Industry Leveraging a better tomorrow (RTSI), 2016 IEEE 2nd International Forum on*, pp. 1–4, IEEE, 2016.

[153] S. Allen Jr, D. Tsui and R. Logan, Physical Review Letters **38**, 980 (1977).

[154] A. Principi, R. Asgari and M. Polini, Solid State Communications **151**, 1627 (2011).

[155] A. Politano, A. Marino, V. Formoso, D. Farías, R. Miranda and G. Chiarello, Physical Review B **84**, 033401 (2011).

[156] P. Vogt, P. De Padova, C. Quaresima, J. Avila, E. Frantzeskakis, M. C. Asensio, A. Resta, B. Ealet and G. Le Lay, Physical review letters **108**, 155501 (2012).

[157] F. J. Garcia de Abajo, Acs Photonics **1**, 135 (2014).

[158] W. Wang and J. M. Kinaret, Physical Review B **87**, 195424 (2013).

[159] L. Brey and H. Fertig, Physical Review B **73**, 235411 (2006).

[160] V. Popov, T. Y. Bagaeva, T. Otsuji and V. Ryzhii, Physical Review B **81**, 073404 (2010).

[161] C. Tao *et al.*, Nature Physics **7**, 616 (2011).

[162] P. Tassin, T. Koschny, M. Kafesaki and C. M. Soukoulis, Nature Photonics **6**, 259 (2012).

[163] B. Kiraly, A. J. Mannix, R. M. Jacobberger, B. L. Fisher, M. S. Arnold, M. C. Hersam and N. P. Guisinger, Applied Physics Letters **108**, 213101 (2016).

[164] D. R. Andersen and H. Raza, Physical Review B **85**, 075425 (2012).